Cellular-Enabled Machine Type Communications: Recent Technologies and Cognitive Radio Approaches

Abdelmohsen Ali

A Thesis

in

The Department

of

Electrical and Computer Engineering

Presented in Partial Fulfillment of the Requirements

for the Degree of Doctor of Philosophy at

Concordia University

Montréal, Québec, Canada

Sept, 2016

CONCORDIA UNIVERSITY

SCHOOL OF GRADUATE STUDIES

This is to certify that the thesis prepared

By: Abdelmohsen Ali

Entitled: Cellular-Enabled Machine Type Communications: Recent Technologies and Cognitive Radio Approaches

and submitted in partial fulfillment of the requirements for the degree of

Doctor of Philosophy (Electrical & Computer Engineering)

complies with the regulations of the University and meets the accepted standards with respect to originality and quality.

Signed by the final examining committee:

Chair

Dr. J.Y. Yu

External Examiner

Dr. F. Labeau

External to Program

Dr. C. Assi

Examiner

Dr. M.O. Ahmad

Examiner

Dr. Y.R. Shayan

Thesis Supervisor

Dr. W. Hamouda

Approved by: Dr. W.-P. Zhu, Graduate Program Director

September 30, 2016

Dr. A. Asif, Dean, Faculty of Engineering & Computer Science

Abstract

Cellular-Enabled Machine Type Communications: Recent Technologies and Cognitive Radio Approaches

Abdelmohsen Ali, PhD.

Concordia University, 2016

The scarcity of bandwidth has always been the main obstacle for providing reliable high data-rate wireless links, which are in great demand to accommodate nowadays and immediate future wireless applications. In addition, recent reports have showed inefficient usage and under-utilization of the available bandwidth. Cognitive radio (CR) has recently emerged as a promising solution to enhance the spectrum utilization, where it offers the ability for unlicensed users to access the licensed spectrum opportunistically. By allowing opportunistic spectrum access which is the main concept for the interweave network model, the overall spectrum utilization can be improved. This requires cognitive radio networks (CRNs) to consider the spectrum sensing and monitoring as an essential enabling process for the interweave network model.

Machine-to-machine (M2M) communication, which is the basic enabler for the Internet-of-Things (IoT), has emerged to be a key element in future networks. Machines are expected to communicate with each other exchanging information and data without human intervention. The ultimate objective of M2M communications is to construct comprehensive connections among all machines distributed over an extensive coverage area. Due to the radical change in the number of users, the network has to carefully utilize the available resources in order to maintain reasonable quality-of-service (QoS). Generally, one of the most important resources in wireless communications is the frequency spectrum. To utilize the frequency spectrum in IoT environment, it can be argued that cognitive radio concept is a possible solution from the cost and performance perspectives. Thus, supporting numerous number of machines is possible by employing dual-mode base stations which can apply cognitive radio concept in addition to the legacy licensed frequency assignment.

In this thesis, a detailed review of the state of the art related to the application of spectrum sensing in CR communications is considered. We present the latest advances related to the implementation of the legacy spectrum sensing approaches. We also address the implementation challenges for cognitive radios in the direction of spectrum sensing and monitoring. We propose a novel algorithm to solve the reduced throughput issue due to the scheduled spectrum sensing and monitoring. Further, two new architectures are considered to significantly reduce the power consumption required by the CR to enable wideband sensing. Both systems rely on the 1-bit quantization at the receiver side. The system performance is analytically investigated and simulated. Also, complexity and power consumption are investigated and studied.

Furthermore, we address the challenges that are expected from the next generation M2M network as an integral part of the future IoT. This mainly includes the design of low-power low-cost machine with reduced bandwidth. The trade-off between cost, feasibility, and performance are also discussed. Because of the relaxation of the frequency and spatial diversities, in addition, to enabling the extended coverage mode, initial synchronization and cell search have new challenges for cellular-enabled M2M systems. We study conventional solutions with their pros and cons including timing acquisition, cell detection, and frequency offset estimation algorithms. We provide a technique to enhance the performance in the presence of the harsh detection environment for LTE-based machines. Furthermore, we present a frequency tracking algorithm for cellular M2M systems that utilizes the new repetitive feature of the broadcast channel symbols in next generation Long Term Evolution (LTE) systems. In the direction of narrowband IoT support, we propose a cell search and initial synchronization algorithm that utilizes the new set of narrowband synchronization signals. The proposed algorithms have been simulated at very low signal to noise ratios and in different fading environments.

To my dearest wife, Sara Salah, for her support and encouragement

and

my parents, and my adorable kids Yousef and Farah, for their patience.

Acknowledgments

First and foremost, all praise and thanks are due to Allah (God) for giving me the power to believe in my passion and pursue my dreams. I could never have finished this thesis without the faith I have in Him and depending on Him.

I would like to express my gratitude and thanks to my supervisor Prof. Walaa Hamouda for his role as a great advisor and all the support he provided me both technically and socially. His support and insightful advices were crucial to my academic success and my development as a researcher. Both on the personal and technical levels, I could easily say that Prof. Hamouda has a great impact on me and I hope that I will adhere to all the technical and ethical values I have learned from as a supervisor and a teacher.

I am also thankful to Prof. Yousef Shayan, Prof. M. Omair Ahmad, and Prof. Chadi Assi for serving on my thesis committee and for providing constructive comments that made this thesis better.

I am sincerely thankful to Concordia Graduate Student Support Program (GSSP) for funding my PhD's studies.

Finally, I would like to express my greatest and deepest appreciation to my family. Special thanks to Sara Salah, my wife and best friend, for all the tremendous love and all the support at all the times she gives to me. Thank you Sara for being a steadfast source of encouragement and inspiration to me. It is no exaggeration to say that without your sacrifice and infinite patience, this thesis would never have existed. Thanks to our kids, Yousef and Farah, for being so cute and filling our life with joy and hope. Last but not least, thanks to my mother and father whose endless love and sincere prayers have always been with me.

Contents

List of Figures

List of Tables

List of Common Symbols

$\mathbf{x}$	vector $\mathbf{x}$
$a_{i,j}$	element in matrix A with row i and column j
σ_X^2	variance of Gaussian distributed random variable X
$(\mathbf{x})^T$	transpose of vector $\mathbf{x}$
$(\mathbf{x})^H$	conjugate Transpose of vector $\mathbf{x}$
$(\mathbf{X})^{-1}$	matrix inverse of matrix $\mathbf{X}$
$*$	convolution operator
$\|\mathbf{x}\|_p$	p norm for vector $\mathbf{x}$, also called ℓ_p norm
min	minimization
max	maximization
$\mathrm{E}(X)$	expectation of random variable X
m_X	mean of random variable X
$\mathrm{Var}(X)$	variance of random variable X
$\ln(a)$	natural logarithm of a
$\log_{10}(a)$	base-10 logarithm of a
I_M	$M \times M$ identity matrix
$\mathcal{H}_0$	null hypothesis
$\mathcal{H}_1$	alternative hypothesis
$\mathbb{C}$	set of complex numbers
$\mathbb{R}$	set of real numbers
$\cup$	union operator
Pr(a)	Probability of event a
$\Gamma(\,,\,)$	Upper Gamma function
$I(\,,\,)$	Upper incomplete beta function

$Q(\,)$	Q-function
$\delta(x)$	Delta function
$F(x)$	Cumulative distribution function
$f(x)$	Probability density function
$\mathcal{N}$	Gaussian distribution
$\chi^2_N(\,)$	Chi-squared distribution of degree N
$\in$	within the group
$\forall$	for all
$A \subseteq B$	A is a subset of B
$\angle Z$	angle of the complex number Z

List of Acronyms

ADC	Analogue to Digital Converter
3GPP	3rd Generation Partnership Project
AGC	Automatic-Gain-Control
ARIB	Association of Radio Industries and Businesses
AWGN	Additive White Gaussian Noise
BP	Basis Pursuit
BPF	Band-Pass Filter
CAF	Cyclic Autocorrelation Function
CFO	Carrier Frequency Offset
CP	Cyclic Prefix
CR	Cognitive Radio
CRN	Cognitive Radio Network
CSCG	Circularly Symmetric Complex Gaussian
DAC	Digital to Analouge Converter
DCI	Downlink Control Information
DFH	Dynamic Frequency Hopping
DRX	Discontinuous Reception
DSMF	Dynamic Spectrum Management Framework

ED	Energy Detector
ER	Energy Ratio
ETSI	European Telecommunications Standards Institute
FC	Fusion Center
FFT	Fast Fourier Transform
H2H	Human to Human
i.i.d.	Independent and identically distributed
ICI	Inter Carrier Interference
IoT	Internet of Things
ISI	Inter Symbol Interference
LDPC	Low Density Parity Check
LNA	Low Noise Amplifier
LO	Local Oscillator
LS	Least Squares
LTE	Long Term Evolution
M2M	Machine to Machine
MF	Matched Filter
MIB	Master Information Block
MIMO	Multiple Input Multiple Output
ML	Maximum Likelihood
MTC	Machine Type Communication

NB	Narrow band
NBI	Narrow Band Interference
NLOS	Non-Line Of Sight
OFDM	Orthogonal Frequency Division Multiplexing
OMP	Orthogonal Matching Pursuit
PAPR	Peak to Average Power Ratio
PBCH	Physical Broadcast Channel
PDCCH	Physical Downlink Control Channel
PDP	Power Delay Profile
PDSCH	Physical Downlink Shared Channel
PLL	Phase-Locked-Loop
PN	Phase Noise
PNR	Primary to Secondary Noise Ratio
PRACH	Physical Random Access Channel
PRB	Physical Resource Block
PSD	Power Spectral Density
PSS	Primary Synchronization Signal
PU	Primary User
PUCCH	Physical Uplink Control Channel
PUSCH	Physical Uplink Shared Channel
QoS	Quality of Service

QP	Quiet Period
RAN	Radio Access Networks
RE	Resource Element
RF	Radio Frequency
RIP	Restricted Isometry Property
ROC	Receiver Operating Characteristics
RS	Reference Symbol
RSSI	Received Signal Strength Indicator
SAR	Successive Approximation
SC-FDMA	Single Carrier Frequency Division Multiple Access
SFBC	Space-Frequency Block Code
SFO	Sampling Frequency Offset
SIMO	Single Input Multiple Output
SISO	Single Input Single Output
SNR	Signal to Noise Ratio
SPR	Secondary-to-Primary power Ratio
SPR	Secondary to Primary Power Ratio
SSS	Secondary Synchronization Signal
STBC	Space-Time Block Code
SU	Secondary User
TI	Time-Interleaved

TTI	Transmission Time Interval
UE	User Equipment
UHF	Ultra-High Frequency
UWB	Ultra-Wideband
WB	Wide band
WLS	Weighted Least-Squares

Chapter 1

Introduction

1.1 Machine Type Communications and Internet Of Things

The Internet technology has undergone enormous changes since its early stages and it has become an important communication infrastructure targeting anywhere, anytime connectivity. Historically, human-to-human (H2H) communication, mainly voice communication, has been the center of importance. Therefore, the current network protocols and infrastructure are optimized for human-oriented traffic characteristics. Lately, an entirely different paradigm of communication has emerged with the inclusion of "machines" in the communications landscape. In that sense, machines/devices that are typically wireless such as sensors, actuators, and smart meters are able to communicate with each other exchanging information and data without human intervention. Since the number of connected devices/machines is expected to surpass the human-centric communication devices by tenfold, machine-to-machine (M2M) communication is expected to be a key element in future networks [1]. With the introduction of M2M communications, the next generation Internet or the Internet-of-Things (IoT) has to offer the facilities to connect different objects together whether they belong to humans or not.

Due to the radical change in the number of users, the network has to carefully utilize the available resources in order to maintain reasonable quality-of-service (QoS). Generally, one of the most important resources in wireless communications is the frequency spectrum. To support larger number of connected devices in the future IoT, it is likely to add more degrees of freedom represented in more operating frequency bands. However, the frequency spectrum

is currently scarce and requiring additional frequency resources makes the problem of supporting this massive number of devices even harder to solve. In fact, this issue is extremely important especially for the cellular architecture since the spectrum scarcity problem directly influences the reliability and the QoS offered by the network.

With the large coverage and flexible data rates offered by cellular systems, research efforts from industry have recently been focused on optimizing the existing cellular networks considering M2M specifications. Among other solutions, scenarios defined by the 3rd Generation Partnership Project (3GPP) standardization body emerge as the most promising solutions to enable wireless infrastructure of M2M communications [2]. In this front, two special categories, namely CAT-M for machine-type-communication (MTC) and Narrowband-IoT (NB-IoT), have been incorporated by the 3GPP to Long-Term-Evolution (LTE) specifications to support M2M and IoT features. Due to the M2M communication challenges and the wide range of supported device specifications, developing the features for M2M communication started as early as release 10 (R10) for the advanced LTE standard. This continued to future releases including release 13 (R13) that is currently developed and expected to be released late in 2016. By introducing the new systems, many implementation challenges arise and have to be addressed by innovative solutions.

1.2 Cognitive Radio

The rapid demand for providing high throughputs in wireless communications that support new applications such as video-streaming, cellular phones and high-speed Internet etc. makes wireless communications a challenging field. For instance, cellular systems have experienced a tremendous growth over the last decade, and this translates to requiring more frequency spectrum to accommodate this unprecedented increase in the number of subscribed users. However, spectrum is very scarce, and, if available, it is very expensive. At the same time, the allocated spectrum has been shown to be severely under-utilized. This scarcity and under-utilization of the spectrum usage necessitate exploiting the available spectrum opportunistically.

Cognitive radio (CR), as an emerging solution, offers the cognitive (secondary) users (SUs)

the ability to access the licensed spectrum in an opportunistic manner. More specifically, the CR techniques allow SUs to sense the unused spectrum and share it without significant interference with other users (Spectrum sensing)[3], to manage the best available spectrum to fulfill the user communication demands (Spectrum management)[4], to maintain certain required quality of service (QoS) during switching to better spectrum (Spectrum mobility)[5], and to provide a fair spectrum sharing among all coexisting users (Spectrum sharing)[6].

In addition to the small cell design, the application of the heterogeneous network concept was investigated where cellular MTC networks can utilize other networks such as WiFi to reduce the number of directly connected machines/users. On the other hand, *cognitive radio (CR) support* is a promising solution for supporting massive MTC devices. It can be argued that cognitive radio concept is a possible solution from the cost and performance perspectives [7]. However, there are more practical challenges that need efforts from researchers in order to have a reliable and a mature solution. Future standards are encouraged to provide both options (i.e. the cognition concept and the heterogeneous network model).

1.3 Motivation

The key objectives of this thesis are to:

1. study the challenges for the next generation MTC cellular networks and provide an efficient solution based on cognitive radio concept for the massive interconnected devices in a scarce spectrum;

2. provide practical solutions in terms of spectrum sensing and monitoring to enable the design of the interweave cognitive radio networks;

3. partially address the practical implementation challenges for the next generation cellular MTC networks;

4. develop analytical and simulation frameworks for the developed techniques.

The proposed work is important in various ways. It certainly addresses a timely topic (cognitive radio systems in conjunction with cellular MTC and IoT), which is expected to play

a major role in many of the future wireless communication systems. In fact, this technology is expected to revolutionize how wireless communication networks will be implemented or deployed in the future, with a focus on addressing the problems of spectrum under-utilization and supporting numerous number of interconnected MTC devices.

The interweave cognitive radio network model has been chosen by many standards to implement the cognition concept. Applying spectrum sensing and monitoring in both narrowband and wideband spectrum have been addressed by many researchers. However, increasing the cognitive radio throughput given the constraint of reducing the harmful interference to the primary user is a real challenge. Furthermore, the trade-off between complexity, power consumption, and sensing performance is a critical aspect. An up to date architectures are required to address these issues. In light of this, we believe that simpler and more practically implementable spectrum sensing and monitoring techniques are still lacking in the literature.

MTC devices are expected to be deployed in harsh environments which typically can be characterized by low coverage, ultra low power consumption, and reduced complexity. Due to these reasons, a significant number of implementation challenges come to the picture while defining the specifications for enhanced coverage user equipments in cellular enabled networks. For instance, cell search and initial synchronization are significant challenges at these low receiver capabilities with ultra low received power. Unconventional and system-specific solutions are required to tackle these issues and to enable a reduced-complexity enhanced-coverage devices. Due to the recent introduction to the MTC and IoT systems, the current literature lacks this innovative techniques.

1.4 Thesis Contributions

The contributions of this thesis can be summarized as follows.

- Among various network models, we focus on the enabling technique for the interweave cognitive radio networks which have received great attention from standards perspective due to its reliability to achieve the required QoS. Several researchers have already considered various aspects to realize efficient techniques for spectrum sensing. In this direction, we have provided a detailed review of the state of the art related to the

application of spectrum sensing in CR communications [8]. We present the latest advances related to the implementation of the legacy spectrum sensing approaches [9].

- We address the challenges that are expected from the next generation MTC network as an integral part of the future IoT. This mainly includes the design of low-power low-cost machine with reduced bandwidth. The trade-off between cost, feasibility, and performance are also discussed. Supporting numerous number of MTC devices is possible by employing dual-mode base stations which can apply cognitive radio concept in addition to the legacy licensed frequency assignment [7].

- We address the implementation challenges for cognitive radios in the direction of spectrum sensing and monitoring. We propose a novel algorithm to solve the reduced throughput issue due to the scheduled spectrum sensing and monitoring [10][11][12]. Furthermore, we provide two new solutions for the high power consumption required by the CR to enable wideband sensing. Both techniques employ one-bit quantizer to significantly reduce the power budget [13][14][15]. However, the architectures for the two solutions are different.

- Because of the relaxation of the frequency and spatial diversities, in addition, to enabling the extended coverage mode, initial synchronization and cell search have new challenges for LTE-MTC systems. We study conventional solutions with their pros and cons including timing acquisition, cell detection, and frequency offset estimation algorithms for non LTE-MTC systems. We propose a technique to enhance the performance by folding the time [16]. Furthermore, we propose a frequency tracking algorithm for LTE-MTC systems that utilize the new repetitive feature of the broadcast channel symbols [17]. In the direction of NB-IoT, we propose a cell search and initial synchronization algorithm that utilizes the new set of narrowband synchronization signals [18]. The proposed algorithms have been simulated at very low Signal to Noise Ratios (SNR) and in different fading environments.

1.5 Thesis Organization

The rest of the thesis is organized as follows:

In Chapter 2, we present some relevant background on the fundamentals of opportunistic CR systems. We begin by introducing the CR concept, where we focus on interweave model and mainly spectrum sensing and monitoring. We also present briefly the various types of narrowband and wideband spectrum sensing schemes. Then, we introduce the basic concepts of physical LTE systems and its relevant transmission technique, namely the Orthogonal Frequency Division Multiplexing (OFDM). The essential information about the MTC and NB-IoT categories are also covered. In the last part of this chapter, we provide the related works to this research in the literature.

In Chapter 3, we present the major challenges of future M2M cellular networks such as spectrum scarcity problem, support for low-power, low-cost, and numerous number of devices. As being an integral part of the future IoT, the true vision of M2M communications cannot be reached with conventional solutions that are typically cost inefficient. To this extent, we present a complete fundamental understanding and engineering knowledge of cognitive radios, heterogeneous network model, and power and cost challenges in the context of future M2M cellular networks. Furthermore, we highlight the main challenges in CR systems that would enable practical implementations.

As a step to address the CR challenges, in Chapter 4, we present a spectrum monitoring algorithm for OFDM-based cognitive radios by which the primary user reappearance can be detected during the secondary user transmission. The proposed technique reduces the frequency with which spectrum sensing must be performed and greatly decreases the elapsed time between the start of a primary transmission and its detection by the secondary network. The OFDM impairments such as power leakage, Narrow Band Interference (NBI), and Inter-Carrier Interference (ICI) are investigated and their impact on the proposed technique is studied. Both analysis and simulation show that the *energy ratio* algorithm can effectively and accurately detect the appearance of the primary user. We consider the algorithm complexity in comparison to the conventional energy detector.

In Chapter 5, we present an ultra low power wideband spectrum sensing architecture by

utilizing a one-bit quantization at the CR receiver. The impact of this aggressive quantization is quantified and it is shown that the proposed method is robust to low signal-to-noise ratios. Two different architectures are considered. The first approach assumes the Fast Fourier Transform (FFT) based detection with the introduction of the one bit quantizer. In the second technique, a window-based autocorrelation is utilized to estimate the power spectral density of the quantized signal. We derive closed-form expressions for both false alarm and detection probabilities for the fist approach and we analytically provide a proof for the autocorrelation detector showing the impact of the aggressive quantization on the autocorrelation function. For both techniques, the sensing performance and the analytical results are assessed through comparisons with respective results from computer simulations.

In Chapter 6, we mainly address couple of challenges for the practical implementation side for both LTE-MTC and NB-IoT systems. For LTE-MTC systems, we present an evaluation to the conventional cell search and initial synchronization algorithms subject to the new system requirements. The performance of most of the algorithms can be enhanced by utilizing time averaging on the account of increasing the processing time. Furthermore, we present, analyze, and evaluate a frequency tracking technique that relies on the repetitive nature of the MTC broadcast channel. Moreover, we present a procedure for NB-IoT cell search and initial synchronization subject to the special system design. In all cases, by simulating exact LTE-MTC and NB-IoT systems, the performance of various algorithms is obtained with the expected time budget to meet LTE-MTC and NB-IoT specifications.

In Chapter 7, we present a brief summery of our investigation and some important conclusions. We also suggest some potential topics for future research.

Chapter 2

Background and Literature Review

In this chapter, a brief background pertaining to the main topics of this thesis is given, including cognitive radio, spectrum sensing and monitoring, OFDM systems, legacy LTE systems, and next generation LTE systems. It also summarizes recent works that relate to the problems studied in this thesis.

2.1 Cognitive Radio

The electromagnetic radio frequency (RF) spectrum is a scarce natural resource, the use of which by transmitters and receivers is typically licensed by governments. Static spectrum access is the main policy for the current wireless communication technologies. Under this policy, fixed channels are assigned to licensed users or primary users (PUs) for exclusive use while unlicensed users or secondary users (SUs) are prohibited from accessing those channels even when they are unoccupied. Nowadays, it becomes obvious that this frequency allocation scheme cannot accommodate the constantly increasing demands of higher data rates. On the contrary, it has been reported that localized temporal and geographic spectrum utilization is extremely low [19]. Cognitive radio has emerged as an innovative technology to solve this spectrum under-utilization problem in the next generation networks [20]-[21]. Following its introduction, a great deal of effort has been expended to improve the efficiency of cognitive radio networks. These works have been dedicated to develop technologies that either exploit opportunities in time, frequency, and space domains or allow SUs to coexist with PUs in the same spectrum bands with minimal interference.

Generally, there are three different models for the cognitive radio networks (CRN): the

interweave, the underlay, and the overlay models. First, in the interweave network model, unlicensed or secondary users are not allowed to access an occupied band by the licensed or primary user. In fact, the Federal Communications Commission (FCC) is currently developing new spectrum policies that will allow SUs to opportunistically access a licensed band when the PU is absent [22]. In these networks, the CR has to identify the available sub-bands of the radio spectrum, or equivalently the spectrum holes, that are under-utilized (in part or in full) at a particular instant of time and specific geographic location. Therefore, the fundamental task for CR is to sense the spectrum in order to detect whether the PU is present or not. Indeed, industrial standardization bodies have preferred the interweave cognitive radio model not only due to its applicability for these low under-utilization usage of the radio spectrum, but also due to the fact that the interweave model can provide sufficient reliability and reasonable guaranteed QoS. As a consequence, standards such as IEEE 802.22, IEEE 802.11af, and Ecma-392 have been built to utilize the interweave network model.

Second, in the underlay network model, the coexistence of primary and secondary users is allowed and hence the network is also termed as a spectrum sharing network [23][24]. However, PUs are always allocated a higher priority to use the spectrum than SUs. Furthermore, the sharing must be maintained under the PU's predefined interference constraint (i.e., a predefined interference threshold which is also termed interference temperature). Due to this constraint, the underlay technique is mainly useful for short range communications. Third, in overlay cognitive networks, SUs and PUs are allowed to transmit concurrently. The defining assumption made in the current overlay models is that the primary message is known to the secondary transmitter in prior [24]. There are two main approaches to realize this model: (1) with the help of advanced coding techniques [25] such as dirty paper coding (a technique which completely mitigates a priori known interference over an input power constrained additive white Gaussian noise (AWGN) channel), where the secondary user can precode the transmitted stream in order to effectively null the interference at the secondary receiver. While this approach violates the cognitive radio principle of protecting the primary users, it provides a theoretical upper bound on the maximum throughput achievable by the secondary users. (2) The secondary user splits its own power into two parts, one used to raise the primary user power in order to mitigate the interference effect caused by the secondary

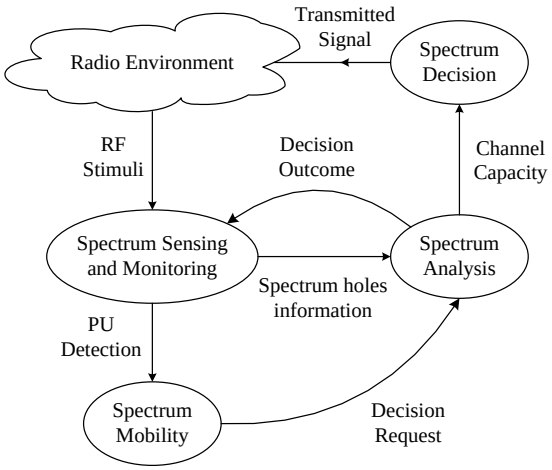

Figure 2.1: Dynamic Spectrum Management Framework for interweave network model [27][28]

user data and the other part is utilized to carry the secondary user data [26].

2.2 Spectrum Sensing in Interweave Network Model

The basic concept behind interweave cognitive radio is to exploit the available under-utilized spectral resources by reusing unused spectrum in an opportunistic manner [20][27][29]. Therefore, the process of realizing efficient spectrum utilization using the interweave cognitive radio technology requires a dynamic spectrum management framework (DSMF) which provides a complete architecture for the model with detailed functionalities. The DSMF proposed in [28] is adopted due to its clear functionality, well-defined interfaces among various blocks, and relevance to our discussion. This DSMF consists of four main blocks: spectrum sensing and monitoring, spectrum analysis, spectrum decision and spectrum mobility, as shown in Fig. 2.1. The tasks required for adaptive operation in one cognitive cycle can be briefly discussed as follows [20]:

- *Spectrum sensing and monitoring:* A cognitive radio senses the available spectrum, captures their information, and then detects the spectrum holes. Spectrum sensing is also able to capture the proper observations about the spectrum holes in order to assist the analysis stage for the spectrum characterization. If the CR is already camping on

a spectrum slice for communication, then the occupied narrowband is monitored to determine whether the original licensed user reappears or not.

- *Spectrum analysis:* The characteristics of the spectrum holes that are detected through spectrum sensing are estimated. The primary user activity and the spectrum band information such as operating frequency and bandwidth have to be considered for individual holes. In fact, it is essential to define parameters such as interference level, channel error rate, path-loss, link layer delay, and holding time that can represent the quality of a particular spectrum band.

- *Spectrum decision:* A cognitive radio determines the data rate, the transmission mode, and the bandwidth of the transmission. Then, the appropriate spectrum band is chosen according to the spectrum characteristics and user requirements.

- *Spectrum mobility:* is the ability of a CR to vacate the channel when a licensed user is detected.

Spectrum sensing is the most important component for the establishment of interweave cognitive radio network. Indeed, spectrum sensing is the task of obtaining awareness about the spectrum usage [30][3]. Spectrum sensing and monitoring techniques can be classified based on the size of the band of interest as shown in Fig. 2.2. Narrowband sensing/monitoring [29][3] tackles the problem of deciding whether a particular slice of the spectrum is a hole or not. On the contrary, wideband spectrum sensing [30][31] is based on classifying individual slices of a wideband to be either occupied or vacant. As a matter of fact, both sensing procedures are required during the cognitive cycle. We have to emphasize that there are usually two distinct phases for the PU detection in interweave networks. During the initial sensing phase, wideband sensing is required to provide varieties for the available spectrum holes. This piece of information assists the spectrum analysis and decision logic to characterize the spectrum holes and to select the proper suitable hole that best fits the cognitive radio requirements.

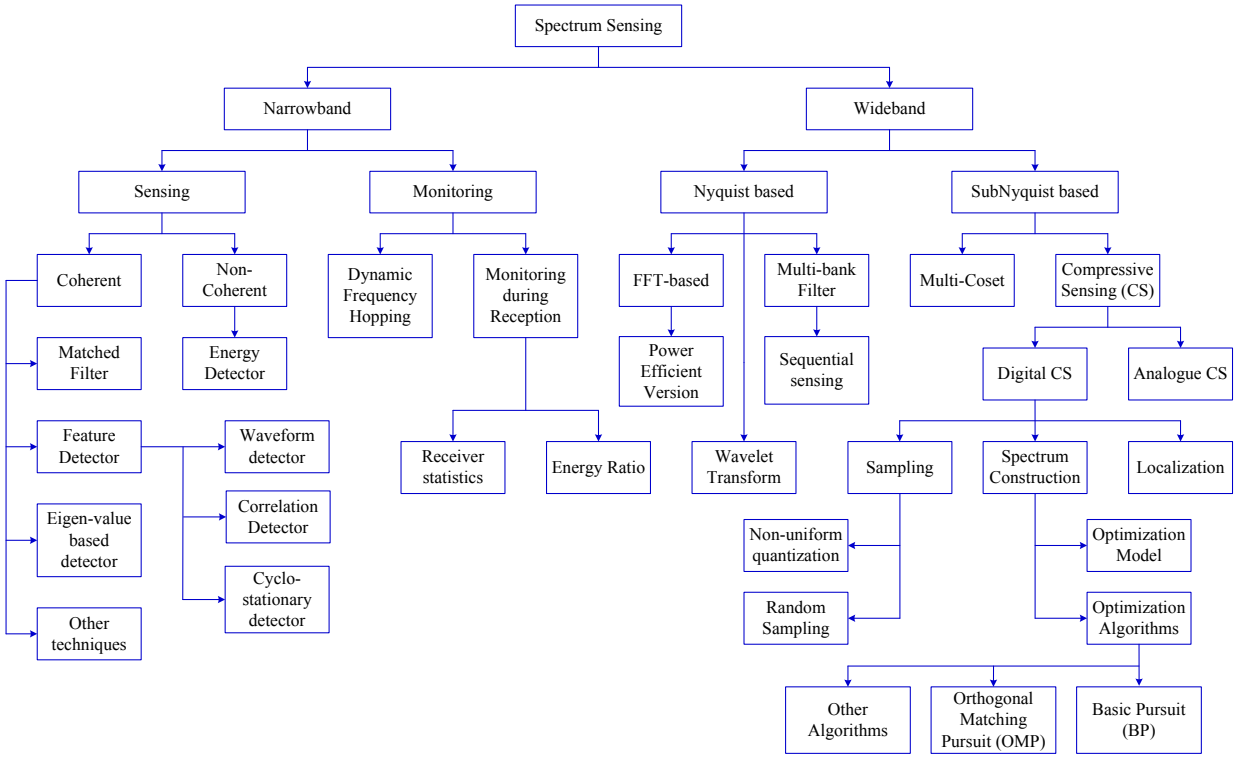

Figure 2.2: Classification for the spectrum sensing approaches based on the bandwidth size.

2.3 Narrowband Sensing and Monitoring

In interweave networks, prior to communication, secondary user must sense the spectrum to detect whether it is available or not. Since the CR users do not access the spectrum during the sensing period, this period is called the quiet period (QP) [32]. As a result of this limited sensing duration, only a certain accuracy can be guaranteed for spectrum sensing results. Moreover, the spectrum efficiency is decreased as some portion of the available time slot is used for sensing instead of data transmission [33]. One approach to reduce the effect of the wasted time in QPs is to employ Dynamic Frequency Hopping (DFH) which assumes that the SU is scheduled to switch from one band to another based on a prior knowledge of the hopping pattern [34][35]. During communication, SU must be able to detect very weak signals generated by the primary user in order to quickly vacate the occupied spectrum. Thus, primary user detection is essential by continuously monitoring the utilized spectrum to release the spectrum. Traditionally, spectrum monitoring techniques rely on the periodic spectrum sensing during quiet periods [36]. The processing is usually applied over the received signal

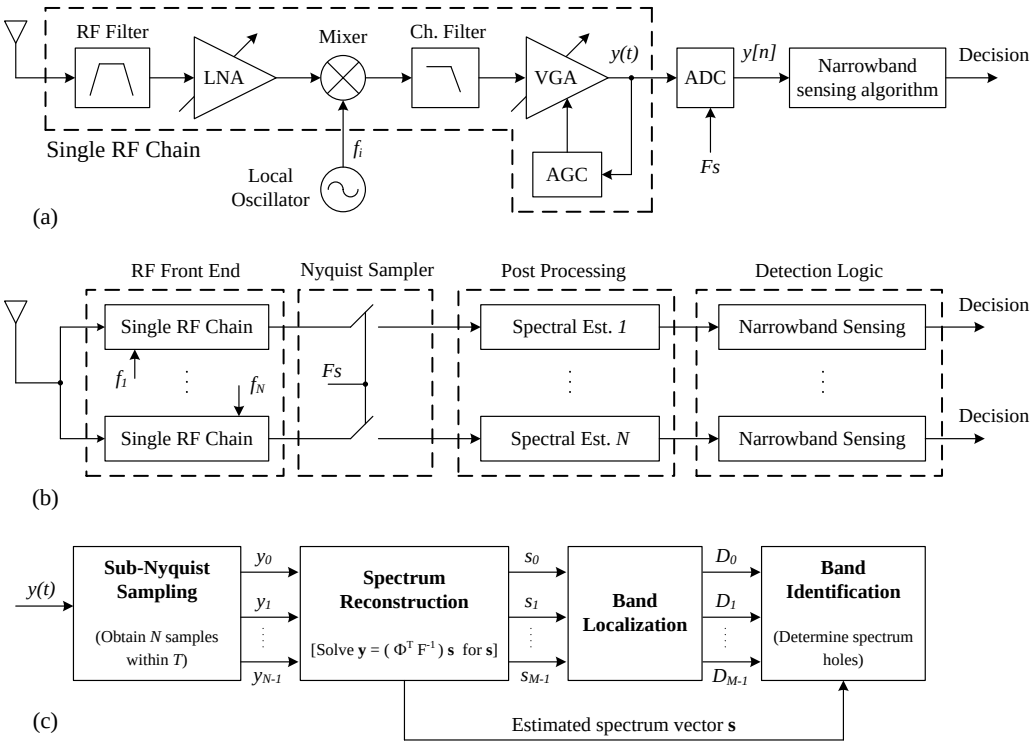

Figure 2.3: Basic block diagrams for various spectrum sensing techniques: (a) Block diagram for the narrowband sensing architecture at the SU receiver. (b) General block diagram for the Nyquist-based wideband sensing techniques. (c) Block diagram for the digital logic of the wideband compressive sensing approach.

at the SU to explore a specific feature to the primary user.

In general, the problem of narrowband spectrum sensing is to decide whether a particular slice of the spectrum is "available" or not. That is, in its simplest form, it is required to discriminate between the two hypotheses defined by (2.1), where $x(n)$ represents a primary user's signal observed at the SU receiver, $w(n)$ is a complex symmetric AWGN with zero-mean and variance σ_w^2 such that $w(n) \sim \mathcal{CN}(0, \sigma_w^2)$, and n represents time. The received signal $y(n)$ can be vectorized to probably represent the received signal at different antenna ports in case of multi-receive antenna systems.

$$\begin{cases} \mathcal{H}_0 : \ y(n) \ = \ w(n) \\ \mathcal{H}_1 : \ y(n) \ = \ x(n) + w(n) \end{cases} \tag{2.1}$$

The performance of the detection algorithm can be summarized with two probabilities: the probability of miss-detection P_{MD} and the probability of false alarm P_{FA} [37][38]. P_{MD}

is the probability of miss-detecting a primary signal when it is truly present. For a given decision statistic Λ, the miss-detection probability can be defined by $P_{MD} = \Pr\big[\Lambda < \gamma \,|\, \mathcal{H}_1\big]$ where γ is a threshold that should be determined. On the other hand, P_{FA} is the probability that the test incorrectly decides that the primary user is present when it is actually not. The false alarm probability can be defined by $P_{FA} = \Pr\big[\Lambda > \gamma \,|\, \mathcal{H}_0\big]$. Generally, P_{FA} should be kept as small as possible in order to prevent under-utilization of transmission opportunities while P_{MD} needs to be minimized.

Typically, the performance of a detector is quantified in terms of its receiver operating characteristics (ROC) curve, which represents the probability of miss-detection P_{MD} as a function of the probability of false alarm P_{FA}. By varying the threshold γ, the operating point of a detector can be chosen anywhere along its ROC curve. Clearly, the fundamental problem of detector design is to choose detection criteria, and to set the decision threshold γ to achieve good detection performance. These matters are treated in detail in the literature of detection theory. Detection algorithms are either designed in the framework of classical statistics, or in the framework of Bayesian statistics [39]. In the classical approach, either $\mathcal{H}_0$ or $\mathcal{H}_1$ is deterministically true, and the objective is to minimize P_{MD} subject to a constraint on P_{FA}; this is known as the Neyman-Pearson (NP) criterion. In the Bayesian framework, by contrast, it is assumed that the source selects the true hypothesis at random, according to some priori probabilities. The objective is to minimize the so-called Bayesian cost.

2.3.1 Narrowband Spectrum Sensing Approaches

In this section, we will be focusing on the most popular narrowband sensing techniques to which most of the recent research activities have been directed. Thus, matched filter detection, energy detection, and cyclostationary feature detection will be considered. A general block diagram for these approached is shown in Fig. 2.3-(a). Also, a brief summary of the main approaches is introduced in Table 2.1.

1. **Energy Detection**: It is a non-coherent detection method that avoids the need for prior knowledge of the PUs and the complicated receivers required by a matched filter [3][38]. The signal is detected by comparing the output of the energy detector

Sensing techniques	Advantages	Disadvantages
Matched-filtering	• Optimal performance. • Low computational cost.	• Require prior information of the primary user.
Energy detection	• No prior information. • Low computational cost.	• Poor performance for low SNR. • Cannot differentiate users.
Cyclostationary feature	• Valid in low SNR region. • Robust against interference.	• Need partial prior information. • High computational cost.

Table 2.1: Pros and cones for different narrowband sensing techniques

with a threshold which depends on the noise floor. Both the implementation and the computational complexity are relatively low. A major drawback is that it has poor detection performance under low SNR scenarios and cannot differentiate between the signals from PUs and the interference from other cognitive radios. Also, it can not detect spread spectrum signals since they seem to be noise.

2. **Matched-filtering Detection**: Known patterns are usually utilized in wireless systems to assist synchronization or for other purposes [40][41]. Such patterns include preambles, regularly transmitted pilot patterns, spreading sequences *etc.* In the presence of a known pattern, sensing can be performed by correlating the received signal with a known copy of itself. This approach represents the optimal solution for spectrum sensing since it maximizes the signal-to-noise ratio in the presence of additive noise. However, it relies on prior knowledge of the PUs and requires cognitive radios to be equipped with carrier synchronization and timing devices, leading to increased implementation complexity.

3. **Feature Detection**: First, a subclass of feature detectors, known as waveform detector, relies on a prior knowledge of the PU signal construction. Usually, preambles, mid-ambles, pilot carrier, and/or spreading sequences are intentionally added to the PU

signal to help synchronization process [3]. Waveform detection is a coherent sensing method that makes use of the known signal patterns. In the presence of known signals, the decision statistic is formed by correlating the received signal to a true-copy of the know pattern. The output is then compared to a threshold value in order to detect the presence or absence of a PU [42]. Second, another subclass of feature detectors depends on the second order statistics of the received signal. In some cases such as OFDM, the feature is attached to the periodicity of the PU signal itself and second order statistics such as autocorrelation can reveal the explicit correlation structure imposed by the insertion of CP at the PU transmitter. Due to the popularity of OFDM in advanced communication systems nowadays, a special attention has been made to design good decision statistic that provides good detection performance and requires the minimum set of known information about the OFDM signal [43][44]. Third, since PU signals are typically digitally modulated, the second order periodicity inherited in these signals exploit a cyclostationary feature. These detection algorithms can differentiate noise from primary users' signals. Usually, cyclostationary features arise due to the periodicity in the signal or in its statistics. Indeed, cyclostationary signals exhibit second order periodicity. Thus, the Cyclic Autocorrelation Function (CAF) at a cyclic frequency α is defined by (2.2) where τ is the lag value, $\mathbb{E}$ denotes expectation, and $(*)$ refers to the conjugate operation. From the implementation perspective, the CAF is estimated based on the received samples, $y(n)$, and prior knowledge to α and/or τ [45]. It acts as a decision statistic which is compared to a threshold to decide whether a PU is present or not.

$$R_y(\alpha,\tau) \quad = \quad \frac{1}{N}\sum_{n=0}^{N-1}\mathbb{E}\Big[y(n)y^*(n+\tau)\Big]e^{-j\alpha n} \tag{2.2}$$

4. **Other techniques**: Due to the limitations of practical system implementation and coherent detection for the conventional narrowband sensing techniques, more investigations and innovative solutions have been recently presented. Among those methods, the eigenvalue based detection [46][47] has been proposed. Some communication signals impart a specific known structure to the covariance matrix which can be obtained based on the correlation among the received signal samples. In general, advanced communi-

cation systems, that include digital modulation, multiple antenna system, Space-Time Block Code (STBC), Space-Frequency Block Code (SFBC), or OFDM, impose specific structure to the primary signal characteristics. Research efforts are directed to design detectors for each of these properties to explore the spectrum occupancy of the primary signal.

2.4 Wideband Spectrum Sensing

Wideband spectrum sensing techniques aim to sense a frequency bandwidth that exceeds the coherence bandwidth of the channel. Based on the sampling frequency, two main classes of solutions are available to deal with the wideband sensing problem. The first approach to realize wideband sensing assumes that it is feasible to sample the desired spectrum by the ordinary Nyquist rate [30]. The common challenge in these approaches is the high computational complexity attached to the required ultra high sampling rates, the high computational complexity of the solutions, and the required sensing time especially when practical considerations are taken into account such as the Automatic-Gain-Control (AGC) settling time, the switching time for the Phase-Locked-Loop (PLL), and the processing delay.

The second approach to perform wideband sensing is based on the sub-Nyquist techniques. These approaches [48] are utilized to relax the long sensing delay or the higher computational complexity and hardware cost resulted from the high sampling rate implementations. Compressive sensing [30] becomes a promising candidate to realize this sub-Nyquist approach. Here, a signal can be efficiently acquired using relatively few measurements by which unique representation of the signal can be found based on the signal's sparsity or compressibility in some domain. Other techniques such as multi-cosets [49] [50] can also be used to reconstruct the spectrum from fewer samples. The idea here is to chose a sampling sequence that enables this reconstruction. In this section, we introduce the basic concepts for the conventional approaches to perform wideband sensing. Also, we include the recent research advances introduced for each approach to enhance its feasibility.

2.4.1 Nyquist-based Wideband Sensing Approaches

A simple approach of wideband spectrum sensing is to directly acquire the wideband signal using a standard ADC and then employ digital signal processing techniques to detect spectral opportunities. A general block diagram for these approached is shown in Fig. 2.3-(b). We present the most common approaches along with their recent enhancements. Various techniques are available for the Nyquist-based wideband sensing.

1. **Multiband Sensing or FFT-based Sensing**: An FFT-based technique is originally proposed in [51]. In this approach, the wideband signal is sampled by a conventional ADC at a high sampling rate. The samples are then divided into segments, where the discrete Fourier transform is obtained for each segment individually. The wideband spectrum from various segments are utilized to obtain an estimate for the power spectral density which is then divided into a series of narrowband spectra. Spectral opportunities are detected using binary hypotheses tests for various narrowbands.

2. **Wavelet-based Sensing**: A wavelet-based spectrum sensing algorithm is proposed in [52][53]. In this algorithm, the power spectral density of the wideband spectrum was modelled as a train of consecutive frequency sub-bands, where the PSD is smooth within each sub-band but exhibits discontinuities and irregularities on the transitions of two neighbouring sub-bands. Unlike conventional Fourier transform, wavelet transform has been used as it provides information about exact location of frequency transition locations and spectral densities. Therefore, the wavelet transform is used to locate the singularities of the wideband PSD. The trade-off is usually the performance versus the sensing time and complexity.

3. **Filter-bank Sensing**: A bank of prototype filters (with different shifted central frequencies) is presented in [54] to process the received wideband signal. The baseband can be directly estimated by using a prototype filter. Other bands can be obtained by modulating the prototype filter so that its center frequency is adjusted to select the desired band. In each band, the corresponding portion of the spectrum for the wideband signal is down-converted and filtered to form a baseband version to which

a narrowband sensing algorithm is applied. This algorithm can therefore capture the dynamic nature of wideband spectrum by using low sampling rates. Unfortunately, due to the parallel structure of the filter bank, the implementation of this algorithm requires a large number of RF components.

2.4.2 Sub-Nyquist Wideband Sensing Approaches

Due to the drawbacks of high sampling rate or high implementation complexity in Nyquist systems, sub-Nyquist approaches are drawing more and more attention in both academia and industry. Sub-Nyquist wideband sensing refers to the procedure of acquiring wideband signals using sampling rates lower than the Nyquist rate and detecting spectral opportunities using these partial measurements. In addition to the multi-coset approach, compressive sensing is the most common technique that facilitate the sub-Nyquist wideband sensing. Thus, we will briefly provide some background about compressive sensing in cognitive radio networks just for reference.

There are some basic definitions that need to be considered in the conventional compressed sensing theory [48]:

- $\mathbf{x}$ is an $M \times 1$ vector (i.e. $\mathbf{x} \in \mathbb{C}^M$) which is sparse in the basis of Ψ where Ψ is an $M \times M$ transform matrix (i.e. $\Psi \in \mathbb{C}^{M \times M}$).

- $\mathbf{s}$ is an $M \times 1$ sparse vector (i.e. $\mathbf{s} \in \mathbb{C}^M$) which has only K non-zero elements such that $K \ll M$. Finally, we have the transform relation $\mathbf{x} = \Psi\, \mathbf{s}$.

- $\mathbf{y}$ is $N \times 1$ vector (i.e. $\mathbf{y} \in \mathbb{C}^N$) which represents the available measurements such that $N \ll M$. Assume that $\mathbf{y}$ can be represented as M linear combinations of $\mathbf{x}$ such that $\mathbf{y} = \Phi^T\, \mathbf{x}$ where Φ is the projection matrix or the measurement matrix and $\Phi \in \mathbb{R}^{M \times N}$.

- When Nyquist sampling is used, the measurement matrix is a simple identity matrix (i.e. $\Phi = I_M$), therefore the measured vector is the same as the Nyquist samples.

Compressive sensing theory attempts to recover the exact or very accurate version of the original sparse signal $\mathbf{s}$ from few measurements $\mathbf{y}$ by solving the linear set of equations $\mathbf{y} = \Phi^T\, \Psi\, \mathbf{s} = A\, \mathbf{s}$, where A is the sensing matrix such that the signal $\mathbf{s}$ can be reconstructed

from few measurements represented by the signal $\mathbf{y}$. In fact, the classical theory of linear algebra has some basic rules to solve this linear system of equations. If there are fewer measurements than unknowns ($N < M$) which is the case, then the problem is under-determined even when A has full rank. Knowledge of $A\,\mathbf{s} = \mathbf{y}$ restricts $\mathbf{s}$ to an affine subspace of $\mathbb{C}^M$, but does not determine $\mathbf{s}$ completely. In order to have an accurate and guaranteed solution to the under-determined system, the sensing matrix should be properly selected to satisfy some constraints. A large number of algorithms that attempt to solve the linear system within the broader field of compressed sensing have been studied using the restricted isometry property (RIP) for the matrix A [55]. This property characterizes matrices which are nearly orthonormal, at least when operating on sparse vectors.

Compressive sensing theory was firstly introduced to sense wideband spectrum in [56]. This technique used fewer samples closer to the information rate, rather than the Nyquist rate, to perform wideband spectrum sensing. To implement compressive sensing in cognitive networks, [56] shows the detailed procedure which is shown in Fig. 2.3-(c). First, a sub-Nyquist sampler is required to obtain the few measurements. Second, the spectrum is reconstructed from the measured samples. Third, a localization and identification for the occupied sub-bands are explored to finalize the wideband sensing decisions.

1. **Sub-Nyquist Sampling**: Let the received signal $y(t)$ be sampled by the conventional Nyquist rate. After conversion, the discrete time signal can be denoted by $y(n) = y(t)|_{t=nT_0}$ where T_0 is the Nyquist sampling period. Assume that the sensing period $T_{sensing} = MT_0$, therefore we have traditionally M digital samples from the signal $y(t)$ within the time period $T_{sensing}$. Instead, the digital receiver converts the continuous-domain signal $y(t)$ to a discrete sequence $\mathbf{y} \in \mathbb{C}^N$ of length N such that $N \ll M$. This process is defined as the sub-Nyquist-rate sampling process. One solution is the recurrent and non-uniform sampling that is equivalent to choosing some samples from a uniform grid, which can be obtained using a sampling rate f_s that is higher than the Nyquist rate. The uniform grid is then divided into blocks of M consecutive samples, and in each block N samples are retained such that $N \leq M$ while the rest of samples are skipped. The process is repeated periodically to continuously achieve sub-Nyquist sampling.

Another realization for non-uniform sampling is the random sampler which is the class of non-recurrent sampling. The sampling process does not show any periodicity and can only be described statistically. The theoretical framework is based on the random sampling theory. Unlike uniform sampling, the Nyquist rate is no longer the barrier under a random sampling scheme [57] [58]. It is possible to unambiguously reconstruct a class of spectrally sparse signals that is sampled randomly below the Nyquist rate.

2. **Spectrum Reconstruction**: The main challenge for compressive sensing is the spectrum reconstruction part. It is required to accurately reconstruct the signal spectrum $\mathbf{s}$ represented by M frequency samples at the Nyquist rate from the available measurement set $\mathbf{y}$ which has a reduced size of $N < M$ elements. If $\mathbf{s}$ represents the spectrum of the Nyquist rate samples $\mathbf{x}$, then the transform matrix Ψ represents the inverse discrete Fourier transform matrix such that $\Psi = F^{-1}$ where $F \in \mathbb{C}^{M\times M}$ is the discrete Fourier transform matrix. Then, we have a linear set of equations $\mathbf{y} = \left(\Phi^T F^{-1}\right)\mathbf{s} = A\,\mathbf{s}$ where A is the sensing matrix. Assuming that the sensing matrix $A_{N\times M}$ is known, of course with some constraints, one can minimize the error between the measurements $\mathbf{y}$ and the linear system of equations $A\,\mathbf{s}$ to find the best guess for $\mathbf{s}$.

   The reconstruction of sparse signals can be reduced to an optimization problem with efficient algorithms. One of them is the Orthogonal Matching Pursuit (OMP) which formulates the problem as finding the sparsest solution of linear equations $\mathbf{y} = A\,\mathbf{s}$ such that the linear programming is used to find the solution based on the optimization problem given by (2.3). Unfortunately, ℓ_0 minimisation is computationally intractable. In fact, in complexity theory, ℓ_0 minimisation can be classified as an NP-hard problem in general [59]. An NP-hard (or Non-deterministic Polynomial hard) is at least as hard as the NP-Complete problems which is the problem of solving all possible set of NP problems. When $\mathbf{s}$ is sparse, ℓ_0 minimisation is often correct, but very difficult to compute. The Basis Pursuit (BP) [60] method considers a convex relaxation of (2.3). For certain RIP properties, the sparse signal can be exactly recovered via the ℓ_1 minimization, given by (2.4). The necessary condition that every $2K$ columns of A have to be linearly independent, has to be strengthened somewhat. The precise condition is

being RIP of order $2K$ [55] which is obeyed by many types of matrices (e.g. Gaussian random matrices obey the RIP with high probability).

$$\hat{\mathbf{s}} = \arg\min_{\mathbf{s}} \|\mathbf{s}\|_0 , \text{ s.t. } \mathbf{y} = A\,\mathbf{s} \tag{2.3}$$

$$\hat{\mathbf{s}} = \arg\min_{\mathbf{s}} \|\mathbf{s}\|_1 , \text{ s.t. } \mathbf{y} = A\,\mathbf{s} \tag{2.4}$$

3. **Localization and Identification**: After the reconstruction of the wideband spectrum, the spectrum holes are localized and identified so that the SU can decide which band is suitable for its transmission. The spectrum is assumed to be K sparse. The typical approach here is to obtain the wavelet transform for the estimated spectrum and hence the spectrum discontinuities can be obtained. The locations of those discontinuities determine the boundaries for the occupied and vacant bands. Now, the bands are localized by having proper corner frequencies for both vacant and occupied bands. The last step is to distinguish which band is vacant and which is occupied. In fact, this reduces the problem of wideband sensing into a narrowband one in which the spectrum is known. Therefore, a simple energy detection can do the job of identifying the band type of being whether a spectrum hole or not.

In fact, compressive sensing has concentrated on finite-length and discrete-time signals. Thus, innovative technologies are required to extend the compressive sensing to continuous-time signal acquisition, i.e., implementing compressive sensing in analogue domain. To realize the analogue compressive sensing, an analogue-to-information converter (AIC), which could be a good basis for the above-mentioned algorithms, is proposed in [61]. For sparse input signals, AIC promises greatly reduced digital data rates (matching the information rate of the signal). The AIC-based model consists of a pseudo-random number generator, a mixer, an accumulator, and a low-rate sampler [62][63]. The pseudo-random number generator produces a discrete-time sequence that demodulates the signal $x(t)$ by a mixer. The accumulator is used to sum the demodulated signal for T_s seconds, while its output signal is sampled using a low sampling rate. After that, the sparse signal can be directly reconstructed from partial measurements using compressive sensing algorithms.

2.5 OFDM Systems

OFDM is a multi-carrier modulation technique that is used in many wireless systems and proven as a reliable and effective transmission method. In an OFDM scheme, a large number of orthogonal, overlapping, narrow band sub-channels or sub-carriers, transmitted in parallel, divide the available transmission bandwidth. The separation of the sub-carriers is theoretically minimal such that there is a very compact spectral utilization. The attraction of OFDM is mainly due to how the system handles the multipath interference at the receiver. Multipath generates two effects: frequency selective fading and Inter Symbol Interference (ISI). The "flatness" perceived by a narrow-band channel overcomes the former, and modulating at a very low symbol rate, which makes the symbols much longer than the channel impulse response, diminishes the latter. Using powerful error correcting codes together with time and frequency interleaving yields even more robustness against frequency selective fading, and the insertion of an extra guard interval between consecutive OFDM symbols can reduce the effects of ISI even more.

In general, OFDM reduces the need for complex equalizers at the receiver side. Other advantages of OFDM include robustness against NBI, scalability, and easy implementation using FFT algorithm. OFDM can be also used as a multiple access technique, namely Orthogonal Frequency Division Multiple Access (OFDMA), where independent sources can share both time and frequency to transmit their data. Due to these advantages, OFDM is utilized as the physical layer modulation technique for so many wireless systems including DVB-T/T2, LTE, IEEE 802.16d/e, IEEE 802.11a/g, and the first cognitive standard IEEE 802.22. For cognitive radios, OFDM is preferred but also it has some challenges that have been studied [64].

On the other hand, there are some challenges in OFDM systems, the large dynamic range of the signal (also referred as peak-to-average power ratio (PAPR)) and its sensitivity to frequency errors which may result in ICI. Moreover, the finite time-window in the receiver DFT will result in a spectral leakage from any in-band and narrow band signal onto all OFDM sub-carriers. In this introduction, we will focus on the ICI reasons and solutions.

2.5.1 ICI In OFDM Systems

OFDM system may have an ICI, which means a sub-carrier frequency component is influenced by other sub-carrier frequency components. Generally, the observed frequency domain signal at each sub-carrier has three components [65]: (1) The original transmitted symbol whose magnitude and phase are distorted due to the effects of Carrier Frequency Offset (CFO), Sampling Frequency Offset (SFO), and the channel. (2) An ICI term whose source may be the carrier signal distortion or the sampling clock distortion or both. (3) The AWGN noise. The bit error rate of the OFDM system is significantly degraded by having considerable ICI term, and hence traditional OFDM system design should be able to carefully reduce ICI effect.

In general, there are two types of distortion associated with the carrier signal [66]. One is the Phase Noise (PN) due to the instability of carrier signal generators used at the transmitter and receiver, which can be modelled as a zero-mean Wiener random process. The ICI from PN can be estimated and then compensated for all sub-carriers by applying the common phase error over the pilot tones. Actually, the effect of PN can be greatly reduced by increasing the sub-carrier spacing, Δf. We will (optimistically) assume that Δf is large enough such that the ICI introduced by the PN is neglected with respect to the ICI generated by either CFO or SFO.

The other type of distortion is the carrier frequency offset caused by the difference between the carrier frequencies generated by the transmitter and receiver oscillators, or by the Doppler frequency shift. If f_{offset} denotes the frequency offset between the transmitter and receiver, then the normalized CFO is defined as $\varepsilon = \varepsilon_i + \varepsilon_f = f_{\text{offset}}/\Delta f$ where ε_i is the integer part of the normalized CFO while ε_f is the fractional part. In fact, if ε is only integer (i.e: $\varepsilon_f = 0$), this means that the sub-carriers are shifted by a non-zero integer number. Although the orthogonality among the sub-carrier frequency components is not destroyed in this case, the receiver will decode wrong symbols as the symbol order has been changed by this frequency shift. Therefore, powerful estimation and compensation techniques, that can guarantee a zero miss detection probability for the CFO integer part, should be used even if the complexity is relatively high. Even after estimating and compensating both integer and fractional CFO,

a residual CFO, ε_r, which represents the remaining uncompensated fractional CFO always exist. The SNR degradation, $\mathrm{SNRD}_{\mathrm{CFO}}$, due to this residual CFO is analytically analysed in [65]. The analysis shows that in the AWGN channel and when the number of sub-carriers is large, the SNR degradation is given by,

$$\mathrm{SNRD}_{\mathrm{CFO}} \quad = \quad \frac{10}{3\ln(10)}\left(\pi\,\varepsilon_r\right)^2\mathrm{SNR} \qquad \mathrm{dB} \tag{2.5}$$

The most important sampling clock distortion that causes ICI is the sampling frequency offset between the transmitter and receiver which mainly occurs due to the mismatch between the transmitter and receiver oscillators. SFO gives rise to the phase offset between the transmitter and receiver clocks to vary with time such that the received continuous-time waveform is sampled at an interval of $(1+\delta)\,T_s$ instead of T_s where T_s is the ideal sampling period and δ (usually expressed in part per million or ppm) is the normalized difference between the periods of the two clocks. If δ is estimated by the receiver, the compensation can be carried out by feeding the clock generator with the amount of time shift in order to adjust the clock or by interpolating the received time domain samples with a fractional delay [67]. In both cases, there will be a residual SFO, δ_r, by which the SNR over different frequency sub-carriers is degraded. Actually, the SNR degradation due to SFO in the k^{th} sub-carrier, $\mathrm{SNRD}_{\mathrm{SFO}}(k)$, is analysed in [68] and is given by,

$$\mathrm{SNRD}_{\mathrm{SFO}}(k) \quad = \quad 10\log_{10}\left(1+\frac{1}{3}\left(\pi\,\delta_r\,k\right)^2\mathrm{SNR}\right) \qquad \mathrm{dB} \tag{2.6}$$

2.5.2 OFDM System Block Diagram

For the functionality level, a typical block diagram of the OFDM transmitter and receiver is shown in Figure 2.4. This model is very close to the OFDM system discussed in [64].

At the transmitter side, data coming from the source is firstly segmented into blocks where each block is randomized, channel encoded, and interleaved separately. After interleaving, the data is modulated by a QAM mapper. The frequency domain OFDM frame is constructed by combining: (a) One or more training symbols or preambles that are used for both time and frequency synchronization at the receiver side. (b) The modulated data. (c) The BPSK modulated pilots which are useful for data-aided synchronization algorithms employed by the receiver.

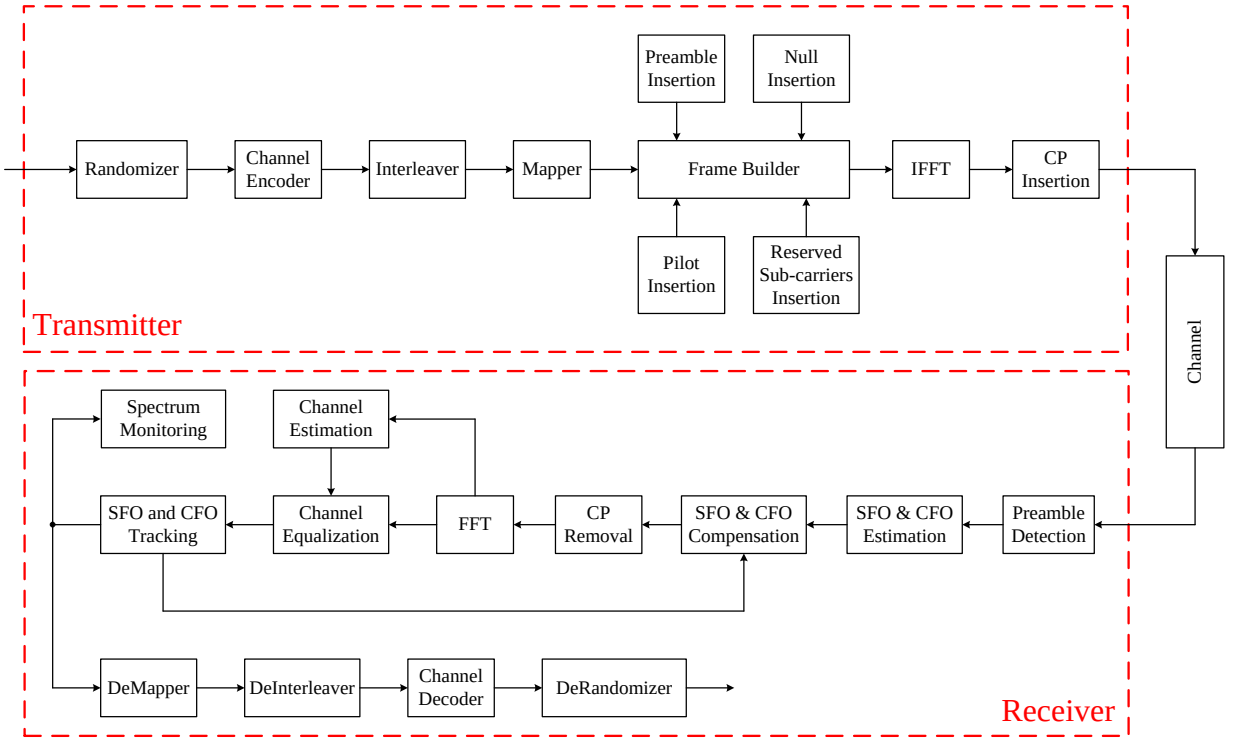

Figure 2.4: Secondary user transmitter and receiver structures

It should be mentioned that each OFDM symbol has a guard band or a number of null sub-carriers that develop a spectrum mask for the transmitted signal. Each N_s encoded complex data symbols generated by the frame builder are used to construct one OFDM symbol by employing the Inverse Discrete Fourier Transform (IDFT) block that is used to synthesize the OFDM symbol, where N_s denotes the number of sub-carriers per one OFDM symbol. Thus, the n^{th} time-domain sample of the m^{th} symbol can be expressed as given by (2.7) where $C(k,m)$ is the modulated data to be transmitted on the m^{th} OFDM symbol with the k^{th} sub-carrier. To reduce the effect of ISI, the last N_g samples of the time domain OFDM symbol are copied to the beginning of the symbol in order to form a guard time or cyclic prefix.

$$s(n,m) \;=\; \frac{1}{\sqrt{N_s}} \sum_{k=-N_s/2}^{N_s/2-1} C(k,m)\, e^{j2\pi kn/N_s} \tag{2.7}$$

At the receiver, the inverse blocks are applied. After timing synchronization (frame detection, start of symbol timing, and SFO estimation and compensation) and frequency synchronization (CFO estimation and correction), the cyclic prefix is removed. Then, the

received OFDM symbol is transformed again into the frequency domain through an N_s point DFT. The channel is then estimated and the received data is equalized. The complex data output is then mapped to bits again through the De-mapper. De-interleaving, decoding, and De-randomization are applied later to the received block to recover the original source bits.

2.6 Conventional and Next-Generation LTE Systems

2.6.1 Legacy LTE Framework

LTE has been designed as a highly flexible radio access technology to support several system bandwidth configurations including 1.4, 3, 5, 10, 15, and 20 MHz. Radio spectrum access is based on OFDM scheme. In particular, Single Carrier Frequency Division Multiple Access (SC-FDMA) and OFDMA are used in uplink and downlink directions, respectively [69]. Differently from basic OFDM, they allow multiple access by assigning sets of sub-carriers to each individual user. OFDMA can exploit sub-carriers distributed inside the entire spectrum, whereas SC-FDMA can use only adjacent sub-carriers. OFDMA is able to provide high scalability, simple equalization, and high robustness against the time-frequency selective nature of radio channel fading. On the other hand, SC-FDMA is used in the LTE uplink to increase the power efficiency of UEs, given that they are battery supplied.

Radio resources are allocated into the time/frequency domain. In particular, in the time domain they are distributed every Transmission Time Interval (TTI), each one lasting 1 ms. The time is split in frames, each one composed of 10 consecutive TTIs [70]. Furthermore, each TTI is made of two time slots with length 0.5 ms, corresponding to 7 OFDM symbols in the default configuration with short cyclic prefix. Indeed, two types of cyclic prefixes (CP) are defined: the normal CP and the extended CP. For both, a single sub-frame duration is 1ms which is further divided into two slots with equal periods. For the normal CP type, a slot is composed of 7 OFDM symbols. The CP length, say N_g, of the first symbol in each slot is 10 samples and those of the other symbols are 9 samples long. For the extended CP type, a slot consists of only 6 OFDM symbols and the CP length of each symbol is 32 samples.

In the frequency domain, instead, the total bandwidth is divided in sub-channels of 180

kHz, each one with 12 consecutive and equally spaced OFDM sub-carriers. A time/frequency radio resource spanning over two time slots in the time domain and over one sub-channel in the frequency domain is called Physical Resource Block (PRB) and corresponds to the smallest radio resource unit that can be assigned to an UE for data transmission. As the sub-channel size is fixed, the number of PRBs varies according to the system bandwidth configuration (e.g., 25 and 50 RBs for system bandwidths of 5 and 10 MHz, respectively).

On the uplink side, the call is initiated through the Physical Random Access Channel (PRACH) which carries the preamble to the base station (eNodeB in LTE context). The data and control are carried through the Physical Uplink Shared Channel (PUSCH) and Physical Uplink Control Channel (PUCCH), respectively. For the physical downlink channels, there are couple of channels dedicated for information exchange. Downlink data and signalling information are time multiplexed within the subframe. In details, control channels occupy, in each TTI, the first 1 to 3 OFDM symbols over the 14 available. Consequently, data transmission is allowed during the remaining time. Downlink control signalling is carried by three physical channels [71], namely the Physical Broadcast Channel (PBCH), the Physical Downlink Control Channel (PDCCH), and the Physical Control Format Indicator Channel (PCFICH). The PBCH carries the Master Information Block (MIB) which provides the most essential system information such as the system bandwidth and the frame timing. This is in a broadcast mode to which any user can listen. It is mapped to the first 4 OFDM symbols in the second slot of a radio frame [72].

The network provides the UE with Downlink Control Information (DCI) messages that are typically carried by the PDCCH [73]. This DCI carries the essential information by which a UE can decode the coming data. For instance, the adaptive modulation and coding information, the repetition index of the frame, the new data indication and other uplink grants and downlink assignments are transmitted through DCIs. Thus, PDCCH is one of the most important channels since it is the precondition for the correct data decoding. The PDCCH is mapped to the first few symbols of the subframe. The number of OFDM symbols that carry the control information is signalled by a fixed channel, namely the PCFICH. Downlink data are transmitted by the eNB over the PDSCH [74]. As its name states, it is shared among all the users in the cell as, in general, no resource reservation is performed in

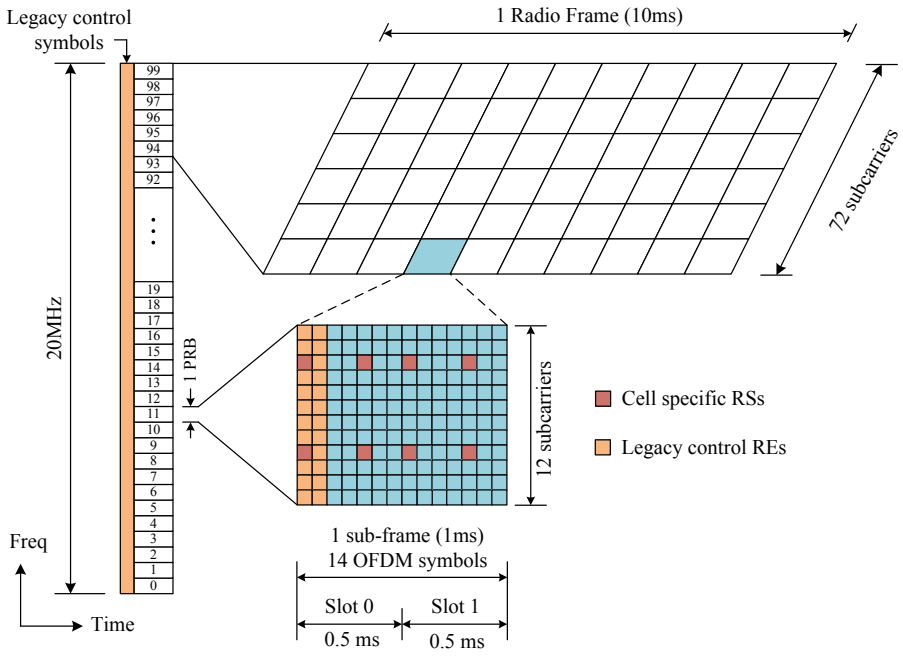

Figure 2.5: Radio frame structure for legacy LTE system for 20MHz bandwidth and Normal CP type.

LTE. Transmission of PDSCH payloads is allowed only in given portion of the spectrum and in certain time interval according to a scheme. An example of the typical structure of the LTE downlink subframe is shown in Fig. 2.5, where it is possible to observe the case of a LTE downlink subframe when 2 OFDM symbols. are dedicated to control messages.

2.6.2 LTE-MTC Framework

In this section, we present the main concepts that have been introduced to LTE-MTC. Since part of the contribution of this thesis is related to the synchronization signals and the physical broadcast channel employed by LTE-MTC, we provide a brief introduction for those topics. In fact, MTC has the main weight of contribution for LTE future releases including Release-13 (R13) that is currently being developed [75][76]. LTE-MTC systems are being improved to support the special requirements including low cost, low data rate, and low power features for M2M communications over LTE [76][77]. This can be realized by employing no spatial or frequency diversity at the UE, low modulation orders, and very long duty cycles to entourage the UE to sleep more. In addition, since MTC UE can suffer from a reachability issue, the

specifications define enhanced coverage UEs that can still decode signals with an SNR of as low as -15dBs. Moreover, frequency hopping is a new added feature to enhance detection within the reduced bandwidth.

Since regular PDCCH crosses the whole system bandwidth, an LTE-MTC UE does not have the capability of demodulating the legacy PDCCH as MTC UE bandwidth is restricted to 1.4MHz. In [71], the authors have presented a new control channel design to support enhanced coverage for LTE-MTC based on the existing Enhanced PDCCH (EPDCCH). The EPDCCH is introduced in LTE-A Release-11 to achieve better spectral efficiency by exploiting frequency selectivity and beamforming and also to provide greater flexibility of dynamic allocation of control channel resources. The main contribution in [71] is to support repetition codes which utilize the conventional time averaging to enhance the control channel performance in LTE-MTC systems. Fortunately, this proposal has been accepted by LTE-MTC group in their recent agreements [78]. However, the agreement indicates well-defined specifications for the new control channel for MTC, namely MTC-PDCCH or MPDCCH, which have not been considered by [71][70]. The new rules take into account the new system structure and the performance targets for various applications.

In frequency-division duplexing mode, traditional LTE signal can be carried over 1.4, 3, 5, 10, 15, or 20MHz of bandwidth. To maintain the current base station (eNodeB in LTE terminology) with minimal changes, the concept of a narrowband (NB) has been introduced to support only 1.4MHz MTC UEs [77][79]. A narrowband is defined as a contiguous set of 6 PRBs or correspondingly 72 sub-carriers used for MTC operation. For example, Fig. 2.6 shows 16 different NBs for the typical 20MHz bandwidth. A normal CP is considered such that a single sub-frame consists of 14 OFDM symbols. Due to the allowed number of PRBs, the MTC UE shall employ 128-point FFT block at the receiver side to synthesize the received time domain samples into the frequency domain sub-carriers. With the small bandwidth offered to MTC UE, there is a significant loss of frequency diversity. To recover portion of this gain, the LTE-MTC system will make use of frequency hopping between narrowbands [77][70]. The MTC UE has to hop from one NB to another after a predefined time period. The hopping sequence shall be known in advance by the UE and it will be a cell specific feature.

Coverage enhancement (CE) is one of the main objectives for LTE-MTC which aims to

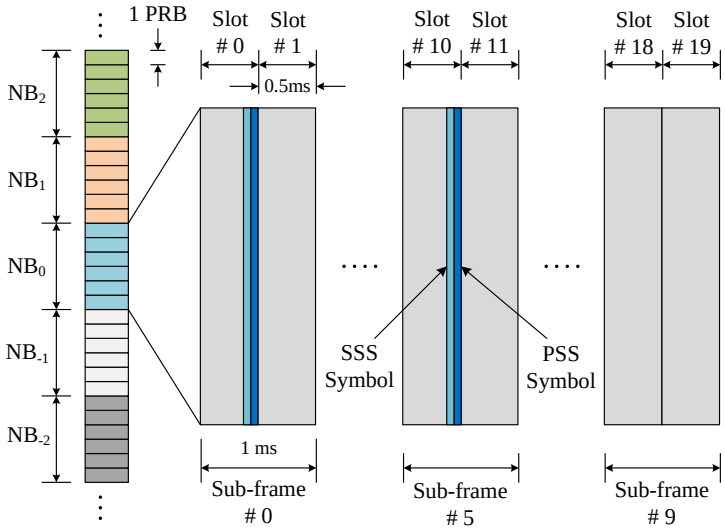

Figure 2.6: Radio frame structure for LTE-MTC systems. The central NB is expanded in time to show the PSS/SSS symbols mapping.

achieve a goal of 15 dB improvement in the link budget when compared to legacy LTE. To realize this objective, two broad categories, namely CE Mode A and CE Mode B, are defined [78]. Typically, CE Mode A describes a set of behaviours for no CE or small CE while CE Mode B is defined for UEs with medium and large CE. The CE mode is signalled to the UE when the connection is established to the network. Initially, the UE shall estimate its CE level based on its own power measurements.

2.6.2.1 Cell Specific Synchronization Signals

PSS and SSS sequences are two synchronization signals that introduce 504 distinct cell IDs [80]. The cell IDs are grouped into 168 cell ID groups, and each group contains three IDs for distinct sectors in a cell. A physical layer cell identity $N_{ID}^{cell} = 3N_{ID}^{1} + N_{ID}^{2}$ is thus uniquely defined by a number N_{ID}^{1} in the range of 0 to 167, representing the cell ID group, and a number N_{ID}^{2} in the range of 0 to 2, representing the sector ID within the group.

The PSS is constructed from a frequency domain Zadoff-Chu sequence of length 63 [81]. The ZC sequence satisfies the constant amplitude zero autocorrelation property which limits the PAPR and provides ideal cyclic autocorrelation. Three PSS sequences are employed in LTE, corresponding to the three sector IDs. The SSS sequence is a second synchronization

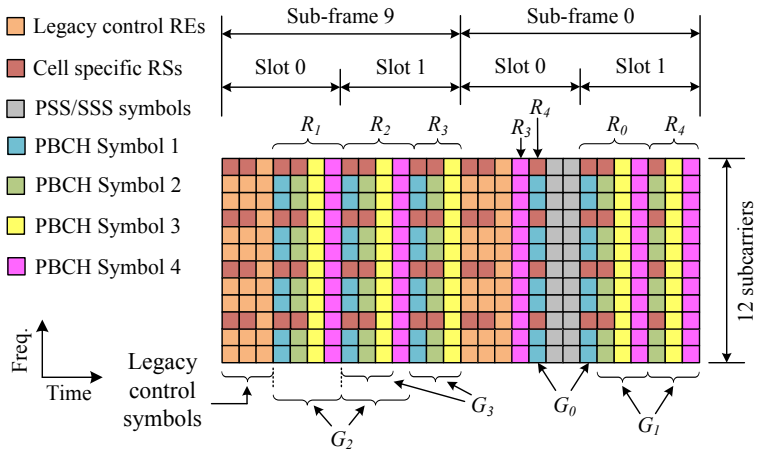

Figure 2.7: One PRB showing the MPBCH repetition for FDD Normal CP mode.

signal and is constructed as an interleaved concatenation of two binary m-sequences, each of length 31. The combination of these two sequences differs between sub-frames 0 and 5. The concatenated sequence is scrambled with a scrambling sequence given by the primary synchronization signal.

2.6.2.2 Broadcast Channel in LTE-MTC Systems

To support coverage enhancement, repetition is introduced for the PBCH [82]. Fig. 2.7 shows how that repetition is structured for FDD with Normal CP. There are five repetitions in total that are spread across sub-frame 9 and the following sub-frame 0. The legacy PBCH is shown as R_0 (repetition 0). Three OFDM symbols are left for the legacy downlink control channels. Fig. 2.8 shows the downlink transmitter chain for the LTE-MTC broadcast channel. The MIB payload is first generated, encoded, interleaved and then rate matched to fit the amount of resources used for the legacy broadcast channel transmission. The Rate Matching (RM) output is scrambled and QPSK modulated. The Resource Elements (REs) are mapped to the proper broadcast channel elements on the central narrowband. According to LTE-MTC agreements [78], the PBCH symbols are repeated as discussed above. The time domain symbols are synthesized using Inverse Fast Fourier Transform (IFFT) after which the CP is inserted.

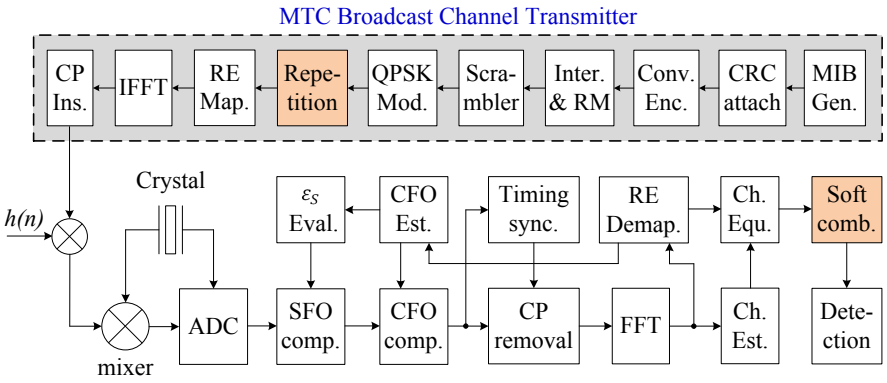

Figure 2.8: Transmitter/receiver model for the PBCH in LTE-MTC system

2.6.3 LTE NB-IoT Framework

Since the core IoT devices or massive MTC devices typically send small amounts of data and require extended coverage, a special category, namely NB-IoT, has been incorporated to LTE specifications to support IoT features [83]. The design targets for this special category require reduced complexity, promote battery longevity, and enhanced coverage. Furthermore, the need to support high data rates seldom applies to massive MTC. The link budget of NB-IoT has a 20dB improvement over conventional LTE-A [84]. These requirements have been realized by utilizing a single receive antenna system, supporting only QPSK modulation in the downlink side, and employing extended discontinuous reception cycles to reduce the power consumption in deep sleep modes. Moreover, signal repetition is considered as the key factor to provide performance gain [85].

NB-IoT intends to occupy a narrow bandwidth of only 200KHz, which is not backward compatible to the supported bandwidths by the legacy LTE. Therefore, NB-IoT redefines the cell attach procedure including cell search and initial synchronization [86]. During initial synchronization, CFO is estimated and compensated to enable proper signal detection. The UE acquires the physical cell identification by employing the cell search procedure. To cope with these changes, NB-IoT employs new set of synchronization signals, namely Narrowband Primary Synchronization Signal (NPSS) and Narrowband Secondary Synchronization Signal (NSSS) [84]. The new sequences have different bandwidth, mapping, periodicity, and generation when compared to the legacy LTE synchronization signals. Unlike conventional

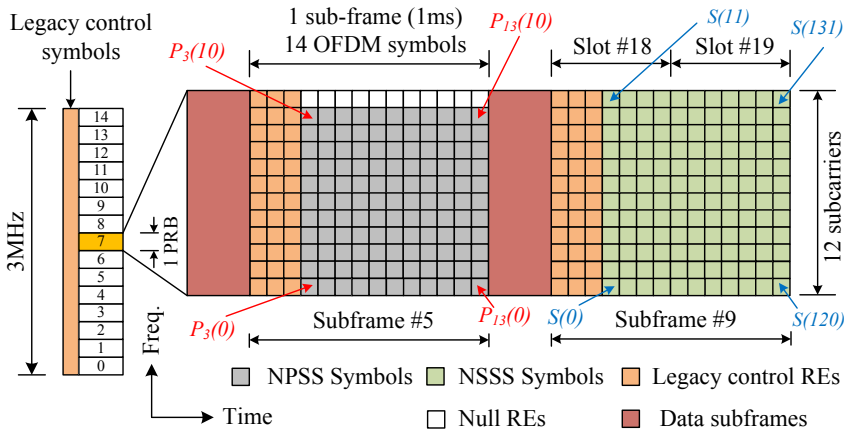

Figure 2.9: Radio frame structure for NB-IoT systems. The allocated RB is expanded in time to show the NPSS/NSSS symbols mapping.

LTE, cell ID is encapsulated only in the secondary sequence without involving the primary sequence.

With a carrier bandwidth of just 200KHz, an NB-IoT carrier can be deployed within an LTE carrier, the LTE guard band, or as a standalone system. Fig. 2.9 shows a 3MHz LTE carrier in which a single PRB is assigned to NB-IoT. An operating NB-IoT band is defined as a contiguous set of 12 sub-carriers forming one PRB. A single radio frame is 10ms which consists of 10 sub-frames with equal duration. Each sub-frame is divided into two slots with equal periods. Unlike conventional LTE which defines two CP types with different CP patterns, NB-IoT in Release-13 supports only the normal CP type, where a slot is composed of 7 OFDM symbols. According to the specification [84], if the signal is sampled at 1.92MSamples/sec, similar to LTE-MTC, the CP length of the first symbol in each slot is 10 samples and those of the other symbols are 9 samples long. Also, in this case, the OFDM symbol spans $N = 128$ sub-carriers. Since NB-IoT devices tend to be placed in signal-challenged locations, the standard defines enhanced coverage UEs to decode signals at very low SNRs of about -12.6dBs.

Unlike legacy LTE-A, NPSS and NSSS sequences are constructed from a frequency domain Zadoff-Chu sequence where NPSS length is 11 samples while the NSSS consists of 132 samples. The NPSS, $P_l(n)$, is generated such that $P_l(k) = Q(l)e^{-j\pi uk(k+1)/11}$, where $0 \leq k < 11$, $3 \leq l < 14$ is the OFDM symbol index, the sequence root $u = 5$, and $Q(l)$ is a modulation

sequence given by $\{1, 1, 1, 1, -1, -1, 1, 1, 1, -1, 1\}$, respectively. In NB-IoT system, there are still 504 unique physical cell IDs. However, all of them are only indicated by the NSSS. The NSSS, $S(k)$, is generated according to,

$$S(k) = \bar{C}_q(k')\, e^{-j2\pi\theta_f k}\, e^{-j\frac{\pi u k(k+1)}{131}}, \quad 0 \leq k < 132 \tag{2.8}$$

where $k' = k \bmod 128$, the root sequence, u, is related to the cell ID, N_{ID}^{Ncell}, by $u = (N_{ID}^{Ncell} \bmod 126) + 3$, and the cyclic shift, θ_f, is related to the radio frame index, n_f, such that $\theta_f = \frac{31}{132}(n_f/2) \bmod 4$. The modulated sequence, $\bar{C}_q(k')$, is given by $\bar{C}_q(k') = 2C_q(k') - 1$, where q is a cell specific parameter that is given by $q = \lfloor N_{ID}^{Ncell}/126 \rfloor$ and C_q forms four complementary 128-bits binary sequences.

In conventional LTE, primary and secondary synchronization signals (i.e., PSS and SSS, respectively) are mapped to two consecutive OFDM symbols in the same slot with a periodicity of 5msec. However, NPSS is mapped to subframe 5 of every radio frame. NSSS is mapped to the last 11 ODFM symbols of subframe 9 in radio frames having $n_f \bmod 2 = 0$. Sequences are mapped to frequency sub-carriers in an increasing order, then applied across time as shown in Fig. 2.9.

2.7 Conclusion

In this chapter, we have presented a general background about the interweave cognitive radio network model and the next generation cellular M2M communications based on OFDM systems. It is clear that the next generation Internet would serve numerous number of objects and hence the spectrum scarcity would be a real challenge. On the other hand, cognitive radio network models can solve the underutilization problem of the frequency spectrum. Motivated by these facts, in the following Chapter, we present the framework to employ the interweave cognitive radio network model in order to address the spectrum scarcity problem for the M2M communications. In addition, we discuss the challenges of providing low power and low cost devices for next generation cellular networks.

In Chapter 4, we address one of the issues in nowadays interweave CR networks, namely the throughput reduction of the cognitive network due to the spectrum monitoring in the

presence of the quiet periods. In this regard, we introduce an OFDM based spectrum monitoring algorithm that allows the coexistence of the continuous reception while the spectrum is monitored. The technique does not only allow a high throughput cognitive network, but it shows a reliable and efficient spectrum monitoring in real environment with real impairments. As a second challenge of interest, the power consumption for the Nyquist-based wideband spectrum sensing is considered in Chapter 5. To operate at ultra low power consumption, a one-bit quantization process can be employed to significantly reduce the analogue to digital conversion power consumption. This process can be efficient only if the proper system architecture is utilized.

For this reason, two separate architectures are presented, in Chapter 5, to enable the one-bit quantization approach. The first technique uses a feedback from the RF processing about the total observed power along with the PSD estimation from FFT-based wideband sensing. By defining the proper threshold, the performance of the FFT-based one-bit quantizer system is quantified at a reduced complexity and power consumption. A second architecture for the one-bit quantizer that relies on the window-based autocorrelation is also presented. In this technique, we prove that the statistical autocorrelation for the quantized system fully reflects the spectrum occupancy of the wideband system. Therefore, the estimated PSD can be utilized to discriminate between occupied sub-bands and spectrum holes. A sub-optimal detection algorithm is designed and simulated. Complexity and power consumption are analysed for this technique as well.

In Chapter 6, we consider some of the challenges attached with the new cellular M2M communications. For example, the cell search and initial synchronization for the LTE-MTC system are quantified. Time averaging can help in enhancing the performance of the conventional algorithms subject to he new system requirements. In addition, we present a frequency tracking approach for the LTE-MTC systems based on the repetition nature of the broadcast channel. Last, we address the new challenge of cell search and initial synchronization in NB-IoT LTE-based system.

Chapter 3

Cognitive Radio and Next Generation M2M Cellular Networks

3.1 Introduction

The ultimate objective of M2M communications is to construct comprehensive connections among all machines distributed over an extensive coverage area. Recent reports show that the projected number of connected machines/devices to the IoT will reach approximately 50 billions by 2020. For instance, the rapid growth of the number of connected devices to the Internet has been reported by Cisco [87] as shown in Fig 3.1. This massive introduction of communicating machines has to be planned for and accommodated with applications requiring wide range of requirements and characteristics such as mobility support, reliability, coverage, required data rate, power consumption, hardware complexity, and device cost. Other planning and design issues for M2M communications include the future network architecture, the massive growth in the number of users, and the various device requirements that enable the concept of IoT.

In terms of M2M, the future network has to provide machine requirements as power and cost are critical aspects of M2M devices. For instance, a set-and-forget type of application in M2M devices such as smart meters require very long battery life where the device has to operate in an ultra low-power mode. Moreover, the future network should allow for low complex and low data rate communication technologies which provide low cost devices that encourage the large scale of the IoT. The network architecture, therefore, needs to be flexible enough to provide these requirements and more. In this regard, a considerable amount of research

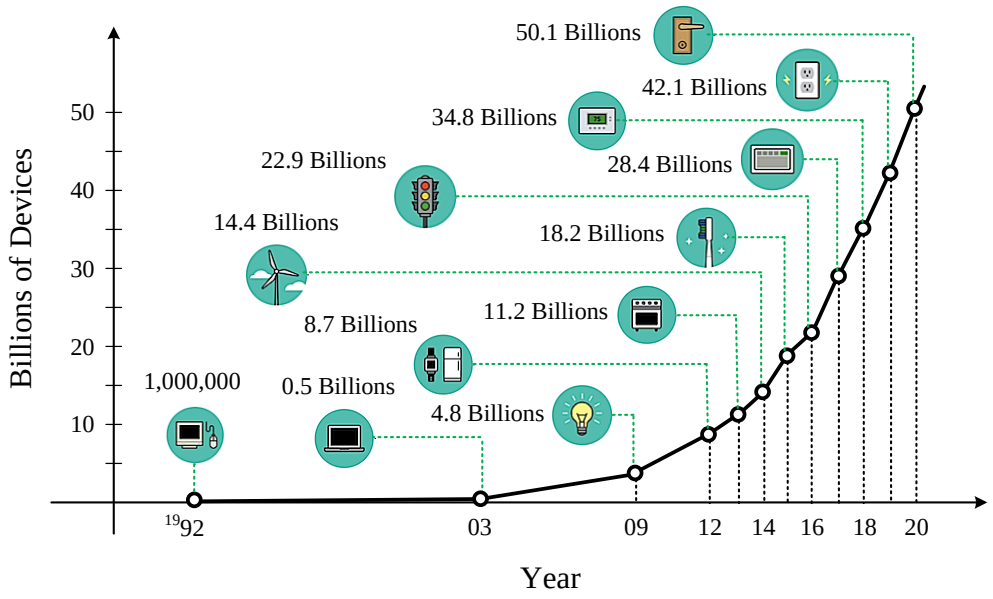

Figure 3.1: Expected number of connected devices to the Internet. This chart is obtained from recent reports developed by both Cisco and Ericsson.

has been directed towards available network technologies such as Zigbee (IEEE 802.15.4) or WiFi (IEEE 802.11b) by interconnecting devices in a form of large heterogeneous network [88]. Furthermore, solutions for the heterogeneous network architecture (connections, routing, congestion control, energy-efficient transmission, etc.) have been presented to suit the new requirements of M2M communications. However, it is still not clear whether these sophisticated solutions can be applied to M2M communications due to constraints on the hardware complexity.

In this chapter, we address the issues that facilitate the existence of cellular MTC including the network architecture, the spectrum scarcity problem, and the device requirements. We review different approaches, including small cell design and interconnecting the cellular network to other wireless networks, based on research efforts and industrial technologies to tackle these issues. Also, we propose a scenario in which cognitive radio can be employed to solve the spectrum scarcity problem that would become significant with this increase in the number of connected devices. Furthermore, we provide a comparison of the potential solutions and the challenges and open issues that require future work to allow for practical development of each solution. Based on these challenges, the following chapters in this thesis

consider solutions to some issues related to cognitive radio network deployment and to enable the implementation of the next generation cellular M2M systems.

3.2 MTC Development

Current M2M markets are highly fragmented and most vertical M2M solutions have been designed independently and separately for each application, which inevitably impacts large-scale M2M deployment [89]. However, when it comes to standardizations, the global coverage, the cellular network stability and maturity, together with the speed offered by recent cellular networks (LTE rates up to 150 Mbps for mobile objects), render wireless cellular technologies as the best candidate for the implementation of secure and reliable business critical M2M services. Several working groups in radio-access-networks (RAN) contribute very actively to the work on MTC-related optimization for 3GPP LTE networks. From day one, the support for MTC was one of the major concerns for the 3GPP and the development for a robust MTC design was divided across different releases [90]. Fig. 3.2 shows the development steps and features for MTC in different releases. Since LTE has the ability to support high performance, high throughput devices, the objective was to develop high volume, low cost, low complexity, and low throughput user-equipment LTE-based MTC devices.

It is worth to mention that seven of the worlds leading standards bodies, including for example the European Telecommunications Standards Institute (ETSI) and the Association of Radio Industries and Businesses (ARIB), have come together to create oneM2M. The main objective of oneM2M is to minimize M2M service layer standards market fragmentation by consolidating currently isolated M2M service layer standards activities and jointly developing global specifications. Although this solution considers some test cases for predefined devices such as smart metering, smart grids, eHealth, and automotive applications, not much attention has been taken on the underlying connectivity layer since oneM2M leverages on current and future technologies such as LTE networks. From the history of MTC/LTE development, the first generation of a complete feature MTC device has emerged in R12. In this release, the 3GPP committee has defined a new profile referred to as category 0 or CAT-0 for low-cost MTC operation. Also a full coverage improvement is guaranteed for all LTE duplex modes.

On the other hand, R13 is a future release for LTE-A in which MTC has the main weight of contribution. Its main goal is to further enhance the MTC LTE-based UE beyond R12. The main objectives for the MTC improvements are, (a) Supporting ultra low-power, low-cost, and narrow-band UE, (b) Enhancing the monitoring of service quality, and (c) Cooperation with other service delivery platforms represented in only the oneM2M [91].

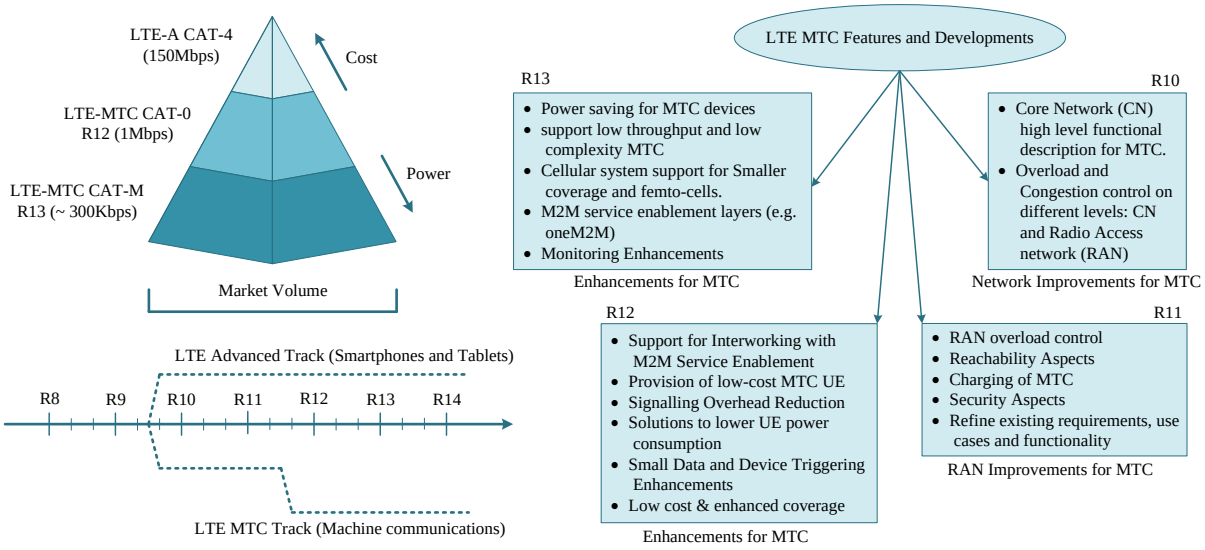

Figure 3.2: MTC in 3GPP LTE Networks: Releases and Features.

3.3 Small Cell Versus Heterogeneous Network Model

The next generation cellular MTC network has to efficiently interconnect several billions of wireless machines to support IoT. The traditional method to support these devices is to employ a well-designed M2M technology over a small cell structured system. In this case, cellular network providers need to deploy several thousands of eNodeBs, each with a smaller cell radius rather than full-power transmitters with large cells. Of course, this solution is cost-inefficient. Moreover, with such large number of small cells, co-channel interference is a limiting factor and complex designs are needed to maintain the required QoS. Another major drawback of this approach is the significant traffic increase due to signalling congestion and network management burden.

Although the "heterogeneous network" model is not currently recommended for MTC due to the limited capabilities of the machines, research efforts [92] have been invested to support

the idea of utilizing the cellular network itself as a small type of a heterogeneous network. The concept is that, in many applications, machines can be clustered geographically where the members of each cluster can be interconnected together through certain technology. To reduce the number of machines connected to the cellular network, each cluster would select a representative, a cluster head, to connect with the cellular network. Inside the cluster, the cellular network is transparent to all machines and only the cluster head will be responsible for relaying the aggregate traffic of the entire cluster. For example, if all machines have WiFi interfaces, then WiFi technology can be utilized to interconnect cluster members. In that sense, the cluster head will be communicating over its WiFi interface inside the cluster while using the LTE interface, for example, to connect to the cellular network as shown in Fig. 3.3. In this model, the cellular network has offloaded part of its traffic to the individual clusters and therefore, reduces the effective number of covered users. The main benefit of this approach is the relaxation on congestion that would result if no clusters are formed.

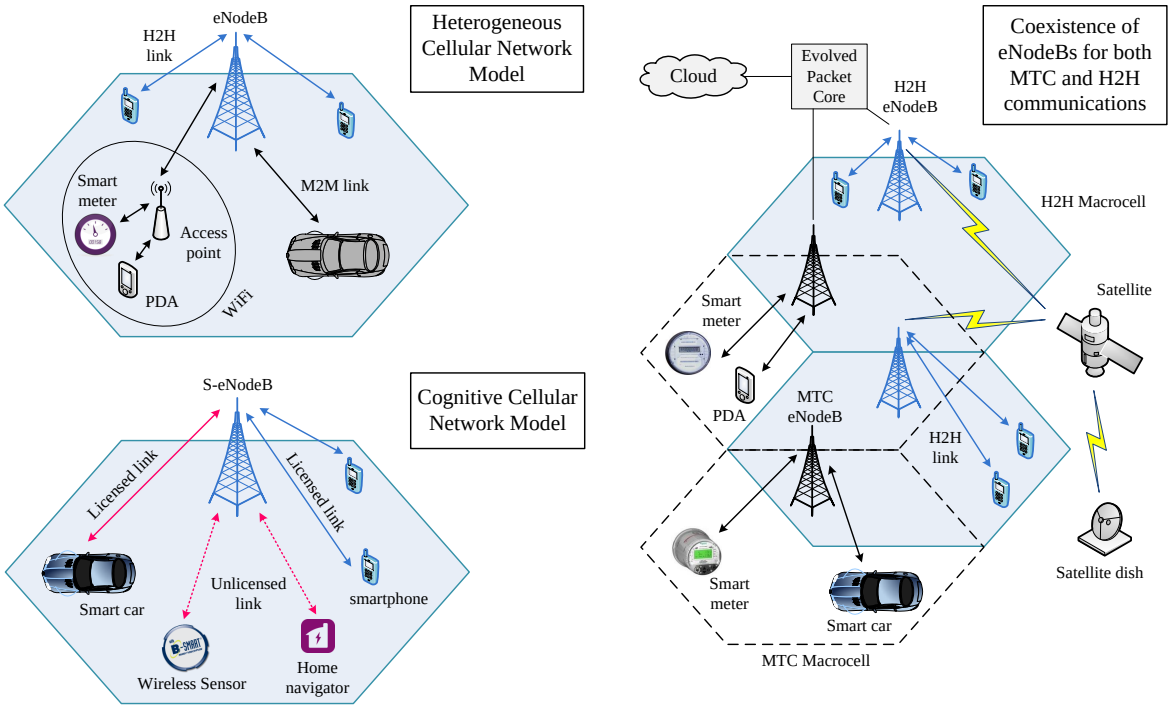

Figure 3.3: Various network models to interconnect numerous number of machines to IoT.

3.4 Cognitive Cellular M2M Networks

The idea of cognitive radios was originally proposed to offer more efficient utilization for the RF spectrum [93]. In this context, there are two approaches to apply the CR concept in cellular M2M networks. The first approach [94] assumes that there can be two types of eNodeB stations, one for typical UEs and other for MTC UEs coexisting with each other (Fig. 3.3), to relax signalling congestion and management burden. In this case, M2M devices seek to opportunistically use the spectrum when the H2H devices are idle. Therefore, M2M and H2H devices are not allowed to simultaneously operate over H2H links. This can be done through coordination between the corresponding eNodeB stations. Once a radio resource is occupied by M2M communications, this radio resource is regarded as suffering from server interference and will not be utilized by H2H communication. Even though this approach is simple to apply, it can degrade the QoS of H2H applications especially when the number of MTC devices is very large.

To overcome the aforementioned problems, we propose a second approach which supports unlicensed bands in addition to existing licensed bands. Here, it is assumed that the network will sense unlicensed bands to find extra vacant bands. If complexity permits, more than one unlicensed band per cell can be utilized by a Smart-eNodeB (S-eNodeB), a coined term to differentiate between the traditional eNodeB and the proposed one, to further increase the number of devices (Fig. 3.3). Indeed, this solution leverages on the huge amount of free spectrum available around the 5GHz and the TV white space. However, current radio access standards such as IEEE 802.22 and IEEE 802.11af already allow the use of this free unlicensed spectrum. Therefore, spectrum sensing and monitoring is a must. This can be implemented by introducing a new layer for spectrum management to support cognition over the unlicensed bands. That is, the S-eNodeB should be capable of (a) sensing the spectrum, (b) gathering information about the available suitable bands, (c) taking decisions on the conditions of these bands, (d) informing the neighboring S-eNodeB's about the allocated unlicensed band, (e) monitoring the allocated unlicensed band, and (f) always providing an alternative band.

If the S-eNodeB handles multiple unlicensed bands, then it should classify the machines

based on their performance tolerance so that a machine is switched to the proper unlicensed band that meets its requirement. Of course, this assumes that the machine would have a group ID to declare its needs which in turn has to be shared with the S-eNodeB during call setup. To clarify how machines and S-eNodeB can work in this scenario, a detailed call procedure is demonstrated to show how a machine can access the unlicensed band. Once the machine is switched on, it goes to the calibration process in which the RF front-end adjusts or even estimates the IQ mismatch parameters. The following procedure is shown in Fig. 3.4 and is discussed below.

- The machine would start the usual frequency scanning over the licensed LTE carriers. Once it locates a strong serving cell, a synchronization procedure is followed so that the machine is locked to the base station. It further decodes the master information block to recognize the cell specification.

- The machine sends a random access request to connect to the cell. The Smart eNodeB then requests the group ID which will be sent over the uplink control channel.

- The S-eNodeB will request the machine to switch to another carrier in the unlicensed band. Full information about the carrier such as modulation, coding, and relative timing to the licensed carrier are also sent to the machine. Afterwards, the S-eNodeB assumes that the session is complete and the machine has been configured.

- The machine will then switch its RF to the desired carrier and enter the synchronization mode to lock itself to the S-eNodeB at the unlicensed carrier.

- The machine defines itself one more time by sending a random access request over this carrier. If it is permitted, the machine can exchange data with the S-eNodeB over the physical uplink and downlink shared channels.

- The S-eNodeB can interrupt the machine by scheduling a measurement gap in which the machine measures and reports the power of a certain carrier in the unlicensed or licensed bands.

- The unlicensed carrier can be dynamically changed based on the collected measurements at the S-eNodeB. In this case, machines have to be informed about the new carrier and its settings.

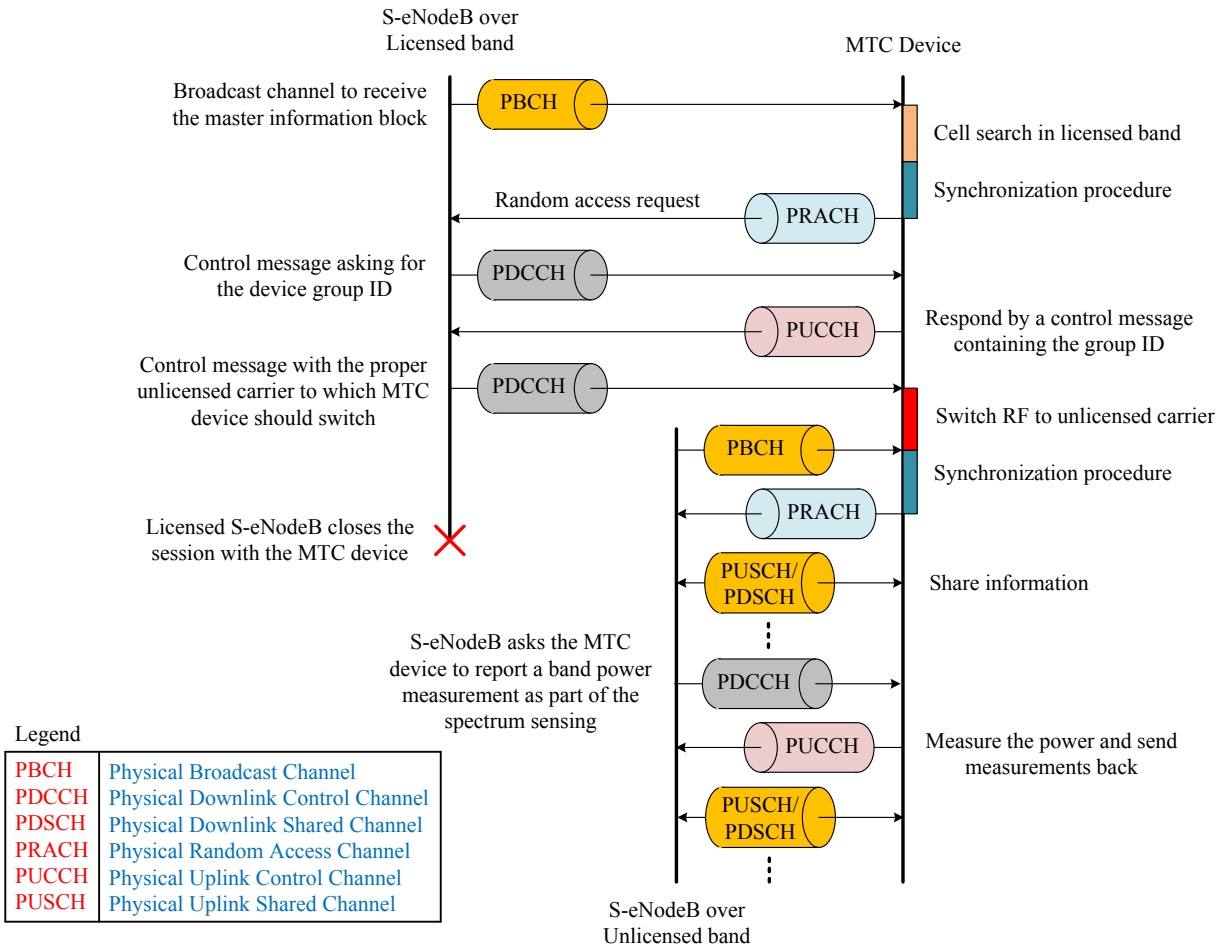

Figure 3.4: Handshake messaging for MTC device over cognitive cellular network.

3.5 Ultra Low-Power and Low-Cost Networks

To save battery life, low-power design is always desired for wireless communication systems. However, power reduction is not an easy task as it is related to the system reliability, rate of data exchange, and the radio chip design and implementation constraints. When the communication link is unreliable, higher layers translate this into retransmissions which results in longer active times and hence, high power consumption. Similarly, if the system continuously

exchange data then it will consume more power. Based on a case study for ZigBee [89], it is shown that if the radio is switched-on all the time, it will deplete a typical AA battery within a week. However, turning the radio duty cycle to 25% extends the lifetime to about a month. Turning it further down to 1% yields years of lifetime. Therefore, low power can be achieved through a reliable communication link with small duty cycle. In LTE-advanced, the concept of discontinuous reception (DRX) cycles is applied where the eNodeB schedules a silent period (DRX cycle) to encourage the device to switch-off the radio chip so that low duty cycle is achieved. To support ultra low-power design in recent releases, a long DRX cycle mode has been employed (with a maximum period of 2.56sec in R12) to further reduce the duty cycle.

Another important aspect of future MTC devices is their low-cost design which is typically provisioned by reducing the complexity of the system while providing the same coverage. The communication system architecture usually involves a general processor to run the software, a memory to hold both instructions and data, and a physical-layer modem to handle the communication protocol. As expected, most of the complexity reduction comes from the physical-layer modem features along with a small portion of data memory reduction. Therefore, a low-cost design is typically related to a feature reduction while the coverage is carefully kept unchanged. For specific applications, low data rates and/or low latency are acceptable. In this case, the modem features can be relaxed to target low-cost design. In recent LTE releases, special category has been defined to support MTC for low data rates which leads to complexity reduction. In LTE-R12, this category supports only one receive antenna and a maximum data rate of 1Mbps. However, those features will be further reduced in LTE-R13 with the expected maximum data rate being 300Kbps (for Narrowband IoT).

3.6 Challenges, Open Issues, and Future Directions

3.6.1 Heterogeneous Networks

When a number of machines is able to form clusters, the cellular network becomes lightly loaded. This conclusion has been investigated by many researchers and even practically

demonstrated on WiFi as the internal technology inside the cluster. However, it is hard to judge if the machines can really form clustering or not. In fact, clusters are formed only if the WiFi connectivity between cluster members is acceptable (data rates are higher than the LTE load generated in the cluster). Also, clustering allows machines to enjoy seamless connectivity to the cellular system while spending more time on a secondary, WiFi-based interface, which is less power consuming than LTE. On the other hand, shifting the responsibility of the aggregate traffic from all cluster members to the cluster head can be challenging especially if the link from the cluster head to the eNodeB is poor. Since the architecture assumes a centralized control at the head node, it is expected that the full cluster will fail. Therefore, more research effort is required to investigate the possibility of dynamically selecting the head node based on the channel quality with the cellular system. One challenge with this solution is to select the optimum period after which a rescheduling has to be done.

3.6.2 Cognitive Radio Network

As discussed earlier, spectrum sensing and monitoring are essential to utilize the cognitive radio concept in which some of the machines operate over an unlicensed band. However, there are many challenges to address this problem.

- *Spectrum sensing techniques*: The sensing can be either centralized at the S-eNodeB or done in cooperation with the machines. Better performance is expected from the latter case since more spatial diversity is utilized. Generally, cooperation is achieved by sending either local decisions [95], which can be either hard or soft decision, or by sending the useful portion of the received data set. Processing power of the machines limits the first approach while high traffic over the control channel is the main challenge for the second approach [96]. Moreover, the link between the machine and the S-eNodeB is not ideal and the sensing decisions/data can be received incorrectly which may alter the sensing accuracy at the S-eNodeB.

- *Wideband sensing methodology*: During the initial sensing stage, a wideband (around 1GHz) has to be assessed to locate a suitable vacant band [30]. This can be implemented by scanning different bands one after another and measuring the in-band power. This

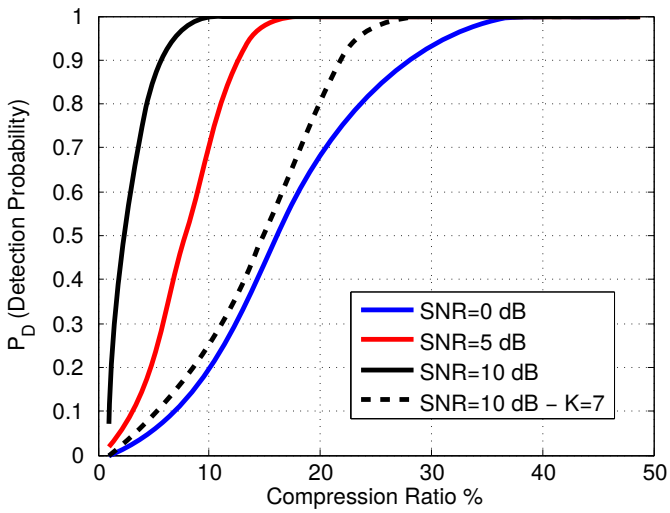

Figure 3.5: Effect of compression ratio (i.e., ratio of the non-uniform sampling rate to the conventional Nyquist rate) on the detection performance when the false alarm rate is 1%. 16 contiguous non-overlapped bands are investigated where each has a bandwidth of 1MHz. Only four active bands are considered, therefore the sparsity level $K = 4$.

technique is simple but it requires time and power to find a suitable band. Another alternative is to examine the power spectral density of the entire wideband at once. Since *this method requires high speed analogue-to-digital conversion which is power consuming*, compressive sensing (CS) [95] is a promising technique to obtain the power spectral density of the wideband spectrum while sampling at rates lower than the Nyquist rate. The concept is to capture few measurements of the *sparse* spectrum. The wideband spectrum is related to those raw measurements by a linear under-determined system of equations. Optimization techniques can be employed to solve this set of equations in order to find the best solution that satisfies the original assumption for the spectrum which is being *sparse*. Fig. 3.5 shows the detection performance as a function of the ratio of non-uniform sampling frequency to the typical Nyquist rate. It is clear that CS is able to detect the spectrum occupancy by a ratio of 1/10 of the Nyquist rate at high SNR. Although CS is very promising in this context, many challenges exist due to the current algorithmic complexity as well as the basic assumptions. For example, the spectrum is dynamically loaded and the *sparse* assumption may not be valid which

results in performance degradation ($K = 4, 7$ cases in Fig. 3.5). Cooperation may be utilized to enhance the accuracy, however finding a high-performance low-complex/low-data rate cooperative sensing technique is not a trivial task. In that direction, more research efforts are needed to develop efficient algorithms to render CS possible with reasonable complexity, especially for MTC where complexity is a real challenge.

- *Narrowband sensing techniques*: A signal processing algorithm is needed to decide on the activities within each of the wideband slices [5]. Conventional detectors [97] include the energy detector, the cyclostationary detector, and the matched-filter detector. In all cases, a decision statistic is computed and compared to a threshold to decide whether a specific band is occupied or not. Complexity, performance, and prior information about the signal to be detected are the main metrics to judge the quality of the detector. Among those detectors, the energy detector is known to be the only simple non-coherent detector. From performance perspective, the matched-filter is known to be the optimal detector. However, it requires full knowledge of the detected signal.

  The Cyclostationary detector can be used only if the signal possesses the cyclostationarity property where its statistics, mean and autocorrelation, are periodic with some known period. Therefore, it requires partial information about the detected signal which is typically the period of cyclostationarity. Fig. 3.6 shows the probability of miss-detection for various narrowband sensing techniques against SNR. Effects of timing errors, noise uncertainty, and hard decision cooperative sensing have been included. The performance results show that: (a) Any uncertainty of the noise level will significantly alter the performance of the energy detector, (b) Matched-filter detection is very sensitive to timing errors, and (c) Cooperation involves high diversity gain. However, these results assume an ideal channel (no noise and no fading) between the machines and the S-eNodeB. The conclusion is that, improvements and/or new sensing techniques are needed to provide less-complex, non-coherent, and robust practical algorithms. *One of the significant drawbacks of the current narrowband sensing is that it requires a quiet period which causes sever reduction in the cognitive radio network throughput.*

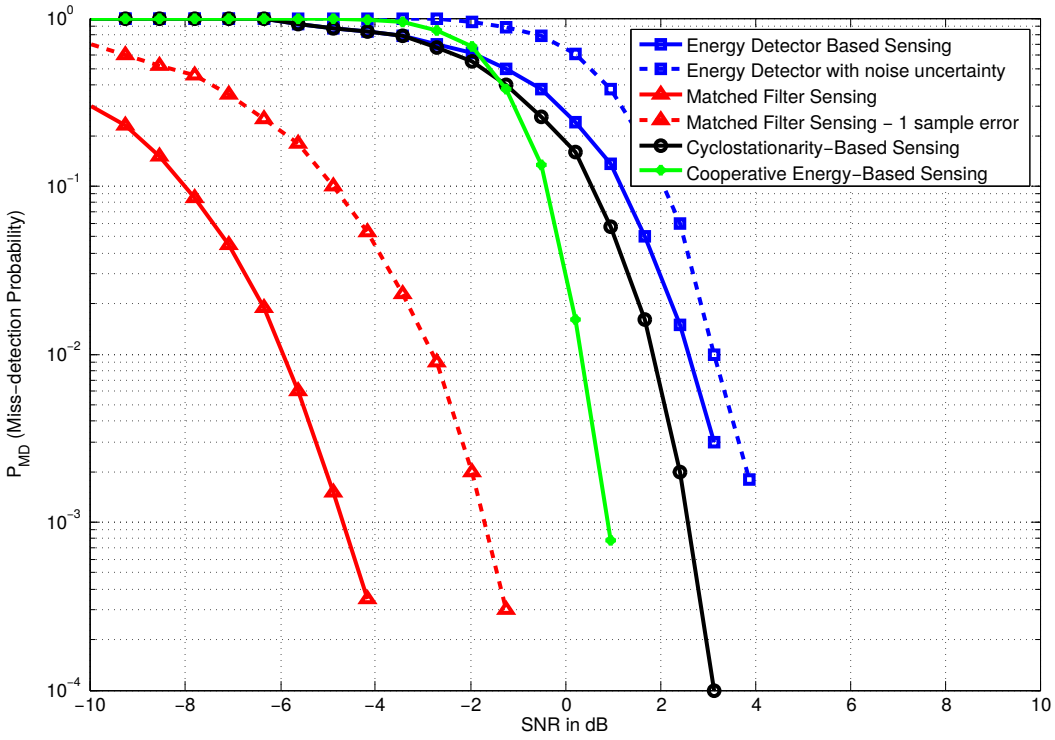

Figure 3.6: These curves are plotted for a false alarm rate of 1%. The window size for the energy detector is the same as the matched filter length. Both agree with the cyclostationary detector period which is 32 samples. For the cooperative sensing, hard decision is used with K-out-of-N rule where K=5 users and N=10 users. The noise uncertainty error is ±0.5 dBs for the energy detection case.

3.6.3 Low-Power Low-Cost Networks

Although longer DRX cycle significantly reduces the power, it also introduces some challenges to the system design. Since the radio chip will be off during the DRX cycle, the device/UE has no way to synchronize itself to the eNodeB. Therefore, the typical behaviour for the device/UE would be to wake-up as early as required to quickly resynchronize itself to the eNodeB before receiving further packets. One of the issues is to determine the best wake-up time so that the synchronization performance is met and no additional power is lost. Another issue is related to the cooperative sensing architecture, if applicable, where the device/UE will not be able to sense or monitor any band while it is in a deep sleep mode. The band can suffer from high interference levels caused by other networks that attempt to access the

same band. Finally, the power can be minimized by properly designing power domains in the hardware to decide which module is not needed to be switched-off.

A low-cost design always comes at the account of system performance with less features provided. For instance, reducing the number of receive antennas from two to one would reduce the spatial diversity of the modem. Therefore, advanced signal processing algorithms for synchronization, cell detection, and decoding will need to be revised to guarantee the same performance with less diversity gain. Indeed, reducing the cost is not only related to the required features from the network, but it also depends on the hardware design process and underlaying technology. For example, optimizing the internal word sizes of the various hardware modules inside the modem will result in a low gate count and low power consumption. However, the optimization algorithms that can achieve this are not unique as signal statistics across various modules are system dependent.

3.7 Conclusion

In this chapter, we considered the next generation cellular M2M communications challenges. With the rapid growth of the number of connected machines, the spectrum occupancy has to be extremely utilized. Thus, conventional solutions such as small cell planning and heterogeneous network architecture seem to be cost inefficient. We presented the idea of utilizing the cognitive radio to overlay less important connections to the cognitive band. In this direction, we presented the concept of smart eNodeB with an expected call setup while the current available physical LTE channels can be used. Heterogeneous network concept is discussed to address the same problem and its challenges are discussed. Future standards are encouraged to provide both options (i.e. the cognition concept and the heterogeneous network model). Finally, a design of low-power low-cost machine is discussed. However, there are important design challenges to make it possible.

Chapter 4

Energy Ratio Algorithm For Spectrum Monitoring

4.1 Introduction

For interweave networks, prior to communication, secondary user must sense the spectrum to detect whether it is available or not. Moreover, during communication, it must be able to detect very weak signals from the primary user in order to quickly vacate the occupied spectrum. Thus, primary user detection is essential to release the spectrum. The CR system may spend a lot of time on this detection. Since the CR users do not access the spectrum during the detection time, this period is called the quiet period [32].

In IEEE 802.22 system, the quiet period consists of a series of consecutive spectrum sensing using energy detections followed by feature detection [98]. Since the energy detection checks only the energy level of the channel, it requires relatively short time but cannot identify the source of energy among primary users and noise. If the CR system detects the energy level higher than the predefined value, that is, it is alarmed by the energy detection, the system performs the feature detection that is able to discern the source of signal by finding the unique feature of each signal but the feature detection spends long time when compared to energy detection [99].

In fact, if the CRs must stop communicating in order to detect the emergence of the primary signal, there will be a trade-off between the performance of the secondary network and the performance of the primary network. During sensing intervals (i.e: the time intervals during which the secondary transmitters are silent while the frequency band is examined),

the secondary network achieves no throughput. If the frequency or duration of the sensing intervals is too large, then the secondary network's average throughput is low and its average delay is high. Between consecutive sensing intervals, traditional spectrum sensing provides no information about the status of the frequency band. Thus, if the frequency or duration of the sensing intervals is too small, then the interference to the primary users are excessive.

Rather than be caught in this trade-off, we can search for a method by which CRs can monitor the frequency band without interrupting their communications. Such methods can detect the reappearance of the primary user during the secondary user transmission. This may supplement traditional spectrum sensing and provide enhanced communications efficiency. If spectrum monitoring determines correctly that there is no primary signal in the band, then the time that would have been spent performing spectrum sensing is used to deliver packets in the secondary network. If spectrum monitoring detects a primary signal in the band during a time period in which spectrum sensing would not have been scheduled, then the disruption to the primary user can be terminated more quickly. Thus the spectrum efficiency of the secondary network is improved and the impact of secondary communications on the primary user is lessened. We are examining two different approaches for the spectrum monitoring done by the CR receiver during reception. These techniques are not replacements for traditional spectrum sensing. Instead, they are supplemental techniques that reduce the frequency with which spectrum sensing must be performed and decrease the elapsed time between the start of a primary transmission and its detection by the secondary network.

The last approach is followed by [100] where the spectrum is monitored by the CR receiver during reception and without any quiet periods. The idea is to compare the bit error count, that is produced by a strong channel code like Low Density Parity Check (LDPC) codes, for each received packet by a threshold. If the number of detected errors is above certain value, the monitoring algorithm reports the primary user activity. The threshold is obtained by considering the hypothesis test between the receiver statistics when the primary signal is absent and the receiver statistics for the desired Secondary-to-Primary power Ratio (SPR).

Although this technique is simple and adds almost no complexity to the system, the receiver statistics are subject to change by varying the system settings. In real systems, there are many parameters that can disturb the receiver error count such as RF impairments

including PN and CFO, SFO, and NBI. The error count will depend not only on the presence of a primary signal but it will also depend on the parameters for those impairments. The receiver statistics may change from one receiver to the other based on the residual errors generated from estimating and compensating different impairments. Since it is a little bit hard to study the receiver statistics for individual CR receiver, it is better to search for an algorithm that is robust enough for synchronization errors and channel effects.

In this chapter, we present a spectrum monitoring technique, namely the *energy ratio* (ER) technique, that is suitable for OFDM-based cognitive radios. During CR reception, this monitoring technique is designed to detect the reappearance of the primary user which has no constraints about its transmission scheme. Here, different signal chain impairments due to CFO, SFO, and NBI as well as frequency selective fading channels are considered. The technique operates over the OFDM signal chain and hence, it does not require to wait for the decoded bits. This implies fast response to PU appearance. Furthermore, the most important OFDM challenges for cognitive radios like power leakage are investigated and their effects on the proposed monitoring technique are considered.

4.2 Energy Ratio Algorithm Description

In the time-frequency grid for the OFDM frame, some tones are reserved for channel monitoring purpose. The tones are not modulated at the transmitter side and they are left as null sub-carriers. The tones are reserved for the whole time except the time of the training symbol(s) transmission as shown in Figure 4.1.

Based on the signal on the reserved tones at the receiver, the secondary user can monitor the band and test the primary user existence. In fact, this technique is not preferred when energy detection is employed to identify the primary user presence from the reserved tones [101]. This is totally true as the spectral leakage of the neighbouring sub-carriers will affect the energy at the reserved tones even for non primary user existence. Here, we propose another decision making variable that has some immunity for this power leakage.

After the frequency domain processing to the received signal at the secondary receiver, the reserved tones from different OFDM symbols are combined to form one sequence of

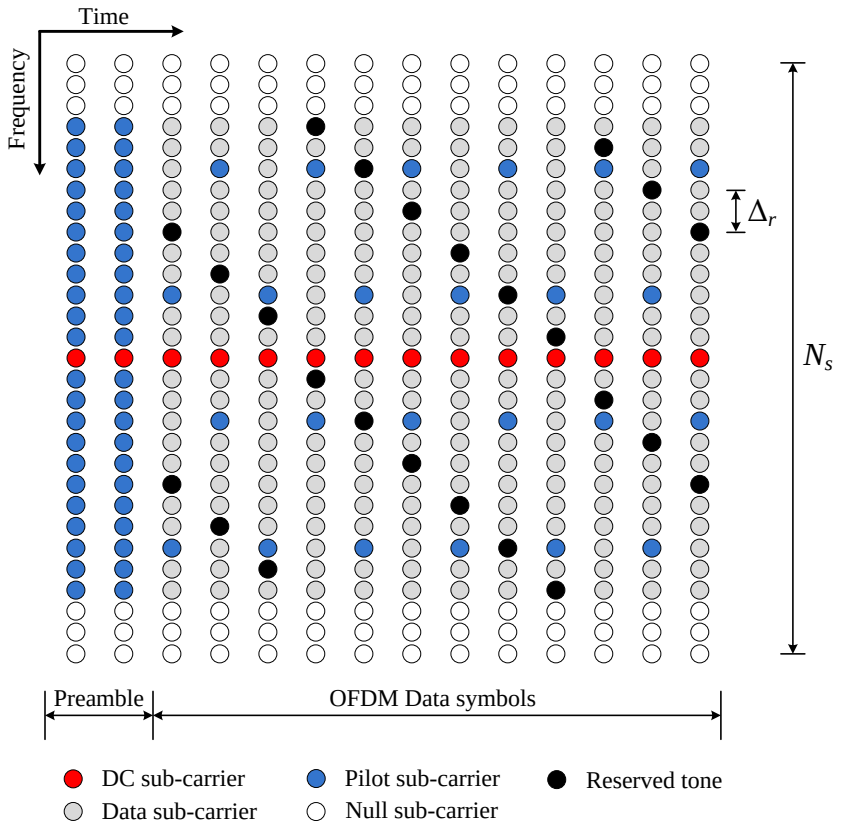

Figure 4.1: Reserved tones inside one OFDM frame

complex samples. Two consecutive equal-sized sliding windows are passed over the reserved tone sequence in the time direction. The energy of the samples that fall in one window is evaluated and the ratio of the two energies is taken as the decision making variable and hence the name *energy ratio*. In a mathematical form, let Z_i be the i^{th} sample of the reserved tone sequence. The decision making variable, X_k, can be defined as given by (4.1) where N is the number of samples per window, U_k is the energy of the second window, V_k is the energy of the first window, and k is an integer such that $k = 1, 2, 3, ...$

$$X_k = \frac{U_k}{V_k} = \frac{\sum_{i=N+k}^{2N+k-1} |Z_i|^2}{\sum_{i=k}^{k+N-1} |Z_i|^2} \tag{4.1}$$

The decision variable tests the change in variance on the reserved tones for the time of the two sliding windows. After the usual spectrum sensing, the receiver would monitor the reserved tones by evaluating the parameter, X_k. If the variable exceeds certain threshold, then the secondary user assumes that the primary has reappeared and it is time to vacate the band. If not, the SU maintains communication. Indeed, if there is no primary user in

band, then the energy of each window will only represent the noise, the leakage from the neighbouring symbols, and the ICI effects, and therefore, the ratio will be very close to unity.

Once the primary user appears, the second window will have three types of signalling which are the noise, the leakage and ICI effects, and the primary user interference. Meanwhile, the first window will only maintain the noise, the leakage and ICI effects. The ratio of the energy will result in much higher values when compared to one. This will depend on the primary user power. We will refer to the ratio of the primary user power to the secondary user noise at the receiver to be PNR. For the time being, we would neglect the effect of the leakage just to study the algorithm and we will investigate the effect of the secondary user power leakage afterwords.

4.3 Energy Ratio Analysis

The problem of spectrum sensing is to decide whether a particular slice of the spectrum is "available" or not. That is, in its simplest form, we want to discriminate between the two hypotheses $\mathcal{H}_0$ and $\mathcal{H}_1$ where the first assumes that the primary signal is not in band and the other assumes primary user presence. Using the *energy ratio* algorithm, we can define these hypotheses as given by (4.2). We have shown that the variable X will be very close to unity when the two windows carry noise only, on the other hand the ratio U/V will exceed the unity when there is some meaningful signal for the primary user.

$$\begin{cases} \mathcal{H}_0 : \ X = \frac{U}{V}, \quad \sigma_u^2 = \sigma_v^2 \\ \mathcal{H}_1 : \ X = \frac{U}{V}, \quad \sigma_u^2 > \sigma_v^2 \end{cases} \tag{4.2}$$

Similar to the conventional detectors, the performance of the detection algorithm can be summarized with two probabilities: probability of detection P_D and probability of false alarm P_{FA}. P_D is the probability of detecting a primary signal when it is truly present. The detection probability can be defined as given by (4.3) where γ is a threshold that should be determined. P_{FA} is the probability that the test incorrectly decides that the primary user is present when it is actually not. The false alarm probability can be defined as given by (4.4). Generally, P_{FA} should be kept as small as possible in order to prevent underutilization of transmission opportunities while P_D needs to be as large as possible.

$$P_D = Prob\big[X > \gamma \,|\, \mathcal{H}_1\big] \tag{4.3}$$

$$P_{FA} = Prob\big[X > \gamma \,|\, \mathcal{H}_0\big] \tag{4.4}$$

4.3.1 CDF Derivation for the Decision Making Variable

Let $z(t)$ be a Gaussian random process that is complex in general. The process is Gaussian if their samples are jointly Gaussian. Therefore, if the random process is sampled N times, we obtain the random variables Z_1, Z_2, Z_3, ..., Z_N which are jointly Gaussian. Now, assume that these random samples are independent and identically distributed, thus the samples are uncorrelated. Each sample Z_i is treated as a scalar complex random variable having a real part R_i and a complex part I_i. If we further assume that Z_i is circularly symmetric complex Gaussian (CSCG) random variable, then its real and imaginary parts are independent and have the same distribution such that $R_i \sim \mathcal{N}(0, \sigma^2)$ and $I_i \sim \mathcal{N}(0, \sigma^2)$.

Let V represent the energy of N adjacent samples of the random process $z(t)$ such that:

$$V = \sum_{i=1}^{N} \big|Z_i\big|^2 = \sum_{i=1}^{N} R_i^2 + I_i^2 \tag{4.5}$$

Since R_i and I_i are independent and identically distributed (i.i.d) random variables that follow Gaussian distribution with zero-mean and variance σ^2, the probability density function for the squared random variable R_i or I_i can be obtained as given by (4.6) where Y_i represents the random variable which is the square of either R_i or I_i. The characteristics function for the random variable Y_i can be obtained as given by (4.7).

$$f_{Y_i}(y) = f_{R_i}(\sqrt{y}) \left.\frac{dR_i}{dY_i}\right|_{R_i=\sqrt{y}} + f_{R_i}(-\sqrt{y}) \left.\frac{dR_i}{dY_i}\right|_{R_i=-\sqrt{y}} = \frac{1}{\sqrt{2\pi y}\,\sigma}\, e^{-y/(2\sigma^2)} \tag{4.6}$$

$$\begin{aligned}\Phi_{Y_i}(\omega) &= E\left[e^{j\omega Y_i}\right] = \frac{1}{\sqrt{2\pi}\,\sigma} \int_0^\infty \frac{1}{\sqrt{y}} e^{-y/(2\sigma^2)}\, e^{j\omega y}\, \mathrm{d}y \\ &= \frac{1}{\sqrt{2\pi}\,\sigma}\, \frac{2\sigma^2}{1-j2\omega\sigma^2} \sqrt{\frac{1-j2\omega\sigma^2}{2\sigma^2}} \int_0^\infty \acute{y}^{\frac{1}{2}-1}\, e^{-\acute{y}}\, \mathrm{d}\acute{y} \\ &= \frac{\Gamma(\frac{1}{2})}{\sqrt{\pi}\,\sqrt{1-j2\omega\sigma^2}} = \frac{1}{\sqrt{1-j2\omega\sigma^2}}\end{aligned} \tag{4.7}$$

As the process $z(t)$ has i.i.d samples, which implies that the sample Y_i are also independent. The summation of $2N$ samples of Y_i results in the desired random variable V which has the characteristic function given by (4.8).

$$\Phi_V(\omega) = \prod_{i=1}^{2N} \Phi_{Y_i}(\omega) = \frac{1}{\left(1-j2\omega\sigma^2\right)^N} = \frac{1}{2^N\,\sigma^{2N}\left(\frac{1}{2\sigma^2}-j\omega\right)^N} \tag{4.8}$$

It is known that the characteristic function is nothing but the inverse Fourier transform for the probability density function. Therefore, if we applied the Fourier transform frequency derivative property N times on the real exponential function, we would get the characteristics function of the random variable V and hence having the Fourier transform results in the probability density function of the random variable V which is given by (4.9). It is obvious that V follows a Chi-Squared distribution with the parameters σ and $2N$ such that $V \sim \chi^2_{2N}(\sigma)$.

$$f_V(v) = \frac{1}{2^N\,\sigma^{2N}\,(N-1)!}\, v^{N-1}\, e^{-v/(2\sigma^2)}, \qquad v > 0 \tag{4.9}$$

Now, we can consider the probability density function for the energy ratio random variable X defined by (4.10). We will assume that the random variables U and V have the same parameter N but have in general different σ such that $V \sim \chi^2_{2N}(\sigma_v)$ and $U \sim \chi^2_{2N}(\sigma_u)$.

$$X = \frac{U}{V} = \frac{\sum_{i=N+1}^{2N} |Z_i|^2}{\sum_{i=1}^{N} |Z_i|^2} \tag{4.10}$$

The PDF for the random variables V and U can be written as given by (4.11) and (4.12), respectively.

$$f_V(v) = \frac{1}{2^N\,\sigma_v^{2N}\,(N-1)!}\,v^{N-1}\,e^{-v/(2\sigma_v^2)}, \qquad v>0 \tag{4.11}$$

$$f_U(u) = \frac{1}{2^N\,\sigma_u^{2N}\,(N-1)!}\,u^{N-1}\,e^{-u/(2\sigma_u^2)}, \qquad u>0 \tag{4.12}$$

The CDF for the random variable X, can be evaluated as given by (4.13).

$$\begin{aligned} F_X(x) &= \text{Prob}\big[X\le x\big] = \text{Prob}\big[U\le xV\big] = \int_0^\infty\int_0^{xv} f_{UV}(u,v)\,\mathrm{d}u\,\mathrm{d}v \\ &= \int_0^\infty\int_0^{xv} \frac{1}{2^{2N}\,\sigma_v^{2N}\,\sigma_u^{2N}\,\Gamma(N)\,\Gamma(N)}\,u^{N-1}\,e^{-u/(2\sigma_u^2)}\,v^{N-1}\,e^{-v/(2\sigma_v^2)}\,\mathrm{d}u\,\mathrm{d}v \\ &= \frac{1}{2^{2N}\,\Gamma^2(N)}\int_0^\infty\left[\int_0^{x\acute{v}\,\sigma_v^2/\sigma_u^2}\acute{u}^{N-1}\,e^{-\acute{u}}\,\mathrm{d}\acute{u}\right]\acute{v}^{N-1}\,e^{-\acute{v}}\,\mathrm{d}\acute{v} \end{aligned} \tag{4.13}$$

In order to obtain the probability density function $f_X(x)$, we have to differentiate $F_X(x)$ with respect to X. This results in a differentiation under integration sign which can be solved to obtain a closed form expression for $f_X(x)$ as given by (4.14). It is obvious that the probability density function for X follows a scaled F-distribution which has the mean $m_X = \big(\Gamma(N-1)\,\Gamma(N+1)/\Gamma^2(N)\big)\times\big(\sigma_u^2/\sigma_v^2\big)$ and the variance $\text{Var}(X) = \big(\Gamma(N-2)\,\Gamma(N+2)/\Gamma^2(N)\big)\times\big(\sigma_u^2/\sigma_v^2\big)^2$.

$$\begin{aligned} f_X(x) &= \frac{\mathrm{d}}{\mathrm{d}x}F_X(x) = \frac{1}{2^{2N}\,\Gamma^2(N)}\int_0^\infty\frac{\mathrm{d}}{\mathrm{d}x}\left[\int_0^{x\acute{v}\,\sigma_v^2/\sigma_u^2}\acute{u}^{N-1}\,e^{-\acute{u}}\,\mathrm{d}\acute{u}\right]\acute{v}^{N-1}\,e^{-\acute{v}}\,\mathrm{d}\acute{v} \\ &= \frac{1}{2^{2N}\,\Gamma^2(N)}\int_0^\infty\left[\left(\frac{\acute{v}\,\sigma_v^2}{\sigma_u^2}\right)\left(\frac{x\acute{v}\,\sigma_v^2}{\sigma_u^2}\right)^{N-1}e^{-x\acute{v}\,\sigma_v^2/\sigma_u^2}\right]\acute{v}^{N-1}\,e^{-\acute{v}}\,\mathrm{d}\acute{v} \\ &= \frac{x^{N-1}}{\Gamma^2(N)}\left(\frac{\sigma_v^2}{\sigma_u^2}\right)^N\frac{\Gamma(2N)}{\Big(1+\sigma_v^2\,x/\sigma_u^2\Big)^{2N}}\left[\int_0^\infty\frac{\Big(\acute{v}\big(1+\sigma_v^2\,x/\sigma_u^2\big)\Big)^{2N}}{2^{2N}\,\Gamma(2N)}e^{-\acute{v}\left(1+\sigma_v^2\,x/\sigma_2^2\right)}\,\frac{\mathrm{d}\acute{v}}{\acute{v}}\right] \\ &= \frac{\sigma_v^2}{\sigma_u^2}\,\frac{\Gamma(2N)}{\Gamma^2(N)}\,\frac{\Big(\sigma_v^2\,x/\sigma_u^2\Big)^{N-1}}{\Big(1+\sigma_v^2\,x/\sigma_u^2\Big)^{2N}}, \qquad x\ge 0 \end{aligned} \tag{4.14}$$

Finally, the CDF for X can be derived in a closed form as given by (4.15) where $I_b(N,N)$ is the regularized incomplete beta function with the parameters b and N.

$$\begin{aligned} F_X(x) &= Prob\big[X \le x\big] = \int_{-\infty}^{x} f_X(t)\,\mathrm{d}t = \frac{\sigma_v^2}{\sigma_u^2}\frac{\Gamma(2N)}{\Gamma^2(N)}\int_0^x \frac{\left(\sigma_v^2\, t/\sigma_u^2\right)^{N-1}}{\left(1+\sigma_v^2\, t/\sigma_u^2\right)^{2N}}\,\mathrm{d}t \\ &= \frac{\Gamma(2N)}{\Gamma^2(N)}\int_0^{(\sigma_1^2\, x/\sigma_u^2)/(1+\sigma_v^2\, x/\sigma_u^2)} u^{N-1}\,(1-u)^{N-1}\,\mathrm{d}u \\ &= I_{\frac{(\sigma_v^2\, x/\sigma_u^2)}{(1+\sigma_v^2\, x/\sigma_u^2)}}(N,N) \end{aligned} \tag{4.15}$$

4.3.2 Energy Ratio Performance

We will use the classical NP criterion where the threshold is selected based on a fixed value for P_{FA} and accordingly, the detection probability is obtained for a known threshold value. By substituting the CDF function, $F_X(x)$, derived in the previous section for the decision making variable, X, in (4.4), one can write the probability of false alarm in case of *energy ratio* algorithm as given by (4.16). Also, we can obtain the threshold γ subjected to a constant P_{FA} as given by (4.17) where $I_x^{-1}(N,N)$ is the inverse incomplete beta function.

$$P_{FA} = Prob\big[X > \gamma \,|\, \mathcal{H}_0\big] = 1 - F_{X\,|\,\mathcal{H}_0}(\gamma) = 1 - I_{\frac{(\gamma)}{(1+\gamma)}}(N,N) \tag{4.16}$$

$$\gamma = \frac{I^{-1}_{1-P_{FA}}(N,N)}{1-I^{-1}_{1-P_{FA}}(N,N)} \tag{4.17}$$

Under $\mathcal{H}_1$, the reserved tones carry the noise power and the primary signal power in the second window (i.e. $\sigma_u^2 = \sigma^2_{\text{noise}} + \sigma^2_{\text{primary}}$) while the first window contains noise only (i.e. $\sigma_v^2 = \sigma^2_{\text{noise}}$). Therefore, the primary signal power to the secondary noise power, PNR, can be obtained as given by (4.18) from which the detection probability can be obtained as a function of PNR as given by (4.19).

$$\sigma_u^2 \;=\; \sigma_{\text{noise}}^2 + \sigma_{\text{primary}}^2 \;=\; \sigma_{\text{noise}}^2\left[1 + \frac{\sigma_{\text{primary}}^2}{\sigma_{\text{noise}}^2}\right] \qquad \Rightarrow \qquad \text{PNR} \;=\; \frac{\sigma_u^2}{\sigma_v^2} - 1 \tag{4.18}$$

$$\begin{aligned} P_D \;&=\; Prob\big[X > \gamma \,|\, \mathcal{H}_1\big] \;=\; 1 - F_{X\,|\,\mathcal{H}_1}(\gamma) \\ &=\; 1 - I_{\frac{(\sigma_v^2\,\gamma/\sigma_u^2)}{(1+\sigma_v^2\,\gamma/\sigma_u^2)}}(N,N) \;=\; 1 - I_{\frac{(\gamma/(1+\text{PNR}))}{(1+\gamma/(1+\text{PNR}))}}(N,N) \end{aligned} \tag{4.19}$$

4.4 OFDM Challenges in Energy Ratio Algorithm

4.4.1 NBI and Power Leakage

By definition, the power of a NBI is concentrated in a small frequency band compared to the overall system bandwidth [102]. Although the total power of the interference may be substantially lower than the total received signal power, these disturbances can reach a noise level which exceeds the received signal level by orders of magnitude inside the interference band. Therefore, the system performance will be severely degraded. Aside from NBI, the side-lobes of modulated OFDM sub-carriers even in case of having no NBI are known to be large. As a result, there is power leakage from sub-carriers to adjacent sub-carriers. It is known that the most efficient solution to NBI is to disable the sub-carriers corresponding to this interference. This will eliminate the effect of NBI at those sub-carriers, however, the signal to noise ratio at the other sub-carriers will be slightly reduced.

For the power leakage, recent research has carefully addressed this problem. For example, the out of band leakages can be reduced by including special cancelling carriers at the edge of the band [103]. These sub-carriers are modulated with complex weighting factors which are optimized such that the side-lobes of the those carriers cancel the side-lobes of the original transmitted signal in a certain optimization range. Another solution is proposed in [104] where the power leakage is totally suppressed by a pre-coding technique. This pre-coding is applied to the frequency domain OFDM signal before IDFT block at the transmitter side. At the receiver, a decoder is applied to omit the spectral distortion to the OFDM signal caused by pre-coding. This technique can totally eliminate the effect of spectral leakage but

of course it needs full revision for all synchronization algorithms applied to traditional OFDM system.

By utilizing the fact that *energy ratio* can perfectly counter any consistent noise like signals, windowing can be applied to the time domain OFDM symbols [105] to limit the leakages and to reduce the influence of NBI. Thus, if a windowing function (e.g., Nyquist window) is carefully chosen to only affect the interference while leaving the OFDM signal unchanged, then spectral leakage can be avoided. In [105], a folding technique is proposed in order not to use a double length DFT. In this case, the samples preceding the OFDM symbol to the end of the symbol are added to the samples following the symbol to its beginning. To evaluate the performance of our *energy ratio* detector in the presence of NBI and power leakage, we turn off the sub-carriers corresponding to the NBI. Moreover, the time domain windowing technique with folding is applied at the receiver side, as it offers the lowest computational complexity with sufficiently good performance.

4.4.2 ICI Effect

Since CFO and SFO estimation and compensation is a must for traditional OFDM systems, we have to consider these issues when the *energy ratio* algorithm is evaluated in the presence of ICI. Since the *energy ratio* is concerned with the amount of change for the signal strength on the reserved tones, the performance of the algorithm will not be destroyed by ICI. However, this interference can be considered as an increase of the noise level and hence the *energy ratio* performance may be a little bit degraded due to the primary signal to noise ratio reduction at the reserved tones. It is worth to mention that we are not going to design or evaluate a synchronization engine for an OFDM system. Our target is just to emphasize that the *energy ratio* technique does not require any new solutions for the OFDM synchronization problems.

4.4.2.1 CFO Estimation and Compensation

Any practical system assumes a maximum acceptable frequency offset, $\mathrm{CFO}_{\max}$, between the transmitter and receiver. Therefore, the integer CFO range is known in prior as the maximum integer CFO is $\varepsilon_{i\max} = \lfloor \mathrm{CFO}_{\max}/\Delta f \rfloor$ and hence the integer CFO range will be $\mathbb{L} = \big[-\varepsilon_{i\max} \ -\varepsilon_{i\max}+1 \ ... \ -1 \ 0 \ 1 \ ... \ \varepsilon_{i\max}-1 \ \varepsilon_{i\max} \big]$. In [106], a two step time domain

estimation technique is introduced for CFO. This approach depends on the training symbols that are transmitted at the front of the OFDM frame. Actually, a good compromise between performance and complexity is achieved by this technique.

The idea is to first estimate the fractional CFO by a maximum likelihood estimator as given by (4.20) where $y(n)$ is the received time domain signal and $D = N_s + N_g$. It applies an autocorrelation to the time domain waveform with the condition that two or more training symbols are inserted at the beginning of the frame. The time domain signal is compensated for the fractional CFO resulting in the signal $y_{\text{comp}}(n)$. This signal is then cross-correlated with the transmitted time domain waveform for the training symbols, y_t, after applying a progressive phase shift that depends on the desired integer CFO as given by (4.21). This cross-correlation is repeated for each integer CFO in $\mathbb{L}$ and the maximum is searched for. The integer CFO that corresponds to the maximum correlation is taken as the estimated integer CFO. Once the normalized CFO is estimated, the OFDM signal can be compensated by rotating the phase of the time domain signal by $-2\pi(\hat{\varepsilon}_f + \hat{\varepsilon}_i)n$ where n is the time index.

$$\hat{\varepsilon}_f = \frac{1}{2\pi D}\angle\left\{\sum_{n=0}^{n=N_s-1} y(n)\, y^*(n+D)\right\} \tag{4.20}$$

$$\hat{\varepsilon}_i = \max_{m\in\mathbb{L}}\left|\sum_{n=0}^{n=N_s-1} y_{\text{comp}}(n)\, y_t^*(n)\, e^{-2\pi jmn/D}\right| \tag{4.21}$$

4.4.2.2 SFO Estimation and Compensation

In [67], the carrier-frequency and timing offsets are jointly estimated by applying a Weighted Least-Squares (WLS) algorithm where a weighting matrix, $\mathbf{W}$, is designed to improve the estimation accuracy of the least-squares. The analytical results show that this matrix should be a function of the noise variance. In fact, if an incorrect (estimated) value of the noise variance is used, then the resulting estimation accuracy may perform rather poorly.

Since the *energy ratio* is strong enough to compact ICI, we can simply apply the WLS algorithm by replacing $\mathbf{W}$ with an identity matrix. This reduces the WLS algorithm into the well-known least-squares estimation. First, we compute the averaged phase difference between the pilots contained in two consecutive OFDM training symbols in the frequency domain to obtain $\mathbf{y} = \begin{bmatrix} y_0 & y_1 & \dots & y_{J-1} \end{bmatrix}^T$ where J is the number of pilots inserted in one

preamble symbol. Second, the pilot sub-carrier indexes denoted by $x_j, j = 0, 1, 2, \ldots J-1$ are arranged to construct the helping matrix $\mathbf{X}$ which is given by (4.22). Finally, the estimated carrier-frequency offset $\hat{\varepsilon}$ and timing offset $\hat{\delta}$ can be obtained by (4.23).

$$\mathbf{X} = \begin{bmatrix} x_0 & x_1 & x_2 & \ldots & x_{J-1} \\ 1 & 1 & 1 & \ldots & 1 \end{bmatrix}^T \tag{4.22}$$

$$\begin{bmatrix} \hat{\delta} & \hat{\varepsilon} \end{bmatrix}^T = \frac{N_s}{2\pi(N_s + N_g)} \left(\mathbf{X}^* \, \mathbf{X}\right)^{-1} \mathbf{X}^* \, \mathbf{y} \tag{4.23}$$

4.5 Energy Ratio Algorithm Over Fading Channels

To study the effect of the frequency selective fading channel on the *energy ratio* algorithm, we are going to first consider the single-input single output (SISO) model where a secondary transmitter communicates with its own receiver over the channel h_{ss}. During the transmission, the primary user may try to send his own data which is received by the secondary receiver across the channel h_{ps}. Both signals are combined at the receiver antenna and then processed as one received stream. The receiver noise is added to the combined signals and the result is converted to the frequency domain by the DFT block. The reserved tone sequence is then organized in order to be processed by the monitoring algorithm.

If $r_i^k, i = 0, 1, ..., N_{RT}-1$ denotes the reserved tone indices for the k^{th} OFDM data symbol where N_{RT} is the number of reserved tones per OFDM symbol, then the j^{th} reserved tone can be modelled as given by (4.24) where $X_s(r_j^k)$, $X_p(r_j^k)$, $H_{ss}(r_j^k)$, $H_{sp}(r_j^k)$, and $n(r_j^k)$ are the secondary user transmitted symbol, the primary user transmitted symbol, the frequency domain response for the secondary channel, the frequency domain response for the primary channel, and the noise sample, respectively, where all are observed at sub-carrier r_j^k. Since the secondary transmitter forces the reserved tones to be nulls, then $X_s(r_j^k) = 0 \ , \ \forall j$ and hence the received reserved tones reduce to just the effect of the primary user and the noise of the secondary receiver under perfect synchronization and neglecting the power leakage effect. Therefore, if (by luck) the primary signal power is fairly distributed among different sub-carriers, then the *energy ratio* algorithm can behave as AWGN even when the channel

is frequency selective fading channel for both primary and secondary users.

$$Y(r_j^k) \;=\; H_{ps}(r_j^k)X_p(r_j^k) + H_{ss}(r_j^k)X_s(r_j^k) + n(r_j^k) \;=\; H_{ps}(r_j^k)X_p(r_j^k) + n(r_j^k) \qquad (4.24)$$

Unfortunately, the power transmitted by the primary user is in practice scaled by different weights over different sub-carriers so that the power spectral density of the primary user received signal is not constant over the observed band. In fact, when the monitoring tones are reserved at fixed sub-carrier indices and the channel exhibits a deep fade at those tones, the primary signal power sensed by the monitoring algorithm is very weak even if the average primary power is high. Moreover, the primary signal to noise ratio on the reserved tones changes with different channel realizations as we do not consider the whole band in which the primary user appears. The problem is that we just monitor a very limited band inside the desired band and the channel may affect the amount of power seen in this very narrow band.

The problem can be overcome by considering large number of monitoring sub-carriers which is equivalent to monitor wider band or by fully determining the primary user channel. These solutions are obsolete as the throughput of the secondary user will be highly reduced and the primary signal is assumed to be totally unknown for the secondary receiver, thus the channel can not be estimated. We propose a simple and efficient solution for this problem instead of observing wider band and without the need to estimate the primary channel. We can in fact allocate the reserved tones dynamically so that the reserved tones indices span the whole band when successive OFDM symbols are considered in time. The tones are advanced by Δ_r positions every OFDM symbol as shown in Figure 4.1. When the last index of the available sub-carriers is reached, the spanning starts again from the first sub-carrier. Now, by considering small values for Δ_r, the reserved tone sequence injected to the *energy ratio* spans the whole band and the channel effect is averaged over time. If the *energy ratio* window is large enough and Δ_r is small enough, then the average power of the primary user is almost included in the second window when the primary user appears.

To further reduce the narrow band effect without increasing the number of reserved tones per one OFDM symbol, multiple-antennas at the receiver side can totally enhance the monitoring performance. For Single-Input Multiple-Output (SIMO) or Multiple-Input

Multiple-Output (MIMO) systems, if the number of receiver antennas is N_{Rx}, there will be N_{Rx} available sets of reserved tones at the receiver for each OFDM symbol or equivalently $N_{Rx} \times N_{RT}$ reserved tones every OFDM symbol. The *energy ratio* technique will combine all these sets together to form the reserved tone sequence. The confidence of primary user presence is increased by the diversity gain obtained from the independent channel paths. This allows more robust decision when compared to the SISO case. The channel effect is reduced and a good averaging for the channel is done by combining more samples at the same time. Effectively, applying SIMO or MIMO is equivalent to increasing the window size by a factor of N_{Rx}. If the same performance is required, the window size can be reduced by N_{Rx} which implies that the primary user power is sensed in less time when compared to the SISO case. Otherwise, increasing the window size directly increases the mean of the decision making variable when the primary signal is active which allows higher detection probability and less false alarm.

4.6 Simulation Results

In this section, we will show the simulation results for the *energy ratio* algorithm and we will study different aspects from simulation point of view. Throughout these simulations, we have used an OFDM system that employs a total of $N_s = 1024$ sub-carriers, 224 of which are used as guard bands on both ends of the signal band. There are 32 pilot sub-carriers and $N_r = 4$ reserved tones, distributed across the entire 800 sub-carriers. Therefore, the throughput reduction due to reserved tones is only 0.5% which is an inconsiderable amount for high data rates. The cyclic prefix is $N_g = 64$ samples long and the sampling frequency is 16MHz. The sub-carrier spacing is then $\Delta f = 15.625$ KHz which is large enough to neglect the phase noise distortion and the time domain windowing effect. Unless otherwise specified, the frame has two consecutive training symbols and 256 OFDM data symbols. The data is modulated by 64-QAM mapper and the secondary power to noise ratio in the absence of primary signal is assumed 9dB. When the system operates under non-perfect synchronization, the maximum acceptable CFO is assumed to be 400KHz, the CFO is 320KHz, and the sampling clock offset is assumed to be 100 ppm.

4.6.1 Analytical Verification

Figure 4.2 shows a comparison between the PDF given by (4.14) and the one obtained from simulation where we have used $10\log_{10}(\sigma_u^2/\sigma_v^2) = 5$dB and an *energy ratio* window $N = 32$. To obtain the simulated PDF, 10^7 circularly symmetric Gaussian distributed samples are generated and scaled properly for both windows. The samples are then applied to the *energy ratio* algorithm and the PDF is obtained by considering the histogram of the decision making variable. It is obvious that the analytical results are in excellent agreement with the simulated ones.

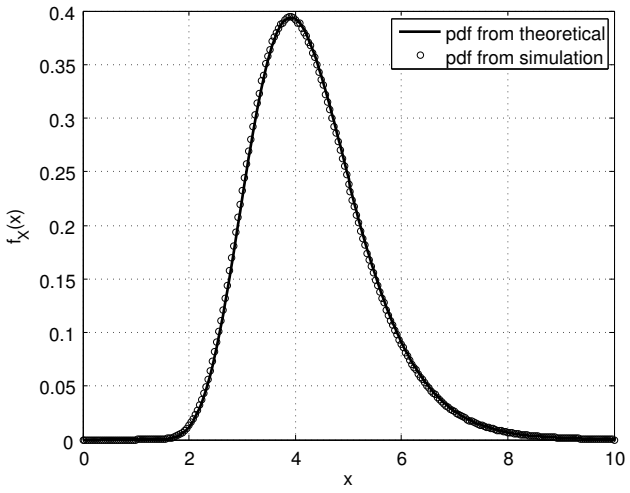

Figure 4.2: Simulated PDF versus analytical PDF for the *energy ratio* decision making variable with N =32 and $10\log_{10}(\sigma_u^2/\sigma_v^2) = 5$dB

Next, the hypothesis test is to be verified by exploring the conditional PDF under both $\mathcal{H}_0$ and $\mathcal{H}_1$. In fact, when there is no primary user in band, the decision variable follows only one unique PDF that is shown in Figure 4.3. Under $\mathcal{H}_1$, the conditional PDF depends on the PNR ratio. Four additional curves are also shown in Figure 4.3 for the conditional PDF under $\mathcal{H}_1$ with four different PNR values (-2, 0, 2, and 4 dB). It is clear that the decision variable can distinguish between no primary user case and primary user presence based on the PNR.

4.6.2 Receiver Characteristics

The detection probability for four different false alarm probabilities is shown in Figure 4.4. The horizontal axis denotes the secondary to primary power ratio (SPR) which is related to the primary to secondary noise ratio (PNR) such that $\text{PNR}\big|_{\text{dB}} = \text{SNR}\big|_{\text{dB}}\text{-SPR}\big|_{\text{dB}}$, where SNR is the secondary power to noise power ratio. It is to be noticed that, PNR is the ratio that determines the performance of the *energy ratio* algorithm whereas SPR is assumed to be the main parameter by which a monitoring algorithm is evaluated.

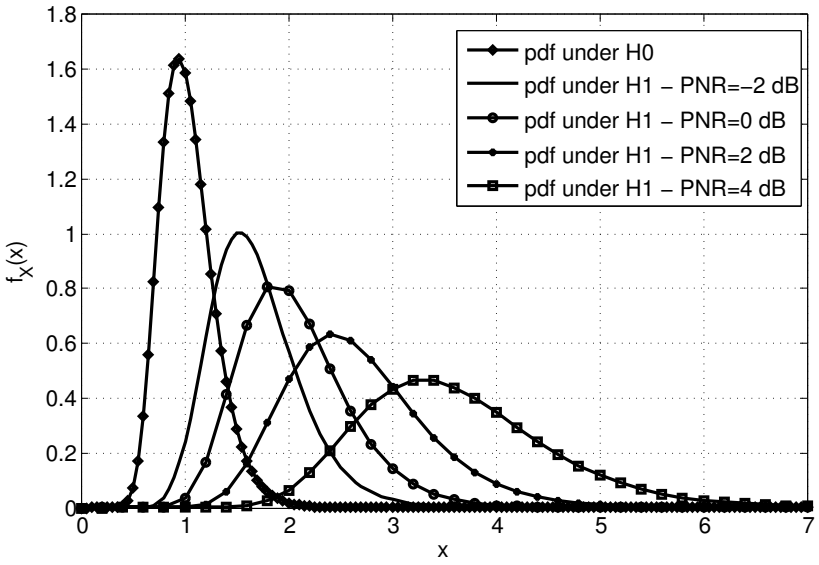

Figure 4.3: Conditional PDF under $\mathcal{H}_0$ and conditional PDF under $\mathcal{H}_1$ for PNR=-2, 0, 2, and 4 dB

The ROC for the *energy ratio* for different values of SPR is shown in Figure 4.5. These results are obtained by simulating the OFDM system twice, one when primary signal is present and the second when it is absent. The system is run over 10^6 realizations and the probability of detection or false alarm is evaluated. The threshold is set based on the theoretical value given by (4.17).

In order to compare the proposed monitoring algorithm with the receiver statistics technique found in [100], the OFDM system is simulated such that the system parameters match the simulation environment followed by [100]. The simulation is run for 4-QAM under SNR = 6dB, P_{FA} =0.04, and N=128. Figure 4.6 shows the simulation results for the de-

tection probability of the *energy ratio* algorithm in comparison with the results obtained in [100]. In addition of having fast detection, it is noted that the *energy ratio* shows a better performance than the receiver statistics algorithm.

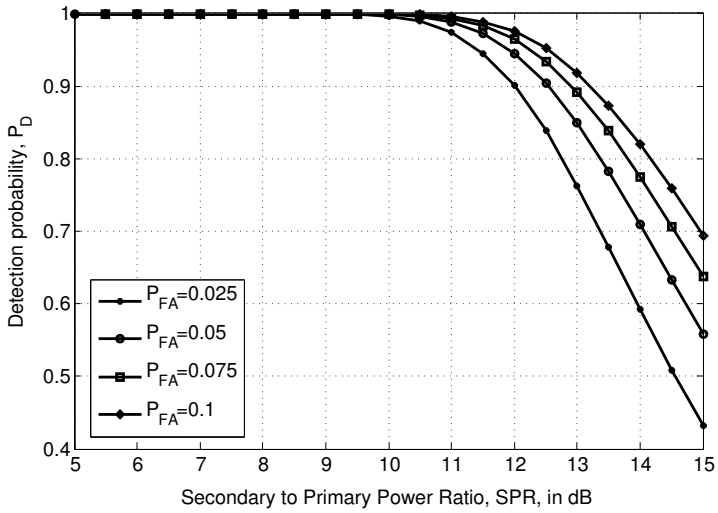

Figure 4.4: The detection probability at fixed false alarm probability under perfect synchronization and neglecting the power leakage effect

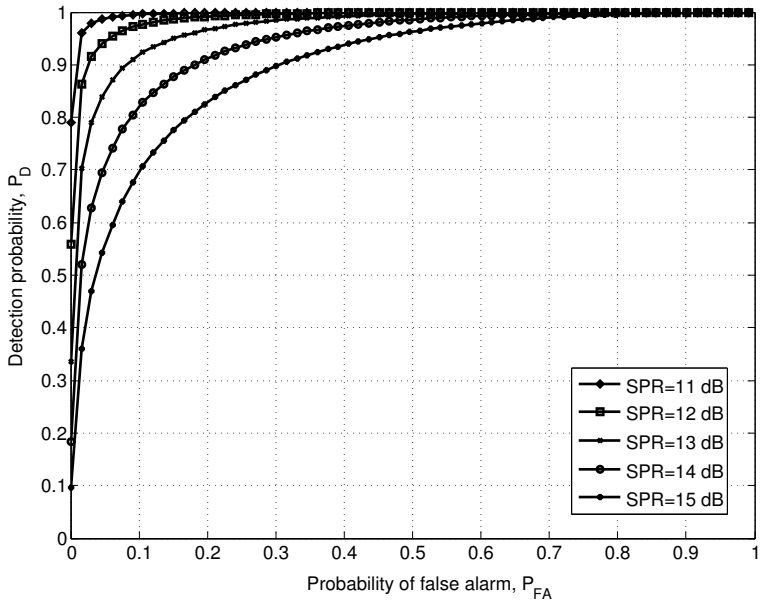

Figure 4.5: Receiver operating characteristics for different PNR values under perfect synchronization and neglecting the power leakage effect

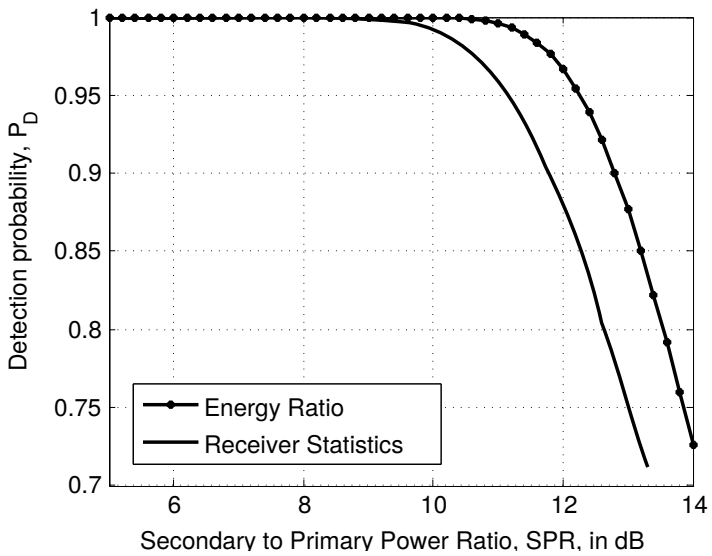

Figure 4.6: Comparison between *energy ratio* and receiver statistics [100] algorithms in case of QPSK, SNR = 6 dB, $P_{FA} = 0.04$, and N =128

4.6.3 OFDM Challenges

The power leakage is modelled by applying oversampling to the frequency domain signal, where the number of points at the receiver DFT is four times the number used at the transmitter. Time domain Hanning window with folding is applied at the receiver to limit the NBI and power leakage. Also the phase of the time domain samples is rotated by $2\pi\varepsilon n$ to model the receiver CFO where n is the time index. Moreover, the received signal is re-sampled at time instances that are multiple of $(1+\delta)T_s$ to model the receiver SFO. The preamble detection and the exact frame timing is assumed to be perfect. Here the time domain preamble is used to estimate and compensate for the CFO. The CFO compensated signal is converted to the frequency domain via DFT. The SFO, $\hat{\delta}$, and the residual CFO are further estimated by applying the least squares algorithm discussed in Section 4.4.2.2. Moreover, the time domain signal is re-sampled according to the delay $\hat{\delta}$ to compensate for the SFO.

Figure 4.7 shows the mean square error for the estimated CFO and SFO. From these results, we can see that the residual fractional CFO and SFO at 9dB are 9×10^{-3} and 5×10^{-6}, respectively. This implies SNR degradation of $\text{SNRD}_{\text{CFO}} = 0.0092$ dB for CFO, and $\text{SNRD}_{\text{SFO}}(1023) = 0.003$ dB for SFO at the last sub-carrier, based on (2.5) and (2.6),

respectively. This shows the advantages of the powerful estimation techniques we have chosen for the OFDM synchronization engine.

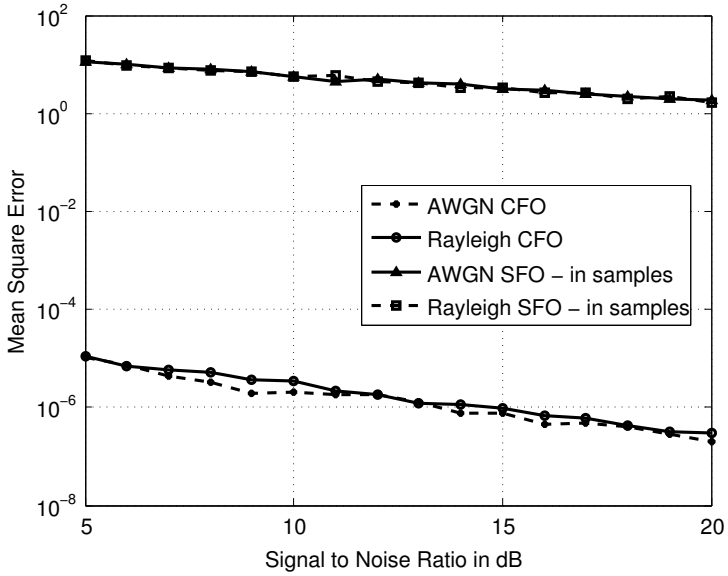

Figure 4.7: MSE for both CFO and SFO estimation under AWGN and Rayleigh fading channels. The MSE for SFO is measured in samples.

To examine the combined effects of OFDM impairments, the detection probability for the *energy ratio* is simulated in the presence of power leakage, CFO, and SFO as shown in Figure 4.8. As we claimed earlier, the *energy ratio* is shown to be robust to OFDM challenges as only minor degradation in detection performance is noted compared to the perfect case. For instance, the overall loss due to all impairments is only 0.4 dB at a detection probability $P_D = 0.9$.

4.6.4 Effect of Frequency-Selective Fading

To study the effect of frequency-selectivity on the proposed *energy ratio* technique, the channel is modelled as a linear time-varying filter whose impulse response, $h(n)$, is obtained by: (1) N_g circularly symmetric Gaussian samples with unit variance. The number of channel taps is defined by the cyclic prefix length as we assume that the cyclic prefix fully defines the channel maximum excess delay. (2) The samples are scaled to fit the required Power Delay Profile (PDP) which is assumed to be exponentially decaying [107]. The OFDM system is

simulated in Rayleigh fading channel for different SPR. In Figure 4.9, we show the effect of Rayleigh fading channel on the *energy ratio* performance for SISO, 2×2 MIMO, and 4×4 MIMO systems. The Rayleigh fading channel effect is compared with the AWGN channel where a minor degradation is noticed due to the narrow band problem. From these results, it is clear that having more receive antennas will offer great enhancement to the detection accuracy of the *energy ratio* detector.

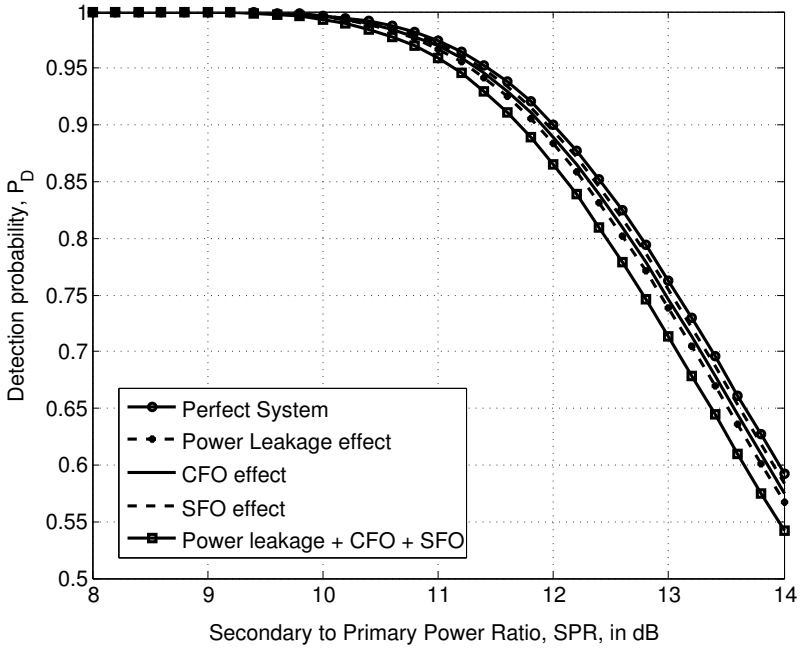

Figure 4.8: Power leakage, CFO, and SFO effects on the *energy ratio* algorithm at $P_{FA} = 0.025$

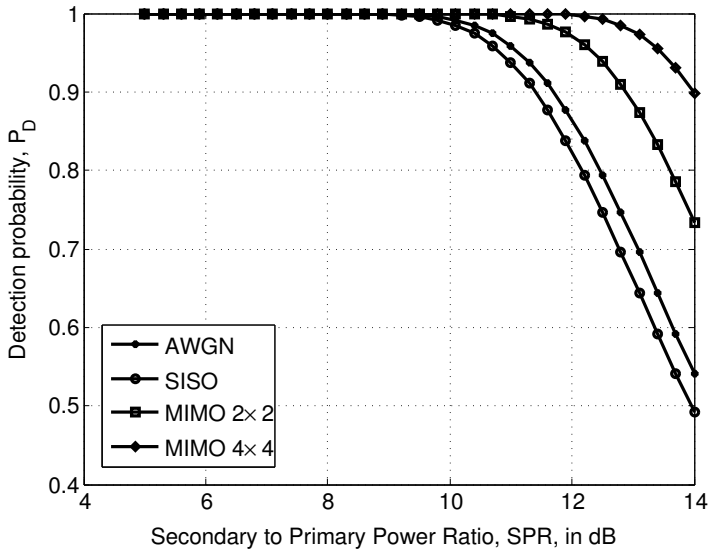

Figure 4.9: Rayleigh fading channel effect on *energy ratio* for SISO and MIMO systems taking power leakage and ICI into consideration. $P_{FA} = 0.025$, $\Delta_r = 2$, and $N = 128$

4.7 Summary

In this chapter, we have presented a spectrum monitoring algorithm that can sense the reappearance of the primary user during the secondary user transmission. The "*energy ratio*" algorithm is designed for OFDM systems such as Ecma-392 and IEEE 802.11af systems. We also derived the detection probability and the probability of false alarm for AWGN channels in order to analyze the performance of the proposed algorithm. Simulation results indicate that the detection performance is superior than the receiver statistics method. For computational complexity, the *energy ratio* architecture is investigated where it was shown that it requires only about double the complexity of the conventional energy detector. When frequency-selective fading is studied, the *energy ratio* algorithm is shown to achieve good performance that is enhanced by involving SIMO or MIMO systems. We have proven that the multiple receive antenna system will further result in a better detection accuracy by emulating the increase in sliding window size. Therefore, our proposed spectrum monitoring algorithm can greatly enhance the spectrum monitoring performance of OFDM-based cognitive networks with a very limited reduction in the secondary network throughput.

Chapter 5

Low Power Nyquist-based Wideband Sensing

5.1 Introduction

One major issue with Nyquist approaches is the power consumption associated with the RF front end, ADCs, and even the digital processing part that is operated by a very high sampling rate. Actually, low power consumption makes wideband sensing possible even at the secondary user equipments. These devices typically operate through batteries which have strict life time constraints. In this regard, it has been shown that ADC power consumes a significant portion of the total power dissipation and it needs a special attention [108]. We present a recent survey based on Texas Instruments ADCs to provide figure of merits for those quantities as shown in Figure 5.1, where part numbers are explicitly mentioned for all ADC items. These commercially available ADCs with these specifications consume power on the order of several Watts.

Reducing the ADC power consumption generally has three main axes. First, the sensing performance based on the conventional Nyquist approaches assume infinite precision of the acquired measurements in order to evaluate the presented algorithmic effort. In practice, signals need to be quantized before further processing, that is, the real-valued measurements need to be mapped to discrete values over some finite range. For this reason, the quantization impact on the spectrum sensing detection performance has been considered [109]. However, the influence of the quantization on the power consumption was not the main focus of this research effort. Second, wideband Nyquist approaches assume the availability of an ultra high sampling rate. However, it should be emphasized that all simulation results presented by previous research work including [110]-[111], consider relatively small band (order of 300MHz)

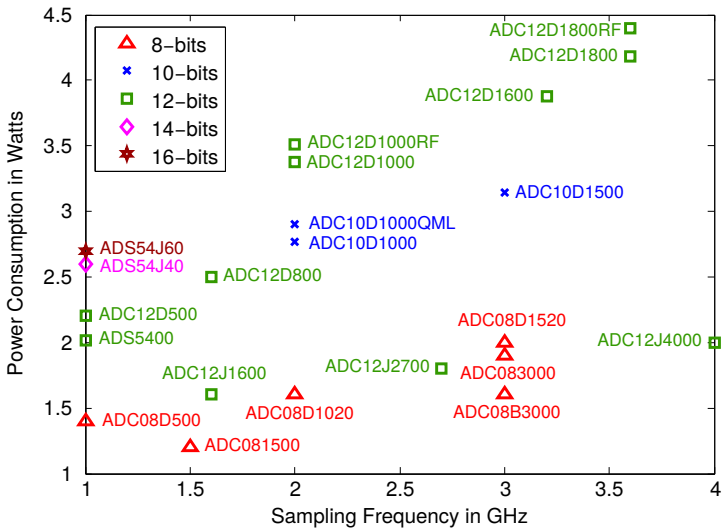

Figure 5.1: Power consumption versus sampling frequency of ADCs for resolutions 8, 10, 12, 14, and 16 bits

which is somehow in the order of a medium-sized band when compared to the practical wideband in the order of GHz. Allowing wideband sensing in the range of GHz makes it even challenging from the power budget perspective. Third, with lower bit resolution, the ADC power consumption can be significantly reduced. However, low resolution will again impact the sensing performance, which may result in a degradation in secondary network throughput. Thus, it is not easy to develop a wideband Nyquist-based sensing technique that maintains reasonable performance with efficient power consumption and reduced complexity. Due to the power consumption issue attached to high-speed high-resolution ADCs that are employed in the classical Nyquist-based approaches, in this chapter, we present two ultra low-power wideband sensing techniques. Both rely on employing 1-bit quantization which can provide significant power reduction.

5.2 System and Signal Models

From the network point of view, we consider a cognitive radio network of M PUs and many SUs. The CR system operates over a wideband channel divided into N non-overlapping sub-bands out of which M sub-bands are randomly assigned to the active PUs. Conventionally, it is assumed that the sub-bands have equal-size bandwidths B [112][113]. Each PU occupies

a spectrum slice with a bandwidth of B for its transmission. In fact, the spectrum is totally investigated or sensed by one SU (the master node or the fusion node) to decide whether each slice is a hole or not. At the fusion node receiver, the signal is sampled at the Nyquist sampling rate $F_s = NB$. The fusion node sends different data to the other SUs (the slave nodes) informing them about the slice to be used for their transmission.

At the fusion node receiver, an $N\times1$ vector can represent the received signal in the frequency domain as given by,

$$\mathbf{R} \;=\; \sum_{m=1}^{M} \mathbf{S}_m + \mathbf{W} \;=\; \sum_{m=1}^{M} \mathbf{H}_m \mathbf{T}_m + \mathbf{W} \tag{5.1}$$

where $\mathbf{H}_m$ is a diagonal $N \times N$ channel matrix representing the static fading channel over the sensing interval, $\mathbf{T}_m$ is an $N\times1$ vector representing the spectrum of the mth primary signal at the PU transmitter over the mth active sub-band, $\mathbf{S}_m$ is an $N\times1$ vector representing the spectrum of the mth primary signal at the SU receiver over the mth active sub-band, and $\mathbf{W}$ is an $N\times1$ vector representing the frequency domain independent and identically distributed circularly-symmetric AWGN with zero-mean and variance $\mathbb{E}[\mathbf{W}\mathbf{W}^H] = N\sigma_W^2$, where $\mathbb{E}$ denotes expectation. Similar to [114], it is assumed that the distribution of the received primary signal over a single sub-band is also circularly-symmetric complex Gaussian (CSCG) with zero-mean and variance σ_S^2. It should be emphasized that this assumption certainly holds only when primary radios deploy uniform power transmission strategies given no channel knowledge at the transmitter side [51][115]. Finally, all primary users and the noise are assumed to be statistically independent.

From the time domain perspective, due to the ultra high sampling rate compared to the typical PU baud rate, the mth narrowband PU signal can be represented by a single complex tone centred at the frequency f_m (which is the central frequency for one of the sub-bands). Accurately, the random variable representing the envelope of the received narrow-band PU signal is assumed to change at a rate of $1/N$ times slower than the sampling frequency. Therefore, after the multipath channel, each PU signal can be modelled as a narrowband signal with a complex envelop that has independent identically distributed (i.i.d) coefficients. The signal also can suffer from a general random delay that accounts for the channel excess delay and the general propagation delay within the observation interval or

observation window, namely T. Let us define the continuous time received signal at the SU receiver by $r(t)$ and the corresponding discrete version of the same signal by $r(n/F_s)$ as given by (5.2) and (5.3), respectively, where τ_m and correspondingly ε_m represent the amount of time shift for the candidate PU, A_m and B_m are independent Gaussian random variables with zero-mean and variance $\sigma_S^2/2$, and $w(t)$ is the time domain version of the AWGN noise process. The notation $\lfloor (n-\varepsilon_m)/N \rfloor$ interprets the index of the random variable sample with time. Notice that ε_m is also a random variable that can be modelled as a uniform random variable in the range $[0,\ N-1]$. Also, it has been assumed that the signals from various users and the noise are independent.

$$\begin{aligned} r(t) \;=\; & \sum_{m=1}^{M} \Big[A^m_{\lfloor (t-\tau_m)/T \rfloor} \cos(2\pi f_m (t-\tau_m)) - B^m_{\lfloor (t-\tau_m)/T \rfloor} \sin(2\pi f_m (t-\tau_m)) \\ & + \mathbf{j} \Big(A^m_{\lfloor (t-\tau_m)/T \rfloor} \sin(2\pi f_m (t-\tau_m)) + B^m_{\lfloor (t-\tau_m)/T \rfloor} \cos(2\pi f_m (t-\tau_m)) \Big) \Big] \\ & + w(t), \qquad 0 \le t < T,\ \mathbf{j} = \sqrt{-1} \end{aligned} \tag{5.2}$$

$$\begin{aligned} r(n) \;=\; & \sum_{m=1}^{M} \Big[A^m_{\lfloor (n-\varepsilon_m)/N \rfloor} \cos\big(2\pi (n-\varepsilon_m) f_m / F_s\big) - B^m_{\lfloor (n-\varepsilon_m)/N \rfloor} \sin\big(2\pi (n-\varepsilon_m) f_m / F_s\big) \\ & + \mathbf{j} \Big(A^m_{\lfloor (n-\varepsilon_m)/N \rfloor} \sin\big(2\pi (n-\varepsilon_m) f_m / F_s\big) + B^m_{\lfloor (n-\varepsilon_m)/N \rfloor} \cos\big(2\pi (n-\varepsilon_m) f_m / F_s\big) \Big) \Big] \\ & + w_I(n/F_s) + \mathbf{j} w_Q(n/F_s), \qquad 0 \le n < N \end{aligned} \tag{5.3}$$

5.3 One-Bit Quantization for FFT-based Wideband Sensing

Here, we have modified the classical FFT-based energy detector so that the ADC is implemented through a comparator. A complete architecture for the sensing mode is considered, where the RF front end collaborates with the digital processing to implement a practical solution. Since classical FFT-based energy detector assumes reasonably high sensing period, we present a modified mathematical tool to better express the system performance irrespective to the quiet period duration. Closed form expressions for the system performance represented by the receiver operating characteristics are derived. Then, we discuss how the 1-bit quan-

tization influences these expressions by considering the power balance problem. Thus, 1-bit quantization performance with imperfect RF front end is obtained and evaluated through simulation results.

5.3.1 Proposed Spectrum Sensing Procedure

The architecture for the proposed 1-bit quantized system is shown by Figure 5.2. After the signal is received, it is processed by various RF blocks to reduce the noise, amplify the signal power, down-convert the signal to the baseband, and mitigate the introduced distortion. The processed signal is then sampled by the ultra high speed ADC. In this work, we are extremely aggressive with the ADC resolution to extremely reduce the power consumption. We deploy a 1-bit quantizer which is typically a comparator that compares the incoming sample, after the sample and hold circuit, to zero in order to retrieve the sign from the sample value. To further reduce the power consumption, it is likely for the digital processing to operate at low clock frequency. Also, the RF can be switched off once the sensing period is complete. Since only the samples that fall within the sensing period are required to be processed, a high speed buffer is employed to store one window of captured samples. Then, the digital processing is applied over the stored samples by relatively low clock frequency.

By introducing the 1-bit quantizer, the soft information about the signal power contained in the received signal disappears. Fortunately, current RF processors provide the received signal power that is measured by a received signal strength indicator (RSSI) block [116]. The measured value is reported to the digital processor through a standalone high resolution ADC that operates at relatively low sampling rate, $\bar{F}_s$. The objective is to supply the digital processor by a soft value for the power so that AGC loop complexity is significantly reduced. In this work, the RSSI is measured at the end of the sensing period and it is utilized to scale the quantized samples so that the received power is preserved. Precisely, the samples are segmented into non-overlapped captures in time where each capture has exactly N samples. During the sensing period, it is assumed that the high speed buffer can hold a complete window of samples consisting of L different captures. Each capture is processed by the FFT block to obtain the frequency spectrum over N frequency bins where each bin corresponds

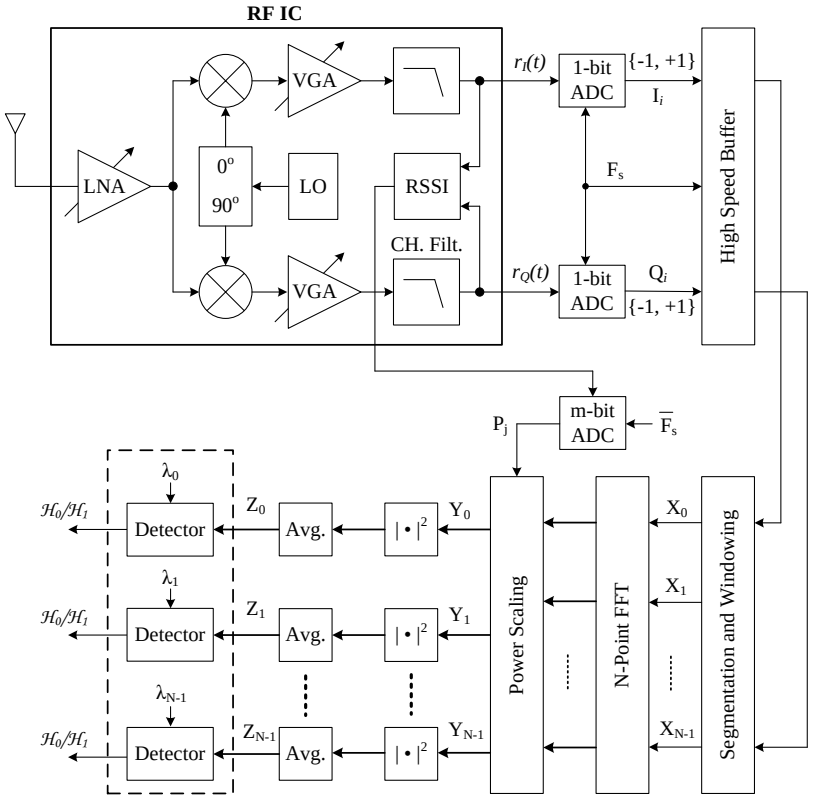

Figure 5.2: General architecture for the low power wideband sensing system

to a single sub-band. The frequency transformation can be defined by,

$$Y_{n,i} \quad = \quad \frac{P_j}{\sqrt{2N}} \sum_{k=0}^{N-1} X_{k,i}\, e^{-\mathbf{j}2\pi kn/N},\ \mathbf{j} = \sqrt{-1} \tag{5.4}$$

where $X_{k,i}$ is the quantized sample value at time index k and capture index i, P_j is the measured signal power, j is an integer representing the window index over time, and n is the sub-band index. According to our model, the measured power value corresponds to the total received power (i.e, $P_j = \mathbb{E}[\mathbf{R}\mathbf{R}^H]$). However, it is unlikely to perfectly estimate the power by the RSSI block. Therefore, we typically model an imperfect measured power to be $P_j = (1+\delta)(M\sigma_S^2 + N\sigma_W^2)$, where δ refers to the percentage of the perfect received power that models the measurement error. For each frequency bin n and window index j, the energy contained in one window consisting of L samples can be defined as given by (5.5). Hence, the decision statistic, $Z_{n,j} = T_{n,j}/L$, is defined to be a power estimator that is employed to decide whether this sub-band is a hole or not.

$$T_{n,j} \quad = \quad \sum_{k=0}^{L-1} \left| Y_{n,j\times L+k} \right|^2, \ 0 \leq j \tag{5.5}$$

5.3.2 FFT-based 1-Bit Quantization Performance

In this section, we present the classical FFT-based energy detector theory and its corresponding conventional approximated performance. Due to the quantization effect and the assumption of infinite averaging, we provide an accurate analysis for the FFT-based energy detector that can be used for practical environments. From this analysis and as a straightforward extension, we conclude the performance of the presented 1-bit quantized system. From the developed detection and false alarm probabilities, the system can be designed to achieve a predefined target performance.

5.3.2.1 Classical FFT-based Energy Detector for Wideband Sensing

Let R_k be the Discrete Fourier Transform (DFT) of the received wideband non-quantized signal at sub-band k out of N sub-bands. To decide whether the kth sub-band is occupied or not, the following binary hypotheses is tested,

$$\begin{cases} \mathcal{H}_{0,k}: \ R_k = W_k \\ \mathcal{H}_{1,k}: \ R_k = H_k S_k + W_k, \ k = 0, \ 1, \ ... \, N-1 \end{cases} \tag{5.6}$$

where $\mathcal{H}_{0,k}$ and $\mathcal{H}_{1,k}$ indicate, respectively, the absence and presence of the primary signal in the kth sub-band, W_k is the AWGN observed at the frequency domain, $H_k S_k$ is the contribution of the primary users at the kth sub-band if this sub-band is occupied. Figure 5.3 shows the general architecture for the classical energy detection technique employed for wideband sensing. In the energy-based detection algorithm, each output bin from the discrete Fourier transform block, that is typically implemented by a Fast Fourier Transform (FFT) algorithm, is utilized to compute the energy over the corresponding sub-band. For each sub-band k, the summary statistic is computed as the sum of received signal energy over an interval of L samples as given by,

$$Z_k \quad = \quad \sum_{l=1}^{L} \left| R_k(l) \right|^2 \tag{5.7}$$

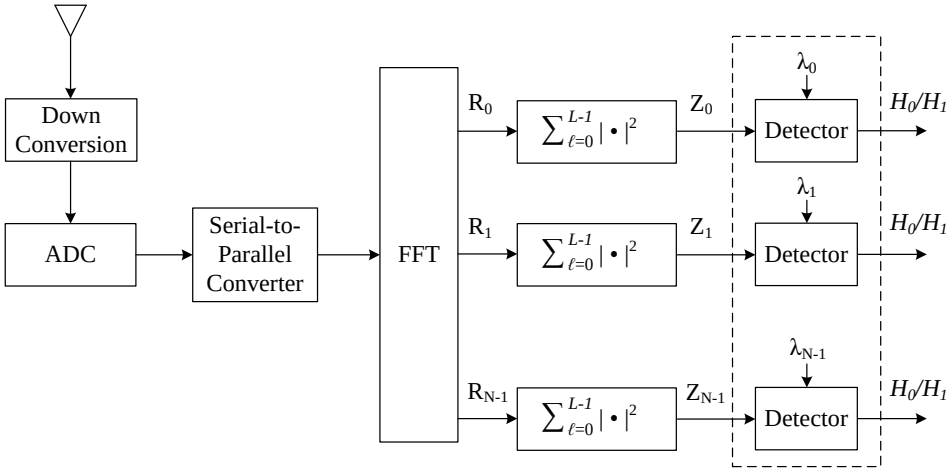

Figure 5.3: Classical energy detection for wideband sensing by employing a high speed ADC and an FFT.

The decision rule is simply given by (5.8) where λ_k is the corresponding decision threshold employed for the sub-band k.

$$\begin{cases} \mathcal{H}_{0,k}: \ Z_k < \lambda_k \\ \mathcal{H}_{1,k}: \ Z_k \geq \lambda_k \end{cases} \tag{5.8}$$

If the averaging is large enough, the decision statistic (i.e, Z_k) can be asymptotically approximated to a Normally distributed random variable [117][118]. The mean and the variance of this random variable will depend on the averaging depth, the AWGN variance, the signal to noise ratio, and the decision of the hypotheses. Let us assume that the noise has a variance of σ_W^2 and the signal to noise ratio at sub-band k is given by $\gamma_k = \mathbb{E}[|H_k S_k|^2]/\sigma_W^2$. In this case, the random variable will have the mean $\mathbb{E}[Z_k]$ and the variance $\mathrm{VAR}[Z_k]$ given by,

$$\mathbb{E}[Z_k] = \begin{cases} \mathcal{H}_{0,k}: \ L\sigma_W^2 \\ \mathcal{H}_{1,k}: \ L\sigma_W^2(1+\gamma_k) \end{cases} \tag{5.9}$$

$$\mathrm{VAR}[Z_k] = \begin{cases} \mathcal{H}_{0,k}: \ 2L\sigma_W^4 \\ \mathcal{H}_{1,k}: \ 2L\sigma_W^4(1+2\gamma_k^2) \end{cases} \tag{5.10}$$

Thus, these statistics can be written compactly as $Z_k \sim \mathcal{N}(\mathbb{E}[Z_k]), \mathrm{VAR}[Z_k])$. Based on this analysis, the detector performance can be derived in terms of the receiver operating

characteristics (ROC) that is represented by the probability of detection, P_D, and probability of false alarm, P_{FA}. The detection probability is the probability of detecting a primary signal when it is truly present. Of course, one can interpret the same meaning by referring to the probability of miss-detection which refers to the rate of miss-detecting a primary user when it truly present. The false alarm probability is the probability that the test incorrectly decides that the primary user is present when it is actually not. Since Z_k follows a Normal distribution, these quantities can be directly obtained such that,

$$P_{FA} = Prob[Z_k > \lambda_k | \mathcal{H}_{0,k}] = Q\left(\frac{\lambda_k - L\sigma_W^2}{\sigma_W^2\sqrt{2L}}\right) \tag{5.11}$$

$$P_D = Prob[Z_k > \lambda_k | \mathcal{H}_{1,k}] = Q\left(\frac{\lambda_k - L\sigma_W^2(1+\gamma_k)}{\sigma_W^2\sqrt{2L(1+2\gamma_k^2)}}\right) \tag{5.12}$$

For cognitive radio networks, the probabilities of false alarm and miss have unique implications. Low probabilities of false alarm are necessary in order to maintain possible high throughput in cognitive radio systems, since a false alarm would prevent the unused spectral segments from being accessed by cognitive radios. On the other hand, the probability of miss measures the interference from cognitive radios to the primary users, which should be limited in opportunistic spectrum access. These implications are based on a typical assumption that if primary signals are detected, the secondary users should not use the corresponding channel and that if no primary signals are detected, then the corresponding frequency band will be occupied by secondary users.

It is quite clear that this analysis miss two important features that can be summarized.

- The received input signal is assumed to have infinite precision where the ADC quantization has not taken into consideration. In real systems, the ADC resolution influences the distribution of the power after the FFT. The quantization noise has to be taken into account. In fact, the effort presented in [119] considers the quantization effect but it still assumes that the soft information about the frequency occupancy is always preserved after quantization since sequential sensing is considered and the problem is converted in a narrow-band sensing problem. In aggressive quantization strategies for non-sequential sensing approaches like the presented FFT-based energy detector, this is not the case.

- It is assumed that the averaging depth is quite high so that the decision statistic can be approximated to a Norma distribution. However, this assumption adds one more implication to the algorithm since the sensing period will be correspondingly high to accommodate for enough samples to average over. If the signal to noise ratios are reasonably high, the averaging depth can be reduced to save more time and increase the secondary network throughput. In this case, the above analysis has to be revised and a better approximation is needed to relax the assumption of having large averaging depth.

5.3.2.2 Energy Detection Performance for Non-quantized Systems

As presented in the previous section, for a large number of samples to average (e.g., $L > 40$), the central limit theorem is typically employed to approximate the probability distribution function of the decision statistic Z_n as a normal distribution under both hypothesises. The sensing time has to be quite long which results in higher power consumption. It is essential to update this mathematical tool to support any averaging length. In this section, we provide closed form expressions for the sensing performance by considering the non-quantized system.

For each sub-band, n, we wish to discriminate between the two hypotheses $\mathcal{H}_{0,n}$ and $\mathcal{H}_{1,n}$ where the first assumes that the primary signal is not in band and the second assumes that the primary user is present. Using the average energy decision statistic, one can define these hypotheses under the assumption of infinite ADC precision as given by (5.13) where it is assumed that the vacant sub-band contains noise only while the occupied sub-band includes both signal and noise.

$$\begin{cases} \mathcal{H}_{0,n}: \ Z_n \leq \lambda_n, & \sigma_Y^2 = \sigma_W^2 \\ \mathcal{H}_{1,n}: \ Z_n > \lambda_n, & \sigma_Y^2 = \sigma_S^2 + \sigma_W^2 \end{cases} \tag{5.13}$$

As the wideband sensing objective is to explore the spectral occupancy of primary signals over numerous number of sub-bands (e.g., $N \gg 100$), then the FFT output sequence follows a circularly symmetric complex Gaussian distribution by central limit theorem. Let $Y_{n,i} \sim \mathcal{CN}(0, \sigma_Y^2)$ as X_k always has a zero mean and the samples are statistically independent, the random variable T_n follows a Chi-Square distribution with L degrees of freedom [120] (i.e, $T_n \sim \chi_L^2(t\ )$). By applying a linear transformation between random variables such that

$Z_n = T_n/L$, one can obtain the PDF for the decision statistic as given by (5.14) where $f_{Z_n}(z) = L\, f_{T_n}(Lz)$ and $\sigma_Z^2 = \sigma_Y^2/L$. Consequently, the mean and variance for the power estimator can be evaluated where $\mu_Z = \mathbb{E}[Z_n] = L\sigma_Z^2 = \sigma_Y^2$ and $VAR(Z_n) = \mathbb{E}[(Z_n - \mu_Z)^2] = L\sigma_Z^4 = \sigma_Y^4/L$. Further, the cumulative distribution function can be obtained in a closed form as given by (5.15).

$$f_{Z_n}(z) = \frac{1}{\sigma_Z^{2L}\,\Gamma(L)}\, z^{L-1}\, e^{-z/\sigma_Z^2}, \quad z > 0 \tag{5.14}$$

$$\begin{aligned} F_{Z_n}(z) &= Prob[Z_n \le z] = \int_{-\infty}^{z} f_{Z_n}(t)\,\mathrm{d}t = 1 - \int_{z}^{\infty} f_Z(t)\,\mathrm{d}t \\ &= 1 - \frac{1}{\Gamma(L)} \int_z^{\infty} \left(\frac{t}{\sigma_Z^2}\right)^{L-1} e^{-t/\sigma_Z^2}\, \frac{\mathrm{d}t}{\sigma_Z^2} \mathrm{d}t = 1 - \frac{1}{\Gamma(L)} \int_{z/\sigma_Z^2}^{\infty} \acute{t}^{L-1}\, e^{-\acute{t}}\, \mathrm{d}\acute{t} \\ &= 1 - \frac{\Gamma\big(L, z/\sigma_Z^2\big)}{\Gamma(L)} = 1 - \sum_{k=0}^{L-1} \frac{1}{k!} \left(\frac{z}{\sigma_Z^2}\right)^k e^{-z/\sigma_Z^2} \end{aligned} \tag{5.15}$$

The performance of the detector is quantified in terms of its ROC curve, which represents the probability of detection, P_D, as a function of the probability of false alarm, P_{FA}. By varying a certain threshold λ_n for each sub-band n, the operating point of a detector can be chosen anywhere along the ROC curve. P_{FA} and P_D can be defined as given by (5.16) and (5.17), respectively.

$$\begin{aligned} P_{FA} &= Prob\big[Z_n > \lambda_n \,|\, \mathcal{H}_0\big] = 1 - F_{Z_n|\mathcal{H}_{0,n}}(\lambda_n) \\ &= \sum_{k=0}^{L-1} \frac{1}{k!} \left(\frac{\lambda_n L}{\sigma_W^2}\right)^k e^{-\lambda_n L/\sigma_W^2} \end{aligned} \tag{5.16}$$

$$\begin{aligned} P_D &= Prob\big[Z_n > \lambda_n \,|\, \mathcal{H}_1\big] = 1 - F_{Z_n|\mathcal{H}_{1,n}}(\lambda_n) \\ &= \sum_{k=0}^{L-1} \frac{1}{k!} \left(\frac{\lambda_n L}{\sigma_W^2 + \sigma_S^2}\right)^k e^{-\lambda_n L/(\sigma_W^2+\sigma_S^2)} \end{aligned} \tag{5.17}$$

In classical statistics framework known as Neyman-Pearson (NP) criterion [121], either $\mathcal{H}_{0,n}$ or $\mathcal{H}_{1,n}$ is deterministically true, and the objective is to maximize P_D subject to a constraint on P_{FA}. Therefore, one can obtain the threshold λ_n subjected to a constant P_{FA}. This step requires linear programming to be applied to (4.4), then the detection probability cab be evaluated by substituting in (4.3).

5.3.2.3 Energy Detection Performance for the 1-bit quantized System

In conventional systems that consider the quantization effect [119], the effect is modelled by adding one more term to the signal variance representing the quantization noise power which is a function of the ADC resolution. Unfortunately, this procedure cannot be applied for the 1-bit quantizer case since the ADC aggressively saturates the incoming signal to two possible outcomes $\{-1, +1\}$ that are uniformly distributed.

By introducing the power scaling operation after the FFT module under perfect power measurement (i.e, $\delta = 0$), a total power transfer is guaranteed to the frequency domain since the defined transform itself is linear and unitary. However, the main objective of the transformation is to reshape the power across various sub-bands. If the input is left un-quantized, the information required for this redistribution process is known in full and the detection error is only introduced due to the noisy environment. When the input is quantized to a single bit and no power gain or loss is guaranteed, then simply the quantization effect can be interpreted as a power leakage process due to the reduced amount of information about the power distribution.

In reality, the 1-bit quantization influences the power balance for various sub-bands. Since the overall system performance gets degraded, it is expected that the power of the allocated sub-bands is reduced while the noise level of the unoccupied sub-bands is increased. It is understood that an occupied sub-band leaks more power for its adjacent sub-bands when compared to other neighbours that are located far away. However, the number of occupied sub-bands is large enough and is uniformly distributed across the whole band. Therefore, the leakage contribution from various PUs at any bin can still be modelled as a Gaussian signal by central limit theorem. This can be illustrated as shown in Figure 5.4.

To derive the amount of this leaked power, let us assume $\alpha M \sigma_S^2$ be the amount of total leakage power from all occupied sub-bands, where α is a constant. As the occupied sub-bands spread randomly across the entire band, the leakage will also be distributed across all sub-bands (i.e, N bins) in an unbiased distribution process. Due to this leakage, the amount of interfering power to any bin is $\alpha M \sigma_S^2 / N$. Therefore, the power contained by one sub-band under $\mathcal{H}_{0,n}$ would be $\sigma_0^2 = \sigma_W^2(1 + \alpha\gamma M/N)$ instead of just σ_W^2 in a non-quantized system,

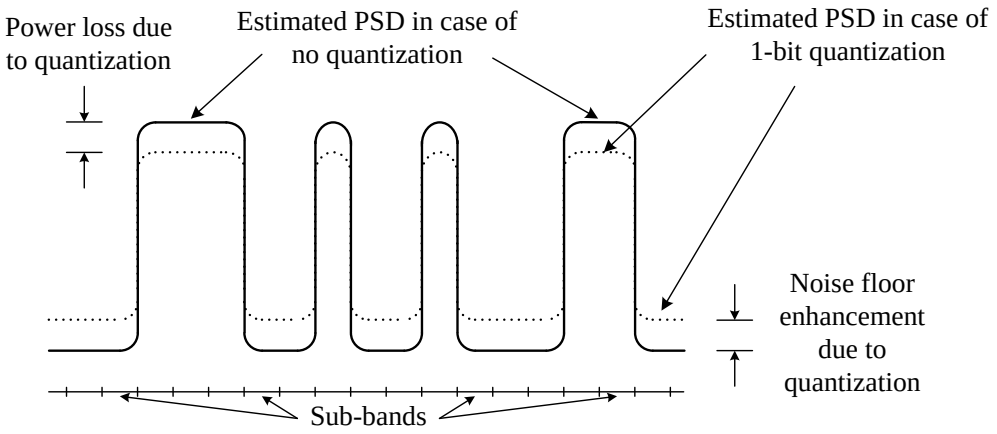

Figure 5.4: Illustration for the 1-bit quantization effect on the estimated power spectral density

where $\gamma = \sigma_S^2/\sigma_W^2$ is the SNR over one sub-band. On the other hand, the occupied sub-bands that have already paid $\alpha M\gamma\sigma_W^2$ of its total power will gain portion of this power due to the fair distribution process. Thus, one can write the power contained in one occupied sub-band as $\sigma_1^2 = \sigma_W^2(1 + \gamma - \gamma\alpha + \alpha\gamma M/N)$ instead of just $\sigma_W^2(1 + \gamma)$, where $-\gamma\alpha$ represents the contribution of this sub-band in the total leakage power. In this work, we rely on extensive computer simulations by varying σ_W^2, σ_S^2, M, L, and N to find an optimum estimate for this constant which is found to be $\alpha = 0.3675 \simeq e^{-1}$.

It is worth to study the effect of the imperfect power measurement on the system performance. The FFT output samples are scaled so that the total power fits the measured power provided by the RSSI block. In this case, the power contained by one sub-band will be adjusted according to whether this sub-band is occupied or not. Based on the previous discussion, if the sub-band is signal free, the sub-band power under $\mathcal{H}_{0,n}$ will be $\widetilde{\sigma}_0^2 = (1+\delta)\sigma_W^2(1+\alpha\gamma M/N)$. On the other hand, if the sub-band includes signal plus noise, the sub-band power under $\mathcal{H}_{1,n}$ will be $\widetilde{\sigma}_1^2 = (1+\delta)\sigma_W^2(1+\gamma-\gamma\alpha+\alpha\gamma M/N)$. As a result, the closed-form expressions for the false alarm and detection probabilities in case of 1-bit quantizer system with imperfect power measurements can be obtained by,

$$P_{FA}\Big|_{1-\text{bit}} = \sum_{k=0}^{L-1} \frac{1}{k!} \left(\frac{\lambda_n L}{\widetilde{\sigma}_0^2} \right)^k e^{-\lambda_n L/\widetilde{\sigma}_0^2} \tag{5.18}$$

$$P_{D}\Big|_{1-\text{bit}} = \sum_{k=0}^{L-1} \frac{1}{k!} \left(\frac{\lambda_n L}{\widetilde{\sigma}_1^2} \right)^k e^{-\lambda_n L/\widetilde{\sigma}_1^2} \tag{5.19}$$

5.3.3 Simulation Results

In the simulation, we consider a wideband system that employs a total band of 1.024GHz that is divided into $N = 1024$ non-overlapped sub-bands, M of which are occupied by primary signals that uniformly spread over the entire band. Each of those allocated sub-bands carries QAM signal that is passed over a multipath channel filter such that the received signal is CSCG with a normalized power level (without loss of generality, $\sigma_S^2 = 1$). The signal is then up-converted to the desired carrier. The channel is randomly generated every processing window. However, the filter taps are always scaled to fit an exponential power delay profile (PDP) [122]. A Gaussian white noise is added to the sum of the up-converted primary signals such that its power spectral density is $1/\gamma$. To simulate the system behaviour, 10^5 trials are processed and the system performance is evaluated based on the decision outcomes. In each trial, a single window containing NL samples is generated where the sub-band occupancies are never changed within a single window. The signs of the received samples are captured to be processed by the detector. The detection performance is taken based on the miss-detection of the occupied sub-bands while the false alarm decisions are considered over the detected vacant sub-bands.

First, the approximated ROC proposed by [114] is compared to our exact closed form ROC performance under different SNR values and for relatively high averaging rate (e.g, $L = 8$). The performance curves are shown in Figure 5.5. It is clear that the Normal approximation introduces considerably large errors in performance even for relatively high averaging rate. The exact expressions are a must to accurately and reliably evaluate the system performance especially for critical systems in which a small performance degradation is accepted to relax other implementation aspects. The simulation results for the non-quantized system are also shown to demonstrate the accuracy of our derivations. Furthermore, Figure 5.5 shows the

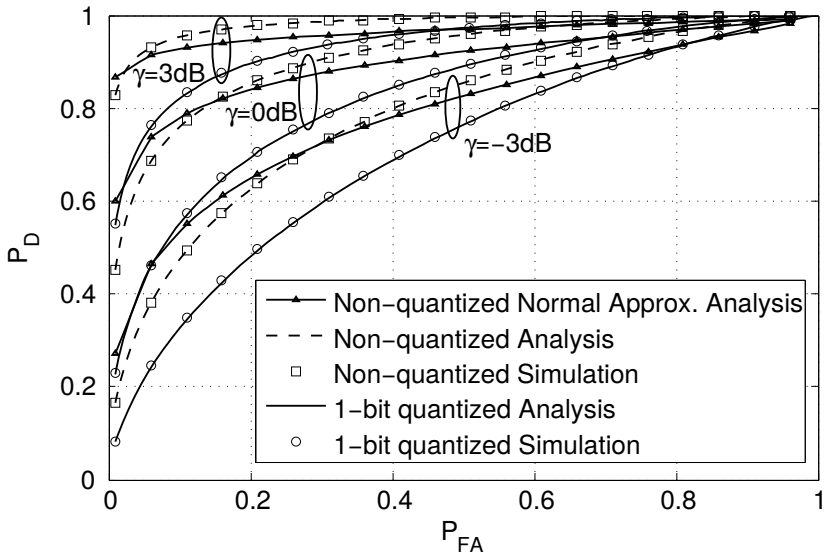

Figure 5.5: ROC comparison among the non-quantized analysis, the corresponding approximated analysis [114], the non-quantized simulations, 1-bit quantized system at different SNR values for $L = 8$, $M = 100$, and $\delta = 0$

ROC for the 1-bit quantizer and the non-quantized systems. We emphasize the fact that the simulations exactly match the analysis for the 1-bit quantizer case for various SNR cases and for a different averaging rate $L = 8$ than the one used in Figure 5.6.

Next, extensive simulations are performed to verify the constant value $\alpha \simeq e^{-1}$. In these results, more than 100 false alarm rates are simulated. Different SNR values and different averaging depths are considered. Figure 5.6 shows the exact match of the performance between the simulation and the analysis for all possible spectrum utilization ratios (percentage of the occupied bands) and for different false alarm rates. Although these results assume fixed values for other parameters such as $L = 4$ and SNR=0dB, we rely on other results (in Fig. 5.5 and Figure 5.7) to demonstrate the confidence and the effectiveness of our selected constant value.

In Figure 5.7, we show the effect of the quantization effect when compared to the non-quantized system. It is clear that a degradation of about 2dB is observed between the non-quantized system and the 1-bit quantized system. Moreover, it is obvious that the averaging depth significantly influence the performance. In fact, increasing the averaging depth improves the detection rate. However, increasing the averaging depth requires longer

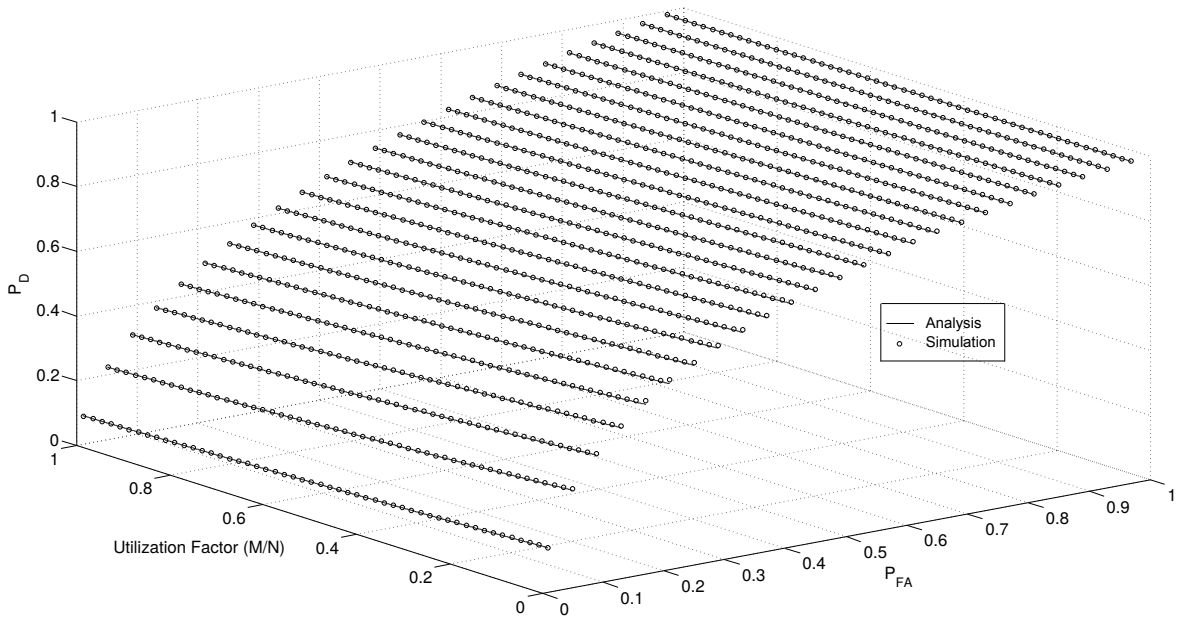

Figure 5.6: Detection performance for the one bit quantizer versus the spectrum utilization at $\gamma = 0$dB, $L = 4$, and $\delta = 0$

sensing intervals which typically reduces the overall secondary network throughput.

Figure 5.8 introduces the imperfect power measurement to compare the detector performance based on the closed form expressions and the performance obtained by simulations. The threshold, λ_n, has been evaluated at $\delta = 0$. At a fixed threshold value, it is clear that increasing the tolerance presents higher degradation for the false alarm on the account of a corresponding enhancement for the detection rate. Therefore, it is better to select an RF IC that provides an accurate power measurements with reasonable complexity and power budget.

5.4 One-Bit Quantization for Autocorrelation-based Wideband Sensing

In this section, we present the second wideband spectrum sensing system in which a 1-bit ADC is employed. The technique best fits with the sparse systems in which few sub-bands are utilized. To support this proposal, a complete architecture for the sensing engine is presented. A practical window-based autocorrelation based processing followed by a DFT

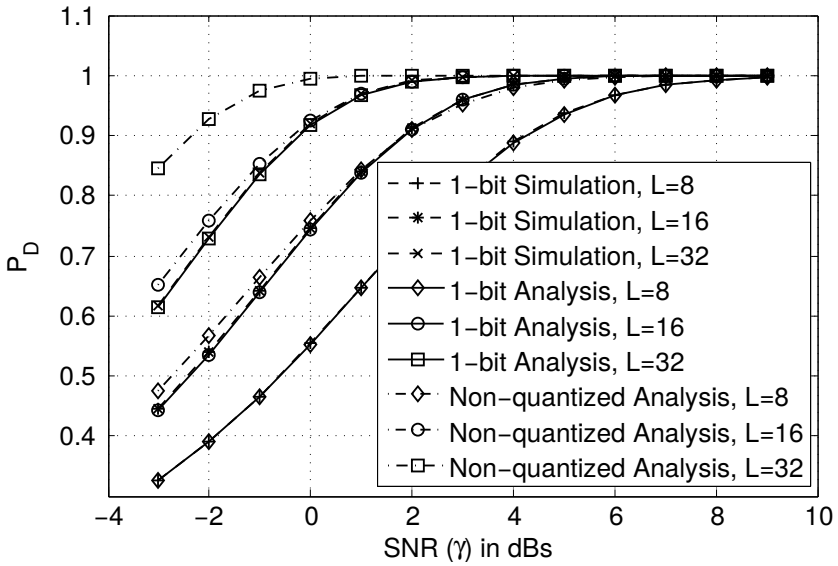

Figure 5.7: Detection probability for the non-quantized exact analysis, the 1-bit quantized analysis, and the 1-bit quantized simulation for different time average values for $P_{FA} = 0.1$, $M = 100$, and $\delta = 0$

block is employed to estimate the power spectral density of the wideband spectrum. The basic idea is that a low baud rate signal representing the PU signal is extensively sampled by an ultra high sampling rate which makes it possible for an autocorrelation to identify if a specific carrier frequency is in use or not. The aggressive quantization effect is fully analysed to provide closed form expressions for the correlation output. A detection algorithm is designed, verified, and simulated to provide the detector performance in terms of ROC curve that determines both a false alarm probability and a detection probability for a given set of the system parameters.

5.4.1 Proposed Spectrum Sensing Procedure

The architecture for the proposed 1-bit quantized system is shown by Fig. 5.9. After the signal is received, it is processed by various RF blocks to reduce the noise, amplify the signal power, down-convert the signal to the baseband, and mitigate the introduced distortion. The processed signal is then sampled by the ultra high speed ADC. To significantly reduce the power consumption, a special system architecture is designed, analysed, and verified. In this

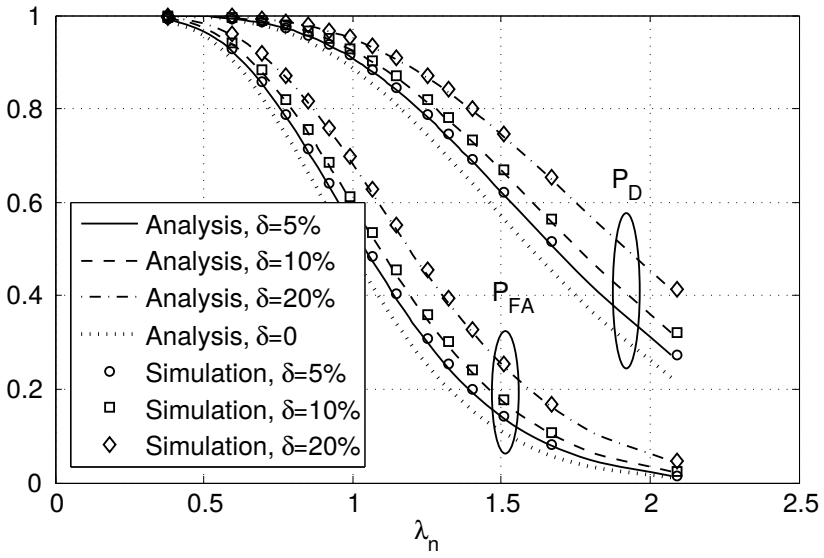

Figure 5.8: False alarm and detection probabilities for various tolerance values (δ =5%, 10%, or 20%) for $L = 8$, $M = 100$, γ=0dB, and $\sigma_W^2 = 1$.

work, we are extremely aggressive with the ADC resolution to come to the bottom line of the power consumption provided by the ADC given a unique sampling rate. We consider a wideband sensing system in which a 1-bit ADC is used for each inphase and quadrature baseband received signal. For 1-bit quantization, binary antipodal signaling was found to be optimal [123]. Therefore, for a Single-Input Single-Output system, the quantized received samples belong to the set $\{1 + \mathbf{j},\ 1 - \mathbf{j},\ -1 + \mathbf{j},\ -1 - \mathbf{j}\}$. It was also shown that in the low SNR regime, the use of low-resolution ADCs incurs a surprisingly small loss in spectral efficiency compared to unquantized observations [124]. It is worth to mention that the typical RF chip usually employs Voltage Gain Amplification stages along with AGC, however, these blocks are not utilized for 1-bit quantizer systems. Therefore, these blocks are deactivated in Fig. 5.9. The reason is that a 1-bit quantizer is typically implemented as a comparator that compares the incoming sample, after the sample and hold circuit, to zero in order to retrieve the sign from the sample value.

To further reduce the power consumption, it is likely for the digital processing to operate at low clock frequency. Also, the RF can be switched off once the sensing period is complete. Since only the samples that fall within the sensing period are required to be processed, a high speed buffer is employed to store one window of captured samples. Then, the digital

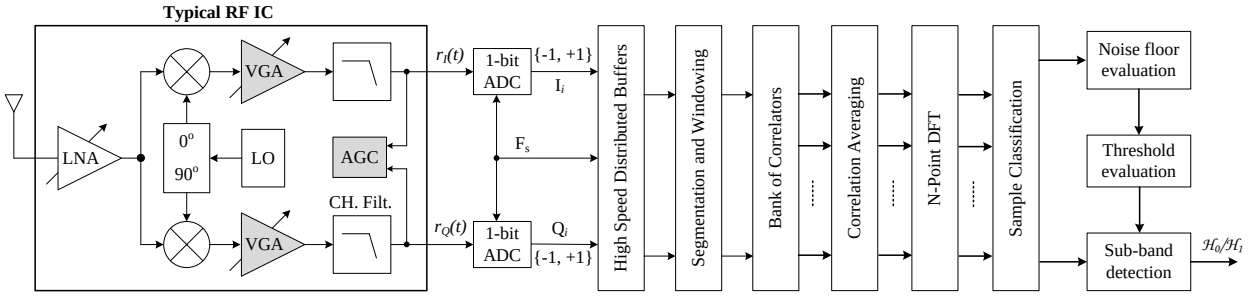

Figure 5.9: System architecture for the correlation based 1-bit quantizer system

processing is applied over the stored samples by relatively low clock rate. The samples are segmented into non-overlapped captures in time where each capture has exactly N samples. During the sensing period, it is assumed that the high speed buffer can hold a complete window of samples consisting of L different captures. Therefore, the buffer size will precisely contain LN samples. By introducing the 1-bit quantizer, the soft information about the signal power contained in the received signal disappears. Fortunately, the quantized signal still has partial information about the spectrum occupancy. To retrieve the power spectral density of the received random signal, each capture is processed by a bank of correlators to obtain a window-based autocorrelation of the received sequence. An averaging process over L consecutive correlations is applied to reduce the effect of the noise over the correlation. Let us define the window based correlation after averaging to be,

$$R(k) \;=\; \frac{1}{L}\sum_{i=0}^{L-1}\left[\frac{1}{N-k}\sum_{n=0}^{N-k-1} r_q^*(n,i)r_q(n+k,i)\right] \tag{5.20}$$

where i is the capture index, k is the time index for the averaged autocorrelation, $r_q(n,i)$ is the complex received sample value after quantization at time index n such that $0 \leq i < L$ and $0 \leq k < N$, and $R(k)$ is the averaged autocorrelation function. To obtain the PSD, the averaged correlation is converted to the frequency domain through a discrete Fourier transform (that could be implemented through an FFT block if N is properly chosen). The DFT size is exactly N such that each bin corresponds to a single sub-band. To evaluate the power spectral density at sub-band m, the absolute value of the normalized frequency transformation can be defined by,

$$S(m) \;=\; \frac{1}{N}\left|\sum_{k=0}^{N-1} R(k)\, e^{-\mathbf{j}2\pi km/N}\right|,\; 0 \leq m < N \tag{5.21}$$

Based on the obtained PSD, the noise floor can be estimated by averaging the bins that lie within a predefined noise region. The methodology to choose those bins is that the PSD value for a selected sub-band has to be close to, *within a predefined tolerance*, the minimum possible PSD value. Since the spectrum is typically sparse, the PSD values within the noise region will interpret two quantities. First, it includes the noise power introduced to the system. This will be an accurate estimate for the noise level if enough averaging has been considered while the autocorrelation is being evaluated. However, this averaging has to be also carefully designed because more averaging means not only improved PSD evaluation, but also it impacts the system by introducing more sensing time and more buffer storage. The second item that is inferred from the minimum power values is the interference induced from the occupied sub-bands at the desired bin. It is understood that an occupied sub-band leaks more power to its adjacent sub-bands when compared to other neighbours that are located far away. However, the number of occupied sub-bands is small enough and is uniformly distributed across the whole band (if sparsity assumption holds). Thus, the interference contribution from various PUs at any bin can still be insignificant if the band is extremely large (i.e., $N \gg 500$). A noise plus interference power can be estimated and used to develop a threshold by which the detection procedure classifies the individual sub-bands to be either vacant or occupied. More details about this detection algorithm will be discussed in Section 5.4.3.

5.4.2 Statistical Autocorrelation and PSD Functions for One-Bit Quantizer System

From the basic concepts, the statistical window-based autocorrelation, $\mathcal{R}(k)$, for the 1-bit quantized system is derived in closed form expression as given by (5.22), where $\eta_k = \frac{1}{M}\left(1 - k/N\right)\sum_{m=1}^{M}\gamma_m \cos\left(2\pi f_m k/F_s\right)$, $\zeta_k = \frac{1}{M}\left(1 - k/N\right)\sum_{m=1}^{M}\gamma_m \sin\left(2\pi f_m k/F_s\right)$, $\bar{\gamma} = \frac{1}{M}\sum_{m=1}^{M}\gamma_m$ is the average primary signal to noise ratio, γ_m is the signal to noise ratio for the occupied sub-band m, $\beta = M/N$ is the utilization factor (see Appendix A). The power spectral density for the 1-bit quantized system can be obtained by taking the Fourier transform of the closed form expression for the window-based autocorrelation function. Precisely, the continuous-frequency PSD is given by $\mathcal{S}(f) = \sum_{k=0}^{N-1}\mathcal{R}(k)e^{-\mathrm{j}2\pi kf/F_s}$ where $0 \leq f < F_s$.

In fact, it is not easy to derive a closed form expression for the power spectral density in this case due to the existence of the arcsine function which is non-linear. However, one still needs to understand the effect of quantization on the spectral density which is the key element in the sensing algorithm. The arcsine function can be approximated to only the first term of its Taylor expansion (a unity slope ramp function) if the operand value is quite small (i.e., $\sin^{-1}(x) = x$ for $|x| \leq 0.2$). Using simple computer simulation, one can evaluate the mean square error of the approximated arcsine and the exact one to be in the order of 3×10^{-7}. For the arcsine approximation to be valid given that $|\zeta_k| \leq \bar{\gamma}$, there will be a restriction on the product $\beta\bar{\gamma}$ such that $\left|\beta\zeta_k/(1+\bar{\gamma}\beta)\right| \leq 0.2$. To jointly satisfy both conditions, we should have $4\bar{\gamma}\beta \leq 1$. In this case, the approximated correlation function can be written as given by (5.23) where $u(k)$ is the typical unit-step function. The corresponding approximated PSD is given by (5.24).

$$\mathcal{R}(k) = \frac{4}{\pi}\left[\sin^{-1}\left(\frac{\delta(k)+\beta\eta_k}{1+\bar{\gamma}\beta}\right) + \mathbf{j}\sin^{-1}\left(\frac{\beta\zeta_k}{1+\bar{\gamma}\beta}\right)\right] \tag{5.22}$$

$$\widetilde{\mathcal{R}}(k) = 2\delta(k) + \frac{4}{M\pi}\frac{\beta}{1+\bar{\gamma}\beta}\left[\left(1-\frac{k}{N}\right)\sum_{m=1}^{M}\gamma_m e^{\mathbf{j}2\pi k f_m/F_s}\right]u(k-1), \bar{\gamma}\beta \leq \frac{1}{4} \tag{5.23}$$

$$\widetilde{\mathcal{S}}(f) = 2 + \frac{4}{M\pi}\frac{\beta}{1+\bar{\gamma}\beta}\sum_{m=1}^{M}\gamma_m\left[\sum_{k=1}^{N-1}e^{-\mathbf{j}2\pi k(f-f_m)/F_s} - \frac{1}{N}\sum_{k=1}^{N-1}ke^{-\mathbf{j}2\pi k(f-f_m)/F_s}\right] \tag{5.24}$$

The approximated power spectral density includes three terms that respectively correspond to the ones provided by the autocorrelation expression: (1) A white noise term represented by the constant value. (2) Impulse train (or equivalently sinc-shaped pulses in the discrete frequency domain) spread exactly at the occupied sub-bands. The impulses are scaled based on the spectrum utilization and the signal-to-noise-ratio. (3) An interference term from every occupied sub-band to the whole spectrum. This term comes from differentiating the impulse train located at the used carriers. If an impulse function (or the equivalent sinc-shaped pulses) is modelled by a narrow triangle function, then its derivative will impact the close neighbours by introducing higher interference power when compared to far sub-bands.

By taking the absolute value of $\widetilde{\mathcal{S}}(f)$, it is straightforward to show that the function has local maxima at the occupied frequencies. We can start by the Triangle inequality which states that $||\mathbf{x}+\mathbf{y}|| \leq ||\mathbf{y}|| + ||\mathbf{y}||$ for arbitrary vectors $\mathbf{x}$ and $\mathbf{y}$ lying in the same plane where $||\bullet||$ is the usual norm operator. It is clear that the local maxima for $|\widetilde{\mathcal{S}}(f)|$ are the same local maxima for $\mathcal{E}(f) = \left|\sum_{m=1}^{M} \gamma_m \sum_{k=1}^{N-1}(1-k/N)e^{-\mathbf{j}2\pi k(f-f_m)/F_s}\right|$ since the first vector of the Triangle inequality is a constant numeric. Some of those local maxima for $\mathcal{E}(f)$ are obtained at $f = f_m \ \forall m$. However, the function $\mathcal{E}(f)$ exhibits other small local maxima representing the side-lopes of the sinc-shapes. Based on this discussion, it is quite clear that the PSD of the window-based autocorrelation for the quantized system fully reflects the spectrum occupancy and hence occupied sub-bands can be effectively sensed by utilizing this approach.

Typically, the quality of the detector is measured in terms of the detection probability as well as the false alarm probability. The detection probability is the probability of detecting a primary signal when it is truly present while the false alarm probability is the probability that the test incorrectly decides that the primary user is present when it is actually not. In classical detector design, the decision statistic formulation is helpful to maximize the detection rate, to minimize the false alarm, or generally to optimize the detector performance as a function of some cost function based on the decision statistic variable. It has been shown that searching for local maxima in $|\widetilde{\mathcal{S}}(f)|$ is not an optimum solution that maximizes the detection rate. Let us define the detection probability as $P_D = \Pr\left[|\widetilde{\mathcal{S}}(f)| > \Lambda | f = f_m \forall m\right]$ where Λ is a threshold and $|\widetilde{\mathcal{S}}(f)|$ is the absolute value of the PSD at an arbitrary frequency f.

The main issue of maximizing this detection rate is that it really depends on the knowledge of the unknown spectrum parameters such as the number of occupied bands M and the spacing between the occupied sub-bands which defines the amount of interference. Recall that the amount of interference increases by increasing the number of occupied bands, therefore the optimum threshold would absorb this fact by being a function of the occupied bands parameters. Furthermore, although this approximation provides enough confidence about the effectiveness of the proposed approach to detected PUs in the framework of a 1-bit quantizer, it is unlikely to have $4\bar{\gamma}\beta \leq 1$ especially when the sparsity level increases even at low signal-to-noise ratios. Actually, violating this condition means that non-linear terms

will be introduced to the arcsine approximation. Those non-linear terms represent more harmonics from each occupied band to be introduced as interference to the whole spectrum. Since the number of non-linear terms are infinite and the occupied sub-bands spread randomly across the wideband, the interference contribution from various occupied sub-bands at a specific carrier can be modelled as a Gaussian noise by utilizing the central limit theorem. The noise power depends on the amount of leakage arises from the occupied sub-band in a form of interference. In fact, this noise power is added to the known white noise power and hence; the noise floor of the system varies depending on the spectrum utilization and the SNR. This makes it even hard to blindly optimize any cost function to obtain an optimum performance measure. Due to the mentioned reasons, we propose a sub-optimal detection algorithm that enables the 1-bit correlation-based wideband sensing.

5.4.3 Detection Algorithm

In this section, we discuss the detection algorithm that utilizes the computed power spectral density to individually differentiate between occupied and vacant sub-bands in case of window-based correlation for the 1-bit quantized system being utilized. To design a good detection algorithm, important factors have to be taken into consideration: (1) The background system noise is magnified by introducing the interference from the occupied sub-bands. Since the spectrum utilization factor is unknown, the noise plus interference power is random. (2) The algorithm has to take the practical implementation into consideration. For example, it is impossible to average infinite number of correlations to reject the effect of independent random variables and the noise samples. (3) The algorithm should consider the complexity, the reduced sensing time, and of course the high performance by achieving the highest possible detection rate at very low false alarm rate.

Since the noise level varies with the spectrum utilization which is typically unknown, practical and reliable implementation of the proposed technique requires that the detection algorithm is able to estimate the noise floor introduced to the system for a given sensing interval. Based on the discussion presented in section 5.4.2, the PSD has enough information about the noise-plus-interference power since the sub-bands, that would have the smallest power values, mainly express the unoccupied sub-bands. Therefore, a noise-plus-interference

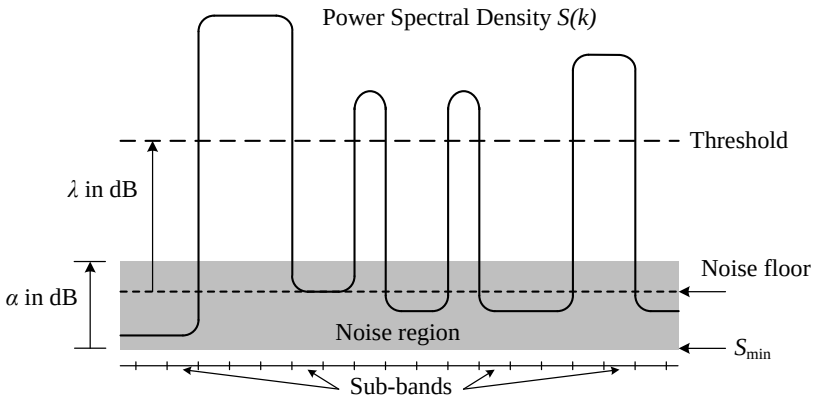

Figure 5.10: Illustration for the detection algorithm and parameter definitions for the correlation-based 1-bit quantized systems

power estimate, $\widetilde{\sigma}_W^2$, can be obtained by averaging the power of the sub-bands that have been classified to be in the noise region. The noise region is defined by introducing a tolerance above the minimum power level found in band. If the minimum power level is defined by $S_{\min}$, then an upper bound for the noise region will be $\alpha S_{\min}$ where α is a system parameter that defines the amount of tolerance. One interesting point of this approach is that α can be designed to satisfy certain false alarm rate for a given SNR and spectrum utilization.

To decide whether a sub-band is vacant or occupied, a binary hypothesis is formed based on the power spectral density of this sub-band. In fact, the value of the power spectral density at a given sub-band is compared to a threshold. If the value of the power level exceeds the threshold, this sub-band will be marked as occupied. Otherwise, the sub-band is assumed to be vacant. The threshold in this algorithm is defined to be a relative threshold to the noise floor. Thus, it mainly represents how much power is required above the noise floor to mark a sub-band as occupied. Once the noise floor (noise-plus-interference estimate) is found, the threshold value is defined to be λ dBs above the noise floor. Motivated by the classical framework of a detector design or the Neyman-Pearson (NP) criterion [39], the value of λ is optimized (through simulations) to provide the maximum detection rate for a given false alarm rate. The definitions for various parameters that are involved in detection algorithm are illustrated in Fig. 5.10. Furthermore, the detection algorithm is listed in Fig. 5.11 where the procedure of evaluating the noise floor and classifying the sub-bands as occupied or not is fully described. Recall that the only input to this algorithm is the computed power spectral

1: Evaluate the normalized Power spectral Density, $S(k)$
2: Search for the minimum PSD value, $S_{\min}$
3: Initialize: Temp=0 and Counter=0
4: **for** $k = 1 : N$ **do**
5: **if** $S_{\min} \leq S(k) < \alpha S_{\min}$ **then**
6: Temp=Temp+$S(k)$
7: Counter=Counter+1
8: **end if**
9: **end for**
10: Evaluate the noise floor: $\widetilde{\sigma}_W^2$=Temp/Counter
11: **for** $k = 1 : N$ **do**
12: **if** $S(k) \geq \lambda \widetilde{\sigma}_W^2$ **then**
13: Set the flag for sub-band k (mark it as occupied)
14: **else**
15: Clear the flag for sub-band k (mark it as a hole)
16: **end if**
17: **end for**
18: Report all flags for various sub-bands

Figure 5.11: Detection algorithm for the correlation-based 1-bit quantized systems

density, $S(k)$, defined by (5.21) where each bin represents a sub-band.

5.4.4 Simulation Results

The same simulation settings utilized by Section 5.3.3 have been inherited to this simulation as well. Thus, the signal to noise ratio per sub-band $\gamma_m = \gamma$. The false alarm probability is investigated for various system parameters. In fact, the false alarm rate depends mainly on the selected threshold, the accuracy of the noise floor, the spectrum utilization, and the SNR. As a first step towards the detector design problem, the noise tolerance, α, and the threshold are selected jointly to set the false alarm rate at a given SNR and spectrum utilization. Fig. 5.12 shows the simulation results for the false alarm probability as a function of both

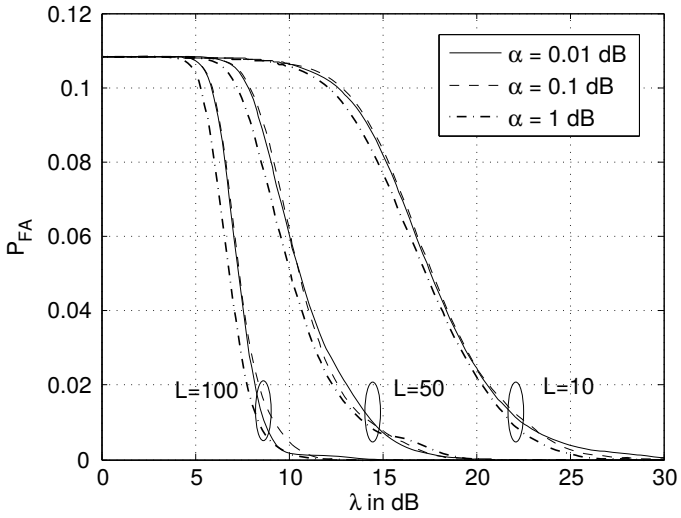

Figure 5.12: False alarm probability versus threshold under different tolerance values α =0.01, 0.1, or 1 dB and different averaging depths L =10, 50, or 100. Fixed spectrum utilization and signal to noise ratio are utilized such that β=100/1024 and γ=-3 dB

the relative threshold, λ, and the noise tolerance, α. One of the fundamental parameters that would influence the threshold value is the amount of averaging introduced to the window-based correlation. The more averaging we apply, the smoother the noise region we obtain. Therefore, less relative threshold can be employed to produce the same false alarm rate. However, a compromise between the sensing period and the smooth noise region applies.

Since the sensing period is directly proportional to the averaging depth (simply, the sensing period is LN/F_s), the averaging depth should have an upper bound to limit the sensing period and to achieve reasonable smooth power spectral density. Motivated by Fig. 5.12, it is worth to mention that the noise estimation quality is reflected in the false alarm rate for a given averaging depth. If reasonable averaging is applied, the impact of the noise estimation is minimized. For the rest of the simulations, we have limited the averaging to be over 100 correlations. In this case, the sensing period is as low as 10μsec for a wide band of 1GHz and as high as 1000 sub-bands. Therefore, $L = 100$ is a reasonable choice that provides enough smoothing and low sensing duration. It is clear from Fig. 5.12 that the tolerance value importance reduces with the increase of the averaging limit.

It can be understood that the utilization factor significantly affects the detector performance due to two reasons: (1) increasing M would increase the interference introduced from

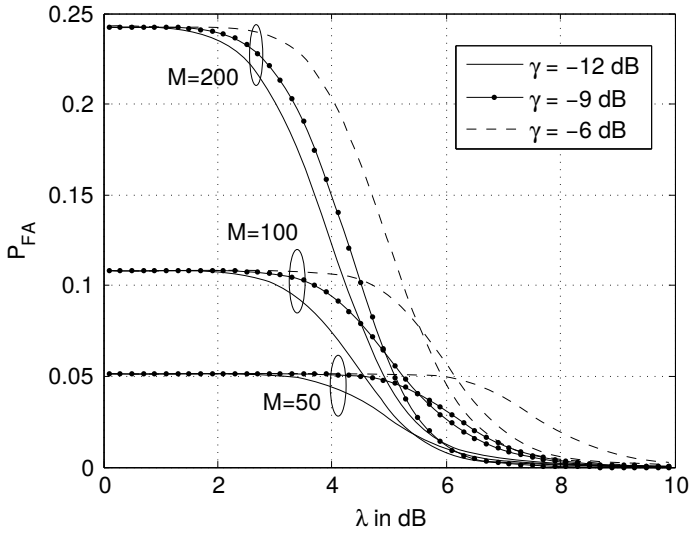

Figure 5.13: False alarm probability versus threshold under different utilization factors β =50/1024, 100/1024, or 200/1024 and different signal to noise ratios γ=-12, -9, or -6 dB. Fixed averaging depth and tolerance values are assumed such that L =100 and α=0.1 dB

the occupied sub-bands to the vacant bands and thus influence the false alarms. (2) It is quite obvious from (5.23) that the second term has a division by M. Therefore, it is expected that increasing M reduces the values of the impulses located at the occupied carriers in the power spectral density. This results in less detection for the occupied sub-bands even at very high SNR values. Fig. 5.13 shows the false alarm probability versus the relative threshold values for various utilization factors and SNRs. It can be seen that the upper bound on the false alarm rate is controlled through the utilization factor due to the fact that more occupied sub-bands introduce more interference spikes that increase the false alarms. On the other hand, the SNR mainly affect the selected threshold to achieve a fixed false alarm rate at a given spectrum utilization. The reason is that very high noise power requires infinite averaging so that smooth noise region is obtained. In this case, the relative threshold will require fine adjustments to achieve the same false alarm rate at a given spectrum utilization. It is worth to mention that FCC revealed that the radio spectrum utilization in the band below 3 GHz varies vastly where occupancy is found to be around from 15% [125]. Motivated by this practical percentage, we have utilized an occupancy range 5% to 30%.

A typical detector design starts by choosing the detector parameters to fix the false alarm

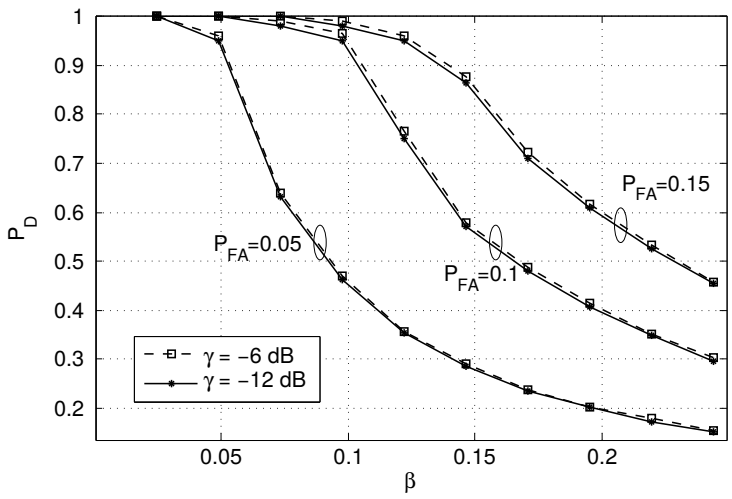

Figure 5.14: Detection probability versus spectrum utilization factor under different signal to noise ratios γ=-12 or -6 dB and different false alarm rates P_{FA}=0.05, 0.1, or 0.15. Fixed averaging depth and tolerance values are assumed such that L =100 and α=0.1 dB

rate. The corresponding detection rate is then obtained to fully characterize the detector performance through the ROC. It is worth to study the effect of various system parameters on the detection rate for given false alarms to be able to fully define the performance of the detector. Fig. 5.14 shows the effect of the utilization factor on the detection rate for given false alarm rates and SNRs. To develop these results, the simulations are adjusted first to find the threshold value at which the required false alarm rate is achieved for given spectrum utilization and SNR. Then, this threshold is used to measure the detection rate for the same system parameters. As discussed before, more utilized spectrum reduces the detection accuracy due to the impact on the impulse values at the occupied sub-bands in the power spectral density. It is clear that the detection rates are very close for various SNRs since the proper threshold is chosen to achieve a fixed false alarm rate.

In the FFT-based sequential sensing approach [119], the ultra wideband is divided into non-overlapping narrow bands. These narrow bands are sensed sequentially by employing an FFT module that computes the signal energy over the sub-bands which should be averaged over some time to strengthen this power estimation. A threshold is used to take decisions about individual sub-bands. Although there is no constraint about the spectrum utilization, the main weak point to this approach is the long sensing interval implied by sequentially

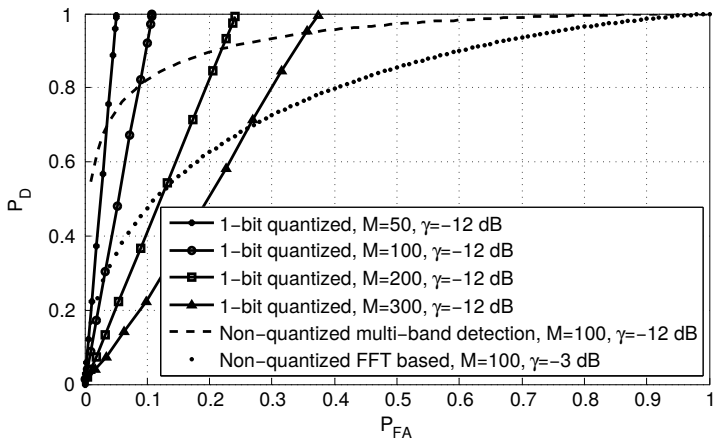

Figure 5.15: ROC curves for the proposed 1-bit quantized detector versus the FFT-based sequential sensing approach [119] and the multi-band detection approach [51]. Different utilization ratios apply for the 1-bit quantizer such that M =50, 100, 200, or 300. Averaging is applied over 100 captures for all techniques. α=0.1 dB for the 1-bit quantizer cases.

sensing the narrow bands and the time averaging. This technique is simulated at relatively high SNR (i.e., $\gamma = -3$dB) as shown in Fig. 5.15. In addition to the large power consumption and the desolation of the quantization effect, our proposed 1-bit quantizer system performs better even at very low SNR (i.e., $\gamma = -12$dB) with the condition of having a sparse spectrum.

Finally, the 1-bit quantizer performance is compared to the multi-band detection technique [51]. N bandpass filters have been designed to disjoint the sub-bands and hence narrow band energy detector can be applied to each sub-band. Each energy detector computes the average energy of the time domain samples presented by the corresponding filter. Averaging is applied over 100 samples. Although this technique shows better performance when compared to the FFT based, still the 1-bit quantizer can perform better for ultra sparse systems. Moreover, the complexity (requires 1024 filters) and power consumption (minimum of 1Watt) for the multi-band detector is quite significant when compared to the 1-bit quantizer.

5.5 Complexity and Power Consumption

5.5.1 Complexity

For the 1-bit quantized system based on the FFT-based energy detector, the complexity of the new system is very close to the classical FFT-based approach except for the additional buffers which have been compensated by the loss in the FFT complexity itself. The standard FFT complexity is represented by the number of arithmetic operations where the complexity is of $\mathcal{O}(N\log(N))$, if N is chosen to be a power of two. However, the processed samples are quantized to only $\{-1,+1\}$ and hence the twiddle multiplication are trivial since they will be implemented by a controlled negation operation. In this case, the complexity of the FFT reduces to only $\mathcal{O}(N\log(N)/2)$ as the first stage of the FFT does not involve any real multiplications.

Theoretically, autocorrelation has to be evaluated based on very large number of samples so that the statistical properties of the signal are captured. Practically, this is not an option due to complexity issues such as supporting large memory size and because of the unlimited sensing time. However, if correlation does not involve enough samples, the performance of the presented algorithm will be significantly impacted. One of the strongest points of our proposed architecture is that it utilizes window-based autocorrelation which provides practically implementable design. In addition, the 1-bit quantizer significantly reduces the complexity of the correlators. In reality, no real multipliers are required to process the correlation since only signs are multiplied. For a correlation window of size N and averaging over L windows, the complexity of the averaged window correlation reduces to only $2NL$ additions/subtractions. It is worthy to mention that the maximum word length of the correlation output is simply $1+\log_2(LN)$ as the input is only 1-bit quantized. One side note is that our approach employs a division operation to compute the unbiased correlation. Since these divisions are by constants, they are not involved in this complexity analysis. Moreover, the detection algorithm relies on the full knowledge of the thresholds which will be computed *off-line* based on the target performance, the operating SNR values, and the upper bound of the expected sparsity of the spectrum. Therefore, complexity for the detection algorithm mainly resides

on the comparisons that are employed by any other wideband sensing procedure utilizing a threshold approach.

5.5.2 Power Consumption

The overall power is distributed among three major blocks: RF processing, digital processing, and ADC. First, various voltage gain amplification stages can be removed from the RF chain as long as a 1-bit quantizer is employed. The reason is that 1-bit ADC intentionally requires the sign of the input signal and it does not rely on its strength. For the currently available ultra-wideband (UWB) systems operating at 500MHz bandwidth, it has been reported that 33% of the power consumption for the RF processing is dissipated by various gain amplifiers [126]. As a consequence, systems that employ 1-bit quantization would save this percentage of power at the RF chip.

Second, the power consumption for the digital processing depends on the system architecture, the complexity, the operating clock frequency, the word length of various variables, and the fabrication technology. As many parameters are involved to evaluate this part of the power consumption, it is hard to tell how much power is really consumed if the proposed architectures are employed as it is mainly an implementation dependent parameter. However, our architectures are compared to the closest one presented in [119]. For the FFT-based approach, the high speed buffer is an additional module and for the autocorrelation-based, the correlators will be the only additional processing since the FFT and the comparison logic present in both architectures. However, the power consumed from this additional increase in complexity has been compensated by reducing the operating clock frequency for the digital processor. The proposed architectures actually allow this feature due to the existence of the high speed buffers. For the autocorrelation-based approach, it is true that the correlation logic complexity (represented by $2NL$ additions) is comparable to the FFT complexity (represented by $N\log(N)$ operations). Therefore, if the operating clock frequency is reduced by 50% of the sampling rate, then the presented architecture will consume the same power, if not less, for the digital part as the FFT-based approach.

Third, ADC power consumption depends on ageing parameters such as the fabrication technology, the internal architecture, the operating frequency, and the resolution. As far

as the resolution is concerned, we can certainly claim that reducing the resolution to only one bit would make it possible for an ADC to dissipate the minimum power if all other factors remain unchanged. However, it is worth to elaborate on some details to support this idea. In general, the comparator is a fundamental component in the design of ADC converters. Various architectures can be utilized to design high-speed ADCs having low power consumption [127]. For K bits ADC, $2^K - 1$ comparators can be used alone with an encoder circuit to form a single flash ADC architecture. The power scales exponentially when compared to a single comparator power consumption. In reality, a single comparator will dissipate about 2^{-K} of the total power absorbed by this flash ADC. On the other hand, Successive Approximation (SAR) ADCs are power efficient for higher resolutions with lower speeds [128]. A SAR ADC usually employs a comparator, a digital-to-analogue converter (DAC), an up-down counter, and control logic where very recent designs show that the comparator consumes only 30% of the total power for SAR ADC [129]. However, SAR rates still do not follow the requirements for the ultra high speed conversion.

Alternatives to flash and SAR ADCs for high-speed low-power operation are hybrid and time-interleaved (TI) ADCs. The former uses a combined flash SAR configuration in a pipelined fashion [128] while the second approach employs multiple parallel low-speed high-resolution ADCs in a non-overlapped time intervals to quantize successive time samples [130]. Both architectures provide high throughput conversion on the account of employing multiple low-speed converters with low complexity proper calibration. In [128], 8-bit hybrid ADC is designed by employing one 3-bit flash ADC, four 5-bit SAR ADCs, and four comparators. In this case, the ADC consumes higher than or equal to $2^3 - 1 + 50/3 + 4 \simeq 28$ times of the 1-bit ADC. Moreover, if a TI ADC utilizes n SAR ADCs, then it will consume a power of at least $10n/3$ when compared to a single-bit ADC. Therefore, it is clear that a 1-bit ADC consumes power that is lower than the high resolution ADCs by order of magnitudes. From this discussion, one can conclude that the proposed architecture is optimized to dissipate significantly low power when compared to other approaches that employ high resolution ADCs.

5.6 Conclusion

Since the Nyquist-based wideband sensing relies on ultra high sampling rates, the corresponding power consumption from the high-resolution analogue to digital conversion is significantly high which makes it hard to reliably realize such solutions. In this chapter, we have presented two different approaches to utilize the 1-bit quantizer in Nyquist-based wideband spectrum sensing. The key objective is to reduce the power consumption from few watts to micro watts at the ADC stage. The first procedure can detect the activity of primary users over various sub-bands by monitoring the signal strength in frequency domain. Here, we derived the exact non-quantized ROC independent on the sensing interval to analyze the performance of the proposed algorithm. Further, we found expressions for the false alarm and detection rates in case of the 1-bit quantizer. Simulation results indicate that the derivations are accurate and reliable for various system parameters. As a result, our proposed architecture can greatly enhance the complexity and power consumption by selecting the proper system parameters so that the detection performance does not severely degraded when compared to the non-quantized case.

For the second approach, we presented an autocorrelation-based approach to estimate the PSD of the 1-bit quantized signal and hence to detect the presence of the PU in individual sub-bands. We derived the closed form expression for the window-based autocorrelation function which clearly shows the spectrum occupancy. We presented a detection algorithm that employs the average PSD to discriminate between vacant and occupied sub-bands. Complexity and power consumption have been quantified with respect to other architectures. Simulation results indicate that the detection accuracy is promising for sparse systems. As a result, our proposed system can greatly enhance the complexity, power consumption, and the performance for the wideband spectrum sensing problem.

Chapter 6

Synchronization and Cell Search Algorithms for LTE-MTC and NB-IoT Systems

6.1 Introduction

As mentioned earlier, one of the basic challenges to realize the next generation cellular M2M communication is the spectrum scarcity which has been addressed in the previous chapters. However, due to the challenging conditions at which devices are required to operate, there are other difficulties to implement practical and efficient devices. It is unusual for the conventional systems to design cellular low-power, low-cost, and enhanced-coverage equipments that can operate at ultra very low SNR values with reduced complexity. Although LTE-MTC systems share some of the transmission capabilities with the conventional LTE systems (for example, both systems can receive the same synchronization signals), practical algorithms have to be developed in order to detect these signals at very low SNR values and under fading conditions. In addition, it should be understood that systems with new signal structures such as NB-IoT require novel techniques to address its implementation challenges. In this chapter, we focus on some of the challenges to realize both LTE-MTC and NB-IoT systems. In specific, due to their important roles in data communication, we address the problems of initial synchronization, cell search, and frequency tracking [131] in LTE-MTC systems. We also consider the initial synchronization and cell detection for the NB-IoT systems which have new set of synchronization signals that are different from the conventional LTE (and LTE-MTC) synchronization signals. Other implementation challenges and issues are considered as future extension to his work.

During the initial physical channel setup [132], the UE shall search for a serving cell by acquiring the cell identity (ID) and the proper cell timing. Since OFDM systems are known to be sensitive to frequency errors, initial synchronization including CFO estimation is typically carried along with the cell search as CFO can be jointly estimated with the cell ID and symbol timing. LTE standard provides two synchronization signals, namely PSS and SSS, to assist completing the synchronization and cell search procedure. In literature, there are various techniques presented to perform both initial synchronization and cell search. All share the same procedure in the following order: (1) A coarse symbol timing has to be obtained first so that the received signal can be converted from time domain to frequency domain. At this stage, there are algorithms to estimate the fractional part of CFO as well [133][134]. (2) PSS (or sector ID) will be detected in the second step. (3) SSS (or cell ID group) will be found next [81][80]. (4) The detection of the integer part of CFO can be fulfilled. Some algorithms have been presented to enable this estimation within either Step 2 or Step 3 [132]. Other algorithms try different time domain approaches [135].

Since LTE-MTC introduces new challenges to the system, conventional cell search and initial synchronization techniques have to be revised. These techniques are designed to meet certain performance requirements, given by the cell detection accuracy and an acceptable frequency tolerance, in a well-defined environment with many degrees of freedom. In this regard, we provide a study and an evaluation to the conventional cell search approaches with respect to LTE-MTC specifications. It turns out that the current techniques with their default parameters fail to achieve the target performance at the desired SNR for extended coverage LTE-MTC mode. Fortunately, the consistent theme of the LTE-MTC specifications is to allow repetition that enhances the detection at very low SNR values. Following this standard spirit, we have utilized the allowed degree of freedom which is the time diversity to improve the performance of the conventional cell search approaches at such low SNR values. Without the help of any additional signalling, we prove by simulation that time averaging is a solution to meet the requirements for MTC-LTE for specific algorithms. On the other hand, it turns out that even with very long time averaging, some other algorithms fail to achieve the target performance at the required SNR.

After initial synchronization, residual frequency errors are always present due to the

Doppler shift and uncompensated residual errors, hence frequency tracking is required. Two issues arise with the introduction of LTE-MTC: (1) During EDRX cycles, frequency tracking is deactivated and DRX wakeup procedure requires resynchronization. (2) Enhanced coverage UEs are required to track frequency errors in very low SNR regimes. A new challenge is then introduced to keep tracking loops with high accuracy at these low SNRs. A compromise between accuracy and processing time appears here. For example, the widely used Maximum Likelihood (ML) CFO estimator [131], that relies on time domain autocorrelation for cyclic prefix samples, shows slow performance enhancements in deep fade environments and at low SNRs. Also, due to the limited bandwidth for the LTE-MTC system, insufficient number of Reference Symbols (RSs) are available for data aided approaches (e.g., [136] and references therein) to provide accurate frequency tracking in short processing time given the constrains of low SNR and fading condition. Fortunately, LTE-MTC employs the concept of repetition to enhance the detection of the physical broadcast channel. To achieve backward compatibility, the legacy PBCH symbols are repeated either four or five times in two consecutive subframes to form a well structured pattern. The MTC UE is supposed to soft combine these symbols to enhance the broadcast information detection under low SNRs. In this front, we propose a frequency tracking algorithm that utilizes the well structured repetitions of the MPBCH symbols. In addition to the analytical solution, we compare the performance of the presented algorithm with the conventional ML estimators. The performance is investigated with respect to the operating SNR and also to the required processing time.

When it comes to the most recent system, namely LTE NB-IoT, we present a novel algorithm to provide an initial timing and frequency acquisition and efficiently search for the serving cell ID. The coarse subframe timing is jointly obtained with the integer CFO by employing NPSS time domain correlation. Cell ID is acquired by utilizing differential frequency domain correlations to NSSS sequences. In fact, a new challenge is to keep the cell search and initial synchronization with high accuracy and reasonable complexity at very low SNRs. Therefore, an averaging mechanism is provided to tackle the trade-off between performance and processing time. In addition to the reduced complexity, the performance is investigated with respect to the operating SNR and also to the required processing time for various channel conditions.

6.2 System Model

Let $s(n)$ be a transmitted baseband OFDM signal. The received signal is given by,

$$y(n) \quad = \quad \Big[s(n) \star h(n) + w(n)\Big] e^{-j2\pi\varepsilon n} \tag{6.1}$$

where $h(n)$ is the impulse response of the multipath channel, $w(n)$ represents the AWGN, ε is the normalized CFO, and $\star$ denotes convolution. As stated before, in OFDM systems, CFO is typically normalized to the sub-carrier spacing where the total normalized CFO, ε, is represented by two terms: the fractional CFO, ε_F, and the integer CFO, ε_I, such that $\varepsilon = \varepsilon_I + \varepsilon_F$. Once the symbol timing is acquired and the CP type is known, the FFT engine is utilized to obtain the frequency domain representation of the received signal which can be derived from (6.1) as given by,

$$Y(k) \quad = \quad H(k)S(k-\varepsilon_I)e^{j2\pi(k-\varepsilon_I)\tau/N} e^{j2\pi\varepsilon_F \frac{N-1}{N}} \times \frac{\sin(\pi\varepsilon_F)}{N\sin(\pi\varepsilon_F/N)} + I(k) + W(k) \tag{6.2}$$

where N is the FFT size which is 128 for LTE-MTC, τ denotes the time misalignment error, $I(k)$ refers to the inter-carrier interference term due to the non-orthogonal sub-carriers, and $H(k)$, $S(k)$, $Y(k)$, and $W(k)$ are the frequency domain versions for $h(n)$, $s(n)$, $r(n)$, and $w(n)$, respectively.

6.3 Cell Search and Initial Synchronization in Conventional LTE Systems

In this section, we present the cell search and initial synchronization algorithms that provide potential solutions for the conventional LTE systems. The presented algorithms focus on the three main axes of the problem represented in timing acquisition, cell detection, and the frequency offset estimation.

6.3.1 Timing Acquisition Techniques

During timing acquisition, the UE requires setting the FFT window with proper timing alignments. In this front, two major techniques have been considered.

6.3.1.1 ML Timing Detection

In [131][132], several approaches on time and frequency synchronization for LTE have been investigated. According to conclusions of this study, the cyclic prefix based method for acquisition of the OFDM symbol timing and the fractional CFO is preferred. The cyclic prefix based method remains unaffected by the presence of high CFO, but estimates only the fractional part ε_F.

The log-likelihood function for the OFDM symbol start (θ) and the frequency mismatch (ε_F) can be written as given by,

$$\Lambda(\theta, \varepsilon_F) \quad = \quad 2\big|\gamma(\theta)\big| \cos\big(2\pi\varepsilon_F + \angle\gamma(\theta)\big) - \rho\mathcal{E}(\theta) \tag{6.3}$$

where $\gamma(\theta) = \sum_{k=n}^{n+L-1} y(k)y^*(k+N)$ is the correlation term, $\mathcal{E}(n) = \sum_{k=n}^{n+L-1} |y(k)|^2 + |y(k+N)|^2$ is the energy term, ρ is the magnitude of the correlation coefficient between $y(k)$ and $y(k+N)$ such that $\rho = \text{SNR}/(1+\text{SNR})$, and $\angle$ refers to the argument of the following complex variable. According to [132], the ML estimate of θ and ε_F maximizes the function $\Lambda(\theta, \varepsilon_F)$ such that $\widehat{\theta}_{ML} = \arg\max_\theta[2|\gamma(\theta)| - \rho\mathcal{E}(\theta)]$ and $\widehat{\varepsilon}_{F,\,ML} = \frac{-1}{2\pi}\angle\gamma\big(\widehat{\theta}_{ML}\big)$

6.3.1.2 PSS Timing Detection

Since there are only three combinations for sector IDs, it is feasible, from the complexity perspective, for a UE to cross-correlate the received signal and the PSS symbol replica in time domain. Maximizing such a correlation provides a joint estimate to the PSS symbol timing and the sector ID of the serving cell [137][138] as given by,

$$(\widehat{\theta}, \widehat{N}_{ID}^2) \quad = \quad \arg \max_{\substack{\theta \\ j\in\{0,1,2\}}} \big|\bar{\Lambda}(\theta, j)\big| \tag{6.4}$$

where $\bar{\Lambda}(\theta, j) = \sum_{n=\theta}^{\theta+N-1} y(n)d_j^*(n-\theta)$ is the correlation cost function, $d_j(n)$ represents the time domain reference PSS symbol with sector ID of j. The correlation period should respect the repetition of the PSS that takes place every 5ms. Unfortunately, similar to the ML approach, the timing still does not provide information about the frame timing as the differentiation between sub-frame 0 and sub-frame 5 is encountered by the SSS not the PSS.

6.3.2 Conventional Cell Detection and Initial Synchronization Techniques

The PSS detection was proposed to be performed in Time Domain (TD) [135][139] as mentioned in section 6.3.1.2 by employing a matched filter approach. However, it is generally assumed [132][140] that the oscillator mismatch produces an integer frequency offset in the range $\varepsilon_I \in [-2, +2]$. The existence of this integer frequency offset will certainly degrade the performance for detecting PSS in time domain. Hence, the PSS detection and integer frequency offset are proposed to be jointly estimated [141] where the cost function is redefined as given by (6.5). The idea is to introduce progressive phase shifts for the reference PSS symbols before applying the cross correlation. Hypotheses are defined to generate the pre-correction phase shifts as a function of the claimed integer frequency offset. Maximizing the cost function over all possible sector IDs and all possible integer frequency offsets will provide a joint estimate for the sector ID and the attached integer frequency offset. The main disadvantage of this approach is the complexity where the number of correlation banks is triple the number of the expected integer frequency offset since the correlation is applied for the three possible PSS IDs.

$$\bar{\Lambda}(\theta, j, \varepsilon_I) \quad = \quad \sum_{n=\theta}^{\theta+N-1} y(n) d_j^*(n-\theta) e^{\frac{j2\pi\varepsilon_I(n-\theta)}{N}} \tag{6.5}$$

On the other hand, if CP correlation is involved to obtain timing, PSS (and SSS) can be detected by employing correlations in frequency domain [81]. However, there usually exists a non-negligible symbol timing error due to not only the unequal CP lengths for normal CP type [142] but also the estimation accuracy. As noticed from (6.2), any time mismatch introduces phase rotations to the frequency domain sub-carriers which degrade the detection for PSS/SSS. To improve the PSS detection in the presence of a timing error, the differential correlation scheme was proposed in [142]. Here, the cross-correlation between the received differential PSS and the local differential reference PSS is maximized as given by (6.6).

$$\widehat{N}_{ID}^2 \quad = \quad \arg \max_{j \in \{0,1,2\}} \left| \sum_{\substack{k=-31 \\ k \neq 0,1}}^{31} \mathcal{Y}(k) \mathcal{D}_j^*(k) \right| \tag{6.6}$$

where $\mathcal{Y}(k) = Y(k)Y^*(k-1)$, $\mathcal{D}_j(k) = D_j(k)D_j^*(k-1)$, $Y(k)$ is the received PSS symbol at sub-carrier k, and $D_j(k)$ is the reference PSS symbol for sector ID, j, at sub-carrier k. It is assumed that the coherence bandwidth of the channel is much higher than the sub-carrier spacing so that adjacent sub-carriers almost suffer from the same channel effect. In case of perfect synchronization, the term $\mathcal{Y}(k) = [H(k)S(k) + W(k)][H(k-1)S(k-1) + W(k-1)]^*$ has implicitly three noise terms other than $H(k)H^*(k-1)S(k)S^*(k-1)$. Statistically, those noise terms vanish since $W(k)$ and $W(k-1)$ are assumed to be independent and $\mathbb{E}[W(k)] = 0$ where $\mathbb{E}$ denotes expectation. However, practical realization for this averaging is not easy especially for very low SNR values and limited number of sub-carriers to average over.

Due to complexity issues for the SSS detection, research proposals prefer to process SSS detection in Frequency Domain (FD) as symbol timing is assumed to be already acquired by timing acquisition. The main difference is whether to apply coherent detection or non-coherent detection. In coherent detection [143][139], the channel estimates are provided by the PSS symbol as it is assumed that the channel does not rapidly vary from one OFDM symbol to the following one. The SSS symbol is equalized by the channel estimates before applying the correlations to maximize the detection accuracy. In its simplest form, least squares channel estimates are computed from the PSS symbol [144] by which SSS is equalized. The maximization problem over the coherent SSS correlations is given by (6.7), where $\mathcal{S}_j^*(k)$ represents the reference SSS symbol with index j at sub-carrier k and $H_{PSS}(k)$ is the least squares channel estimate obtained from the PSS symbol at sub-carrier k. Similar to PSS detection, non-coherent detection based on differential correlation for SSS has been also presented [132][139]. The channel effect is removed by considering the differential cross-correlation between successive sub-carriers. Again, it is expected to have poor performance for this approach at very low SNR values. However, the complexity of the former is higher due to involving channel estimation and equalization.

$$\widehat{N}_{ID}^1 = \arg \max_{j \in [0,167]} \left| \sum_{\substack{k=-31 \\ k \neq 0}}^{31} \frac{\mathcal{Y}(k)\mathcal{S}_j^*(k)H_{PSS}^*(k)}{\left|H_{PSS}(k)\right|^2} \right| \tag{6.7}$$

The detection of integer CFO may be processed along with the search process of SSS [132] or with PSS [81] if either or both will be processed in the frequency domain. Different frequency lags are introduced to the cross-correlations and more hypotheses are generated.

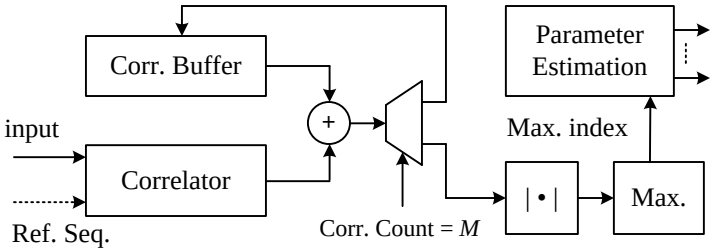

Figure 6.1: General architecture for the proposed averaging methodology for various cell search and initial synchronization algorithms.

The maximum cross-correlation jointly estimates the sector or the group ID as well as the integer CFO. For example, frequency lags can be introduced to the non-coherent SSS detector as given by (6.8), wehere the intger frequency offset is assumed to be in the range $[-2, +2]$. The estimator can now jointly detect the SSS index in addition to the proper integer frequency lag.

$$\{\widehat{N}^1_{ID}, \varepsilon_I\} \quad = \quad \arg \max_{\substack{j\in\{0,1,2\} \\ p\in[-2,+2]}} \left| \sum_{\substack{k=-31 \\ k\neq 0,1}}^{31} \mathcal{Y}(k-p)\mathcal{S}^*_j(k) \right| \tag{6.8}$$

6.4 Proposed Cell Search and Initial Synchronization for LTE-MTC Systems

Conventional LTE specifications define an operating point of SNR=-6dBs for cell search and initial synchronization. However, extended coverage LTE-MTC specifications are more challenging since the operating SNR value should be as low as -15dB. In fact, traditional methods utilize two receive antennas that provides a diversity again of about 3dB for AWGN unlike the LTE-MTC that employs only one receive antenna. Furthermore, a maximum system bandwidth of 20MHz for conventional LTE provides about 4dBs gain when compared to only 1.4MHz for LTE-MTC. All these challenges do not allow a room for a solution except if time diversity is employed.

In this section, we modify the conventional techniques for cell search and initial synchro-

Table 6.1: Different approaches to realize cell search and initial synchronization for LTE systems

Approach	1	2	3	4	5	6
Timing Acq.	ML CP Correlation				PSS TD Correlation	
PSS Detection	Direct Corr.	Diff. Corr.	Direct Corr.	Diff. Corr.	-	
SSS Detection	Coherent		Diff. Corr.		Coherent	Diff. Corr.
ε_I Est.	FD PSS Corr.				TD PSS Corr.	

nization to include more averaging over the decision statistic. Introducing this averaging will enhance the noise rejection and hence provides better performance at very low SNR values. Yet, the decision statistic evaluation is repeated M times. Then the final decision statistic is obtained by averaging all the outcomes. On the other hand, this noise filtering approach consumes longer detection/estimation time depending on the number of repetitions and the period of each trial. Simulations will be employed to decide on the required processing time, or alternatively the parameter M, to achieve the target performance.

Regarding the timing acquisition problem, the performance of the ML estimator does not perform well at low SNR and for fading channels as well. Averaging $\Lambda(\theta, \varepsilon_F)$ over several OFDM symbols is required to improve the performance. In fact, Normal CP mode requires careful attention as the number of CP samples differs from the first OFDM symbol of the slot to other symbols in the slot. To overcome this problem, the CP correlation is reset every slot whose number of samples is exactly 960 samples. The correlation outputs from multiple slots are averaged as a first step. Next, the correlation output is divided into 7 regions that are averaged together to have a single symbol-like correlation from which timing is obtained. When PSS timing is utilized, the cross-correlations from the same base sequence are averaged over M consecutive windows where each window involves TD samples for 5ms. The definition for the modified decision statistic is given by (6.9) where $\bar{\Lambda}_m(\theta, j, \varepsilon_I)$ is the decision statistic over a window of 5ms samples whose index is m. Similarly, if PSS is to be detected in the frequency domain, the decision statistic of the cross-correlation either for

the direct cross-correlation or the differential one is averaged every 5ms. The maximization is applied to detect the sector ID jointly with the integer frequency offset over the averaged decision statistic. Similar to PSS, the periodicity of the SSS symbol is every 5ms. Therefore, the detection of either PSS or SSS will be multiple of 5ms depending on the number of windows to average over.

$$\bar{\Lambda}_{\text{Mod}}(\theta, j, \varepsilon_I) \quad = \quad \frac{1}{M} \sum_{m=1}^{M} \bar{\Lambda}_m(\theta, j, \varepsilon_I) \tag{6.9}$$

A general architecture for the proposed modified algorithms is shown in Fig. 6.1. A correlator is employed to either autocorrelate the incoming sequence (in case of CP correlation) or to cross-correlate the incoming sequence with known reference sequences (in case of PSS and SSS correlations). The correlation output is added to the contents of the correlation buffer to which the sum is saved. Of course, the correlation buffer is initialized to zeros. Once the iteration count comes to M, the correlation sum is directed to another path in which the maximum absolute is evaluated. The estimated parameters such as the symbol timing, PSS index, SSS index, or the integer CFO part are then obtained as a function

Motivated by the presented discussion, we define the most common scenarios for cell search and initial synchronization as listed by Table 6.1. Each scenario assumes specific algorithms for the four parameters of interest. Our objective is to evaluate the performance of various techniques when averaging is involved. Different channel models such as AWGN and standard LTE fading channels have to be involved in addition to the target SNR=-15dB for extended coverage LTE-MTC UEs. By strictly defining the expected accuracy of each stage, one can assume independent performance measures for various blocks.

6.4.1 Simulation Results

We carried out link level simulations for evaluating the performance of the presented algorithms. The 1.4MHz LTE-MTC system is considered, with a sampling frequency of 1.92 MHz, 128-point FFT/IFFT, 15kHz sub-carrier spacing, one antenna at transmitter and receiver, and a Normal CP mode. In extended coverage mode, it is not likely for LTE-MTC device to move as fast as a high speed train. Therefore, we have considered low mobility channels. For instance, AWGN and EPA-5 [75][145] were simulated. EPA-5 is a standard

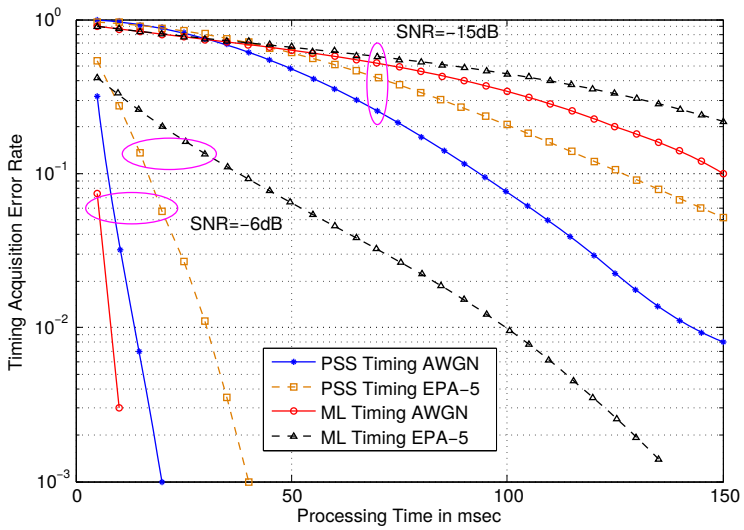

Figure 6.2: Performance for various timing acquisition techniques under different channel conditions and for SNR=-6dB and -15dB. Horizontal axis is related to the averaging length for timing acquisition techniques.

LTE channel with large coherence time (maximum Doppler spread is 5Hz). Simulations were performed over 10^6 sub-frames over independent channel realizations for the conventional SNR of -6dBs and the extended coverage LTE-MTC SNR of -15dBs. We also considered a frequency misalignment of 31.5KHz (i.e, $\varepsilon = 2.1$). A maximum time frame of 150ms is assumed to evaluate the averaging performance gain.

Fig. 6.2 shows the performance (represented by the timing error rate) for the timing acquisition techniques versus the required processing time. Since the CP is 9 samples long, we assume that the timing is in error if the estimated symbol start is shifted from the true one by 4 samples at most. The reason is that OFDM orthogonality can be maintained if the timing is adjusted up to the edge of the cyclic prefix. For conventional acquisition SNR, it is clear that the ML method is sensitive to fading channels more than the PSS timing approach. Originally, fading channels introduce inter-symbol interference which is absorbed by the cyclic prefix and hence the CP is no longer a true copy of the OFDM symbol tail (if the noise is ignored). For extended coverage LTE-MTC, it is obvious that the noise dominates and the difference between fading and AWGN channels is relatively small. Although PSS timing provides better performance, the absolute processing time is quite large (order of 0.2sec or

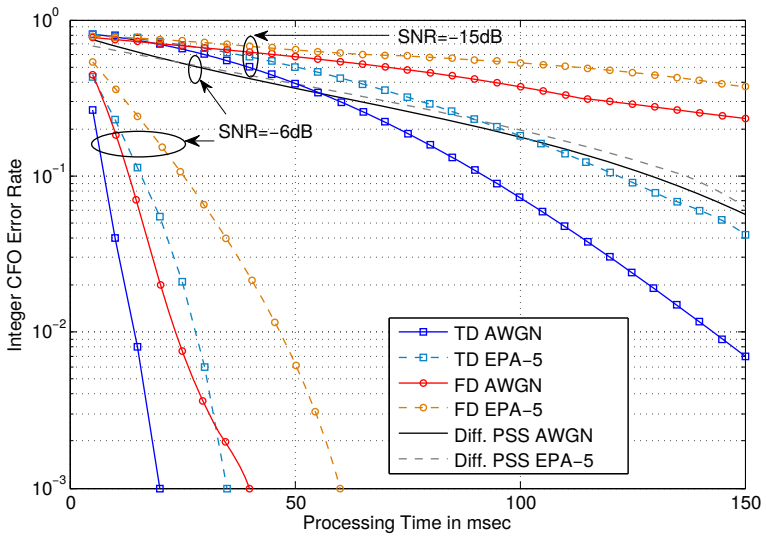

Figure 6.3: Integer frequency offset detection rate for different estimation approaches and under different channel conditions.

more for 1% error rate). A possible solution to have good timing accuracy with reasonable performance is that LTE-MTC specifications provide repetition to the synchronization signals more than once within the 5ms period.

Fig. 6.3 shows the estimation accuracy for the integer frequency offset under different channel conditions and different SNR values. In reality, TD estimation approach is powerful in performance when the processing time is fixed. It is also clear that the differential PSS approach is far away from the other techniques at SNR=-6dB due to the noise magnification issue discussed in section 6.3.2. The problem will be even worse for SNR=-15dB. One of the conclusions is that differential detection approaches have very little chances for LTE-MTC environment compared to other techniques. It will be shown by the following results that the differential approaches not only have issues with integer frequency offset but also the detection accuracy for PSS/SSS is not a prayer.

Fig. 6.4 shows the detection accuracy for PSS detection under different channel conditions and different SNR values. In addition to the time domain PSS detection approach, PSS detection is processed in frequency domain if ML timing acquisition is utilized. It is clear that TD PSS consumes less averaging to achieve the same performance when compared to other approaches. Again, differential detection is away from the rest even at the conventional

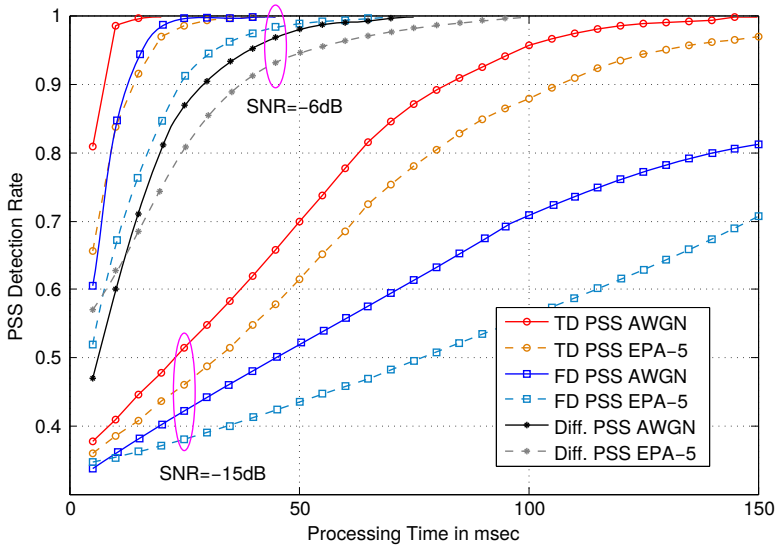

Figure 6.4: Detection probability versus processing time for PSS under different detection techniques. Different channel conditions are considered with SNR=-6dB and -15dBs.

SNR. Therefore, we do not recommend the differential approach with averaging for LTE-MTC systems. Once PSS is detected, SSS detection is applied in the frequency domain by either coherent or differential detection. Fig. 6.5 shows the simulated SSS detection probability under different channels and different SNR values. In case of coherent detection, simple least-squares channel estimation is applied for the PSS symbol. To evaluate the channel estimates, the received PSS sub-carriers are multiplied by the conjugate of the corresponding reference PSS sub-carrier. The output is smoothed by averaging adjacent sub-carriers (5 sub-carriers are considered from each side). SSS symbol is equalized using a simple zero-forcing equalizer that employs the PSS channel estimates. Based on these simulations, we cannot only provide the 90%-detection time budget for an algorithm, but also we can conclude that TD PSS along with coherent SSS would work faster for the cell search and initial synchronization problem in LTE-MTC systems.

6.5 Frequency Tracking For LTE-MTC Systems

In this section, we summarize the common estimators that have been employed to track the frequency in conventional LTE systems. Also, we present the details of the proposed

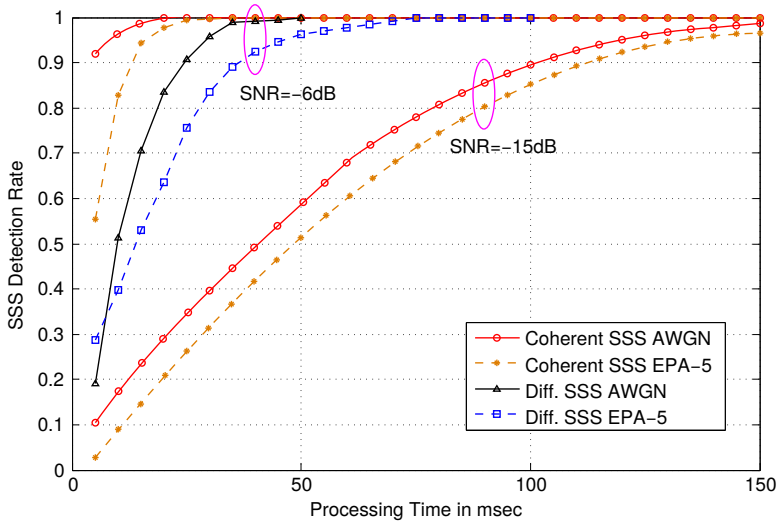

Figure 6.5: Detection probability versus processing time for SSS under different detection techniques. Different channel conditions are considered with SNR=-6dB and -15dBs.

estimator based on MPBCH data repetition. In order not to cause any inconvenience, in this section, the frequency error is represented by ε_c. Typically, this frequency error is the residual error in estimating the fractional frequency offset and hence it is much smaller than ε_F obtained from the initial synchronization procedure.

6.5.1 Time Domain ML Estimator

The same approach defined in section 6.3.1.1 can be utilized to track the fractional frequency offset. Thus, an ML estimator for ε_c can be defined by (6.10), where $\gamma(\theta) = \sum_{m=n}^{n+L-1} y(m)y^*(m+N)$ is the correlation term.

$$\widehat{\varepsilon}_{c,ML} = \frac{-1}{2\pi}\angle\gamma\big(\widehat{\theta}_{ML}\big) \tag{6.10}$$

6.5.2 Frequency Domain Pilot-Based Estimator

The frequency offset can be tracked by measuring the phase shift of pilot symbols in OFDM symbols that contain pilots in two consecutive LTE slots [136]. Let J, p_j, and $S_l(p_j)$ denote the number of pilot tones, the location of the j^{th} pilot tone, and the pilot value located at p_j in the frequency domain at the l^{th} OFDM symbol, respectively. If two OFDM symbols spaced

by D symbols contain pilots at the same pilot positions, an ML estimator is designed in [146] to estimate the frequency offset as given by (6.11) where $\alpha^{-1} = 2\pi(DN+DL+1)/N$ for FDD LTE with Normal CP. For a single transmit antenna configuration, four pilot symbols are allocated for each subframe such that the spacing between identical pilot symbols is $D = 7$. In this case, the estimation range reduces to only $|\varepsilon_c| < 64/960$.

$$\widehat{\varepsilon}_c = \alpha \angle \left\{ \sum_{j=0}^{J-1} Y_l^*(p_j) Y_{l+D}(p_j) S_l(p_j) S_{l+D}^*(p_j) \right\} \tag{6.11}$$

6.5.3 Proposed MPBCH-Based CFO Estimator

One typical data-aided frequency tracking approach is to employ repetitive preambles which remain identical after passing through the transmission channel except for a phase shift produced by the frequency offset. The frequency offset is thus estimated by measuring the induced phase shift [106]. Let us assume that $s_l(n)$ and $s_{l+D}(n)$ are two identical transmitted symbols in MPBCH such that the symbols are spaced by $D-1$ symbols. In this case, under the assumption that the channel remains constant over adjacent $D+1$ symbols, the corresponding noise-free received symbols are related to each others such that $r_{l+D}(n) = r_l(n)e^{j\varepsilon_c/\beta}$ where $\beta = N/(2\pi D(N+L))$. Consequently, the frequency domain symbols will inherit the same scaling and hence $R_{l+D}(k) = R_l(k)e^{j\varepsilon_c/\beta}$. In vector notation, this relation is rewritten as,

$$\begin{aligned} \mathbf{Y}_l &= \mathbf{R}_l + \mathbf{W}_l \\ \mathbf{Y}_{l+D} &= \mathbf{R}_{l+D} + \mathbf{W}_{l+D} = \Theta\, \mathbf{R}_l + \mathbf{W}_{l+D} \end{aligned} \tag{6.12}$$

where $\Theta = e^{j\varepsilon_c/\beta}\mathbf{I}$ is an $N \times N$ matrix representing the CFO coefficients, $\mathbf{I}$ is the identity matrix, $\mathbf{Y}_i = [Y_i(0)\ \ldots\ Y_i(N-1)]^T$ represents the i^{th} received symbol vector, $\mathbf{R}_i = [R_i(0)\ \ldots\ R_i(N-1)]^T$ represents the i^{th} noise-free received symbol vector, and $\mathbf{W}_i$ is the noise vector at symbol i. In [147], it has been shown that an ML estimator for the differential phase can be obtained by minimizing the cost function $\digamma(\Theta)$ given by (6.13) where H denotes hermitian transpose operator. By differentiating $\digamma(\Theta)$ with respect to ε_c, equate the result to zero, and employ the fact that $\Theta[\mathrm{d}\Theta/\mathrm{d}\varepsilon_c]^H + [\mathrm{d}\Theta/\mathrm{d}\varepsilon_c]\Theta^H = \mathbf{0}$, it follows that an

unbiased estimator for the CFO can be achieved and the estimated CFO is given by (6.14).

$$\digamma(\Theta) = \Big[\mathbf{Y}_{l+D} - \Theta\mathbf{Y}_l\Big]^H \Big[\mathbf{Y}_{l+D} - \Theta\mathbf{Y}_l\Big] \tag{6.13}$$

$$\widehat{\varepsilon}_c = \beta \angle\Big[\mathbf{Y}_l^H \, \mathbf{Y}_{l+D}\Big] \tag{6.14}$$

As shown in Fig. 2.7, in the proposed MPBCH, the separation between different repetitions is irregular. Thus, to estimate the CFO based on repetitive MPBCH symbols, we have divided the repetitions into four groups, namely G_0 to G_3. Each group has two sets of OFDM symbols. Each set represents the closest replica for the other set. The spacing, D_i, between each OFDM symbol and its corresponding repetition in a group G_i is the same for all OFDM symbols contained by group G_i. With this definition, averaging over phase differences for all OFDM symbols enclosed by one group is possible. This averaging reduces the estimation noise and enhances the accuracy. Let the decision statistic over a certain radio frame m for group G_i be denoted by $\Gamma_m^i = \sum_{\forall\, l \in G_i} \mathbf{Y}_{\{l,i,m\}}^H \mathbf{Y}_{\{l+D_i,i,m\}}$ where $\mathbf{Y}_{\{l,i,m\}}$ is the received FD symbol l inside one of the two sets contained by group G_i at radio frame m.

Since the estimation formula given by (6.14) is different for each group, we employ a weighted averaging for the estimates produced by various groups to finally evaluate the CFO estimate. If we define the CFO estimate for group i at radio frame m to be $\widehat{\varepsilon}_{c,i,m} = \beta_i \angle \Gamma_m^i$, then the final estimated CFO at radio frame m is obtained by $\widehat{\varepsilon}_{c,m} = \sum_{i=0}^{3} \omega_i \widehat{\varepsilon}_{c,i,m}$. In its simplest form, the weighting coefficients $\omega_i = 1/4$ to preserve unbiased estimator. It is worth to mention that the proposed approach limits the CFO estimation range to the minimum range achieved by all groups. To emphasize, the frequency offset that can be measured without ambiguity is $|\varepsilon_c| < 64/549$ or equivalently 1.75KHz, where we accounted for four symbols to represent the separation D.

For insufficient number of observations, the performance of ML estimators may not perform very well at very low SNR and for deep fading conditions as well. In this case, averaging the decision statistic over multiple observation windows is required to improve the performance [106]. In case of the proposed MPBCH estimator, a single observation window is a complete radio frame (i.e., 10ms). The CFO estimator after M windows is defined by (6.15). Similar averaging can be defined to the other estimators. However, the processing time for an estimation algorithm is defined by the window periodicity and the number of processed win-

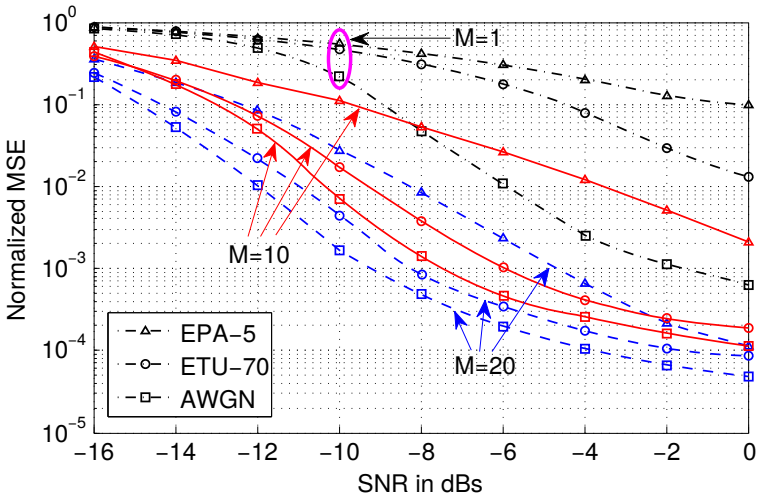

Figure 6.6: Normalized MSE showing the averaging effect for MPBCH-based estimator for $M \in \{1, 10, 20\}$ and under different channel conditions.

dows. It is worth to mention that the pilot-based estimator and the time domain estimator are repeated and averaged every sub-frame (i.e., 1ms).

$$\widehat{\varepsilon}_c = \sum_{i=0}^{3} \omega_i \beta_i \angle \left[\sum_{m=0}^{M-1} \Gamma_m^i \right] \tag{6.15}$$

6.5.4 Simulation Results

Again, we carried out link level simulations for evaluating the performance of the presented algorithms. The same LTE-MTC settings, including a sampling frequency of 1.92 MHz, 128-point FFT/IFFT, 15kHz sub-carrier spacing, f_c = 2.6GH, one antenna at transmitter and receiver, and a Normal CP mode, are considered. Thus, a total of $12 \times 4 = 48$ pilot sub-carriers are allocated per subframe. AWGN and two standard LTE channels, namely EPA-5 and ETU-70 [75], were simulated. ETU-70 is a dispersive channel with maximum Doppler spread of 70Hz. The frequency offset is assumed to be 1.5KHz. However, due to the estimation range limit, it is 750Hz in case of the pilot-based estimator.

For various channel conditions, Fig. 6.6 shows the performance of the MPBCH-based estimator represented in the normalized Mean Squared Error (MSE) defined by (6.16), where $\widehat{\varepsilon}_c^p$ is the estimated frequency error from trial p and up to P trials are considered. The averaging over observation windows is activated such that three averaging periods are investigated

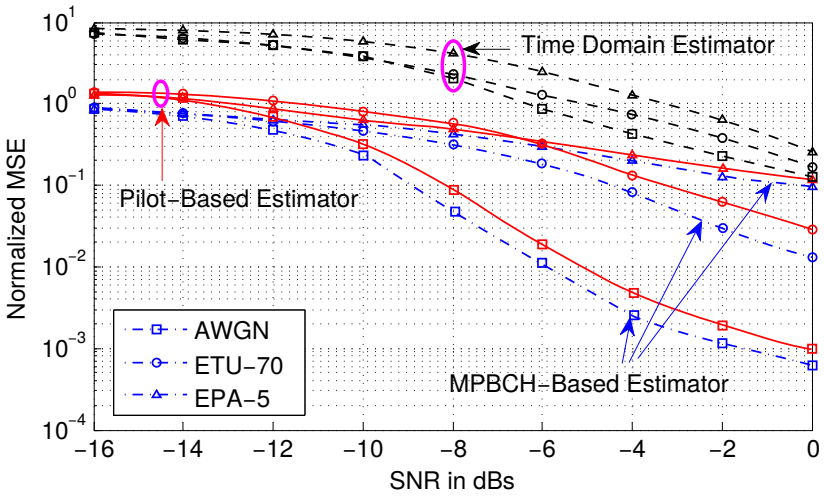

Figure 6.7: Normalized MSE for various estimator versus SNR under AWG, EPA-5, and ETU-70 channels. No averaging is employed.

where M =1, 10, or 20. It is clear that deep fading channels like EPA-5 affect the performance. However, averaging over longer periods significantly enhances the accuracy. For example, increasing the averaging from M=10 to M=20 provides a again of about 6dBs at MSE=2×10^{-3}. With high speed Doppler (i.e., ETU-70), the performance is close to AWGN. Thus, the estimator is more robust against high Doppler which validates the assumption of a constant channel over consecutive symbols.

$$\text{MSE} \quad = \quad \frac{1}{P}\sum_{p=1}^{P}\left|\frac{\widehat{\varepsilon}_c^{\,p}-\varepsilon_c}{\varepsilon_c}\right|^2 \tag{6.16}$$

To compare various estimators in the LTE-MTC environment, the normalized MSE for various estimators against SNR is evaluated when averaging is deactivated as shown in Fig. 6.7. Two aspects arise: (1) although the time domain estimator provides the widest estimation range (i.e., $|\varepsilon_c| < 0.5$) [131], its performance is quite poor. In reality, the number of CP samples for LTE-MTC is quite small when compared to legacy LTE in which this estimator performs better. (2) Due to the insufficient number of pilots for LTE-MTC system, the pilot-based estimator performance degrades when fading is employed. However, it still performs better than the CP correlation estimator in all cases. It is also clear that the performance difference between the pilot-based and the MPBCH estimator in noticeable for ETU-70 in which the constant channel assumption is almost acceptable for MPBCH-

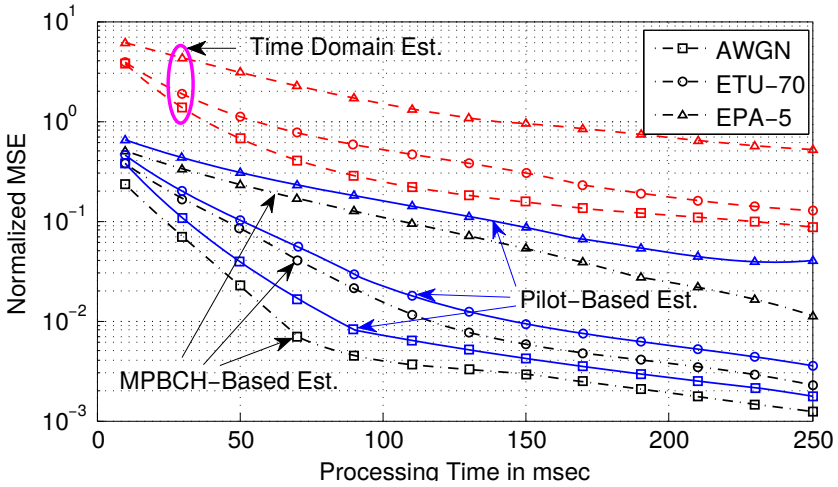

Figure 6.8: Normalized MSE versus processing time for various estimators and under AWGN, EPA-5, and ETU-70 channels such that SNR=-10dBs

based estimator but not for the pilot-based especially at high SNR values. The source of this distinction is the spacing between the repetitions which is high in case of utilizing pilots. Further, even without averaging, the MPBCH estimator performs better for all channel conditions when compared to other techniques.

By changing the averaging period and accounting for different observation window periods for various estimators, Fig. 6.8 shows the performance for various estimators versus the processing time. The main point here is how fast an estimator can reach a desired performance under this challenging environment. For a fixed target performance, the frequency tracking loop will converge quickly if the processing time for the open loop estimator is relatively small. It is clear that less averaging is required for the proposed MPBCH estimator to achieve the target performance independent on the channel. It is also obvious that performance slope is slowly changing but the MPBCH estimator reaches its floor quickly.

6.6 Proposed Initial Synchronization and Cell Search for NB-IoT Systems

As presented in Section 2.6.3, the NB-IoT system has new special requirements than LTE-MTC. With only 180KHz bandwidth which can be deployed as a single physical resource

block in LTE network or as a standalone system, NB-IoT system cannot reuse the legacy synchronization signals that span 1MHz. For this reason, NB-IoT systems have new introduced synchronization signals, namely NPSS and NSSS, which carry the cell information including the cell timing and cell ID. Based on the new signal structure, periodicity, and NB-IoT capabilities in general, in this section, we present an initial synchronization and cell search procedure for NB-IoT systems. The procedure has two parts: timing and frequency acquisition, followed by cell search.

6.6.1 Timing and Frequency Acquisition

As a general OFDM system, symbol timing can be acquired in LTE systems by employing a CP correlation algorithm. Again, the ML approach defined by section 6.3.1.1 can be employed to acquire the general symbol timing. In legacy LTE, symbol timing can be also acquired though PSS detection [139] by trying all possible timing hypothesis within the PSS window (i.e., 5msec). However, in addition to the CP type detection, the subframe numbering is associated with SSS detection since only SSS carries the information about the slot index. Thus, timing acquisition in legacy LTE is a challenging process as it requires solving many hypotheses about PSS, SSS, and CP type. For the frequency synchronization, research proposals [144] prefer to estimate the integer CFO jointly with the SSS index by introducing frequency lags to the FD SSS correlations. Since SSS is a binary sequence, complexity is reduced as correlations have trivial multiplications.

In NB-IoT, neither NPSS is a function of the cell ID nor NSSS is a binary sequence. In addition, NPSS and NSSS almost span complete subframes and the CP pattern is known in advance. By employing a matched filter to the NPSS, symbol timing and subframe boundaries can be jointly obtained. However, due to a possible integer frequency offset, the performance is degraded because of the poor cross-correlation. We present an acquisition approach in which timing and frequency are jointly acquired. Let us define the cross-correlation cost function, $\Lambda_m(\delta, \varepsilon_I)$, within a correlation window m, as given by (6.17), where $p(n)$ is an N_P-samples sequence representing the concatenated TD OFDM symbols carrying the NPSS

and N_w is the number of samples per NPSS window (i.e., 10msec).

$$\Lambda_m(\delta, \varepsilon_I) \quad = \quad \sum_{n=\delta}^{\delta+N_P-1} y(n)p^*(n-\delta)e^{\frac{j2\pi\varepsilon_I(n-\delta)}{N}} \tag{6.17}$$

The idea is to introduce progressive phase shifts for the reference TD NPSS sequence before applying the cross correlation. Hypotheses are defined to generate the pre-correction phase shifts as a function of the claimed integer frequency offset. Since the NPSS is relatively immune to fractional CFO, it is generally assumed [140] that the oscillator mismatch produces an integer frequency offset in the range $\varepsilon_I \in [-2, +2]$. The main limitation of this approach is the complexity, where the number of correlation banks is exactly the same number of the expected integer frequency offsets. It is expected that at very low SNR values, the noise power dominates over the correlation and thus the performance is degraded. In order to preserve a good performance with reasonable complexity, the decision statistic is averaged over M consecutive NPSS windows to further reject the noise. Maximizing the average cost function over all possible integer frequency offsets and various timing offsets within NPSS window will provide a joint estimate for the proper subframe timing and the attached integer frequency offset. Thus, the averaged decision statistic is evaluated as, $\bar{\Lambda}(\delta, \varepsilon_I) = \frac{1}{M}\sum_{m=0}^{M-1}\Lambda_m(\delta, \varepsilon_I)$, and timing and frequency offset estimation can be formed as,

$$(\hat{\delta}, \hat{\varepsilon}_I) = \arg \max_{\forall \delta,\, \varepsilon_I \in [-2,+2]} \left|\bar{\Lambda}(\delta, \varepsilon_I)\right| \tag{6.18}$$

6.6.2 Cell Search

In legacy LTE, SSS can be coherently identified [144]. Before applying correlations with the reference sequences, the SSS symbol is equalized by the channel estimates to maximize the detection accuracy. The channel estimates are provided by the PSS symbol as it is assumed that the channel does not rapidly vary from one OFDM symbol to the following one. Unfortunately, there are couple of challenges to apply a similar procedure to NB-IoT. The NSSS is no longer adjacent to NPSS and hence channel estimates can not be easily obtained. Also, the NSSS samples are cyclic shifted according to the radio frame number and this doubles the number of hypotheses to detect the cell ID. Motivated by these challenges and the legacy LTE cell detection in [139][148], we present a differential cross-correlation scheme

for cell ID identification in NB-IoT. For a given NSSS window, m, the decision statistic for the differential cross-correlation between the received FD NSSS and the local reference NSSS is defined by (6.19), where k_0 is the first sub-carrier to which NSSS is mapped, $Y_l^m(k)$ is the received NSSS within window m, at sub-carrier k and OFDM symbol l, and $S_l^i(k)$ is the reference NSSS for cell ID i, at sub-carrier k and OFDM symbol index l.

$$\Lambda_m(i) = \sum_{l=3}^{13} \sum_{k=k_0}^{k_0+10} Y_l^m(k) Y_l^{m*}(k+1) S_l^{i*}(k) S_l^i(k+1) \tag{6.19}$$

In the context of NB-IoT, there are couple of advantages for this definition. First, it is assumed that the coherence bandwidth of the channel is much higher than the sub-carrier spacing so that adjacent sub-carriers almost suffer from the same channel effect. Therefore, non-coherent detection is possible without any prior knowledge about the Channel State Information (CSI). Indeed, the channel effect is removed by considering the differential cross-correlation between successive sub-carriers. Second, the sequence $[S_l^i(k)]^* S_l^i(k+1)$ is a new sequence derived from the NSSS such that it involves a common phase rotation of $e^{-j2\pi\theta_f}$ independent on the sub-carrier index. Actually, this factor vanishes when the absolute operator is applied. Thus, the dependency on the radio frame number has been removed.

On the other hand, there are couple of limitations. Let $H_l^m(k)$ be the channel coefficient at sub-carrier k, OFDM symbol l, and NSSS window m. The term $Y_l^m(k)[Y_l^m(k+1)]^* = [H_l^m(k)S_l(k)+W_l^m(k)][H_l^m(k+1)S_l(k+1)+W_l^m(k+1)]^*$ has implicitly three noise terms other than $H_l^m(k)S_l(k)[H_l^m(k+1)S_l(k+1)]^*$. Statistically, those noise terms vanish as $W_l^m(k)$ and $W_l^m(k+1)$ are assumed to be independent and $\mathbb{E}[W_l^m(k)] = 0$ where $\mathbb{E}$ denotes expectation. However, practical realization for this averaging is not easy especially for very low SNR values and limited number of sub-carriers to average over. It is expected to have a degraded performance at very low SNR values. The other limitation is the complexity since flat correlations for the whole set of 504 involve numerous computations. For instance, since the sequence length is 132 samples, then $132 \times 504 \simeq 67K$ multiply-accumulate operations are required. However, the throughput of these operations is low since they repeat at least every 10msec which is half the periodicity of the NSSS sequences.

Again, to encourage noise rejection and to improve performance at very low SNR values,

the final decision statistic, $\bar{\Lambda}(i)$, is obtained by averaging the correlation over M consecutive windows such that $\bar{\Lambda}(i) = \frac{1}{M}\sum_{m=0}^{M-1}\Lambda_m(i)$. The estimated cell ID is then evaluated as, $\widehat{N}_{ID}^{Ncell} = \arg\max_{i\in[0,503]}\left|\bar{\Lambda}(i)\right|$. To obtain the best gain, averaging has to be careful about which windows to average so that they have the same possible θ_f. Fortunately, divide and conquer can be applied to reduce the number of multiplications to its one-fourth and hence reduce the complexity. The idea is that for every 4 cell IDs, there will a single root ZC sequence while the cells are differentiated according to the complementary sequences. Thus, computing the correlation can be divided into two sequential processes. During multiplication process, only ZC sequence is utilized to represent the reference NSSS. Next, accumulation is evaluated four times for each ZC sequence, where each complementary sequence is employed as weighting factors before applying the accumulation. Further optimization is possible by identifying the portions of the complementary sequences that are shared among multiple complementary sequences. This could save repeating the same accumulation for this portion again.

6.6.3 Simulation Results

To evaluate the performance of the presented procedure, the baseband downlink NB-IoT system has been simulated assuming a sampling rate of 1.92 MHz, 128-point FFT, 15kHz sub-carrier spacing, one antenna at transmitter and receiver. AWGN and EPA-5 standard channels were simulated. Simulations were performed over 10^4 sub-frames over independent channel realizations for the SNR range $[-16, 0]$ dBs. The frequency offset is assumed to be 17.5KHz.

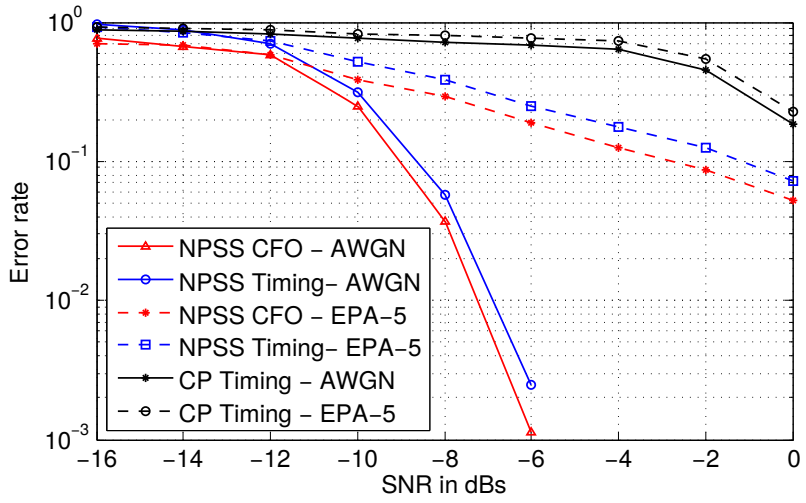

Figure 6.9: Estimation error for the subframe timing and integer CFO versus SNR under different channel conditions. No averaging is applied.

Fig. 6.9 shows the performance of the NPSS detection algorithm in comparison to the CP ML approach for various channel conditions. To guarantee no inter-carrier interference, a timing error is assumed if the estimated timing deviates from the true timing by half of the CP length. It is clear that, the performance of the ML estimator does not perform well at low SNR and it is moving very slowly. The idea is that with no further averaging, CP correlations are sensitive to the fading conditions and the short CP length. On the other hand, acquisition based on the NPSS has a superior performance which reflects the deserved complexity increase. However, introducing fading channel degrades the performance and averaging is required.

By changing the averaging period and accounting for different observation window periods for ML CP correlation and NPSS approach, Fig. 6.10 shows the performance for the two techniques versus the processing time for different channel conditions and SNR values. It is quite obvious that averaging across windows improves the performance on the account of the required processing time. Indeed, for a fixed target performance, the NPSS algorithm converges quickly to the proper timing and frequency offset unlike the CP correlation which is still moving slowly due to the insufficient number of CP samples and fading sensitivity. Thus, the effect of the fading channel can be absorbed by increasing the averaging period since NPSS is able to achieve the target performance independent of the channel conditions.

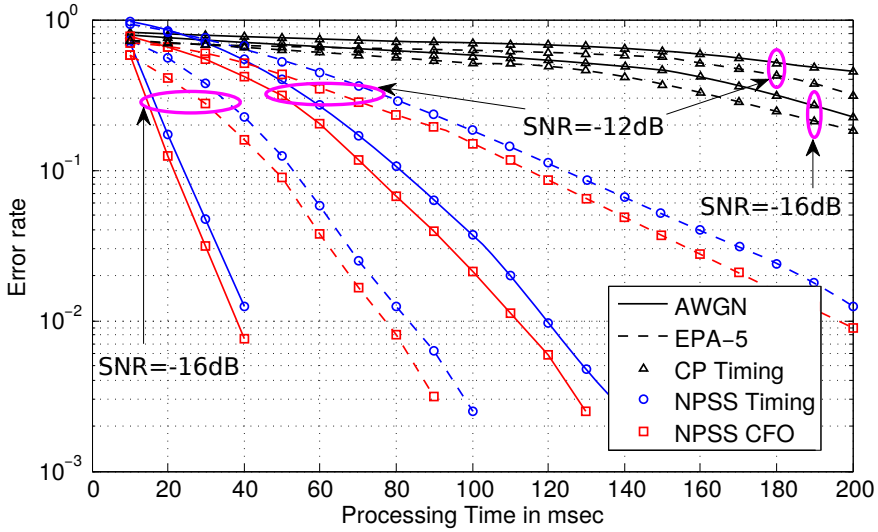

Figure 6.10: Estimation error for the subframe timing and integer CFO versus processing time under different channel conditions. SNR of -16 and -12dBs are considered.

To evaluate the cell search, in addition of simulating the presented differential-based detection approach, we have considered a benchmark scenario in which the reference NSSS sequence is cross-correlated with the received NSSS after applying channel equalization. Perfect CSI is assumed to be known at the UE side. In fact, this is a hypothetical scenario that emulates the ideal system conditions. Fig. 6.11 shows the detection accuracy of the cell detection after timing and frequency acquisition. Different averaging intervals are employed for various SNR values. It is clear that the differential approach is away from the perfect one when no averaging is employed. However, the performance is significantly improved by introducing longer averaging periods even for fading conditions.

6.7 Conclusion

In this chapter, we addressed couple of challenges and issues related to the LTE-based cellular M2M communication. First, we presented the enhancements provided by LTE Release-13 to support future MTC operation. Initial synchronization and cell search have new challenges for LTE-MTC systems and need to be revised. We studied the conventional solutions including timing acquisition, cell search, and initial CFO estimation algorithms for non LTE-MTC

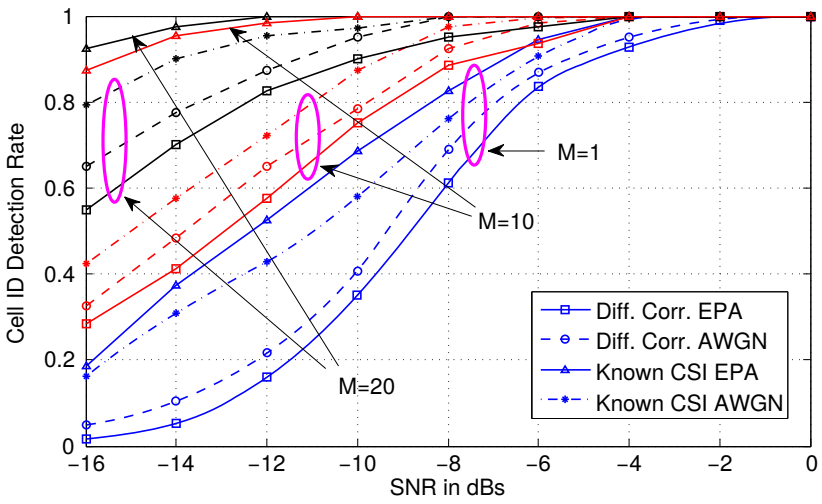

Figure 6.11: Cell search detection accuracy versus SNR. Averaging is employed such that $M \in \{1, 10, 20\}$. AWGN and EPA-5 are considered.

systems. Modifications to these algorithms are proposed and evaluated by computer simulations. By employing the time averaging for various decision statistics, the performance of various algorithms is enhanced on the account of the processing time. We evaluate different algorithms from processing time perspective to help select a solution for the future LTE-MTC design.

Second, we addressed the problem of frequency tracking to estimate the residual frequency error in LTE-MTC systems. We proposed a frequency tracking algorithm that utilizes the new repetitive feature of the broadcast channel symbols. We evaluated the performance of the presented algorithm for various SNR values, channel conditions, and processing times. When compared to conventional approaches, in addition to the substantial performance enhancement noticed from the results, the proposed algorithm can quickly lock the UE to the network under very low SNRs and in different fading environments. Finally, we presented a cell search and initial synchronization algorithm for NB-IoT systems that utilizes the new set of synchronization signals (i.e., NPSS and NSSS). Timing acquisition and initial CFO estimation are jointly acquired through time domain NPSS correlation. The cell ID is captured by differential frequency domain NSSS correlations. The proposed algorithm can quickly lock the UE to the network under very low SNRs and in different fading environments.

Chapter 7

Conclusions and Future Work

7.1 Conclusions

Interweave cognitive radio systems are being investigated to solve the problems resulting from the bandwidth scarcity and the spectrum usage inefficiency by exploiting the existing licensed spectrum opportunistically. Wireless systems, equipped with the substantial capabilities of CR, will provide an ultimate spectrum-aware communication model in wireless networks. Furthermore, CR concept can be employed to facilitate the reduced-cost realization for next generation M2M cellular networks including future LTE-MTC and LTE-based NB-IoT systems. In this thesis, we have tackled a major thrust of research in the CR area and M2M physical implementation, namely narrowband spectrum monitoring, low power wideband spectrum sensing, synchronization and cell detection for LTE-based M2M communications. We have made significant contributions, which is evident from the track record of publications that resulted from this research. Below, we briefly summarize those accomplishments.

As introduced in Chapter 3, we investigated the possibility of solving the massive increase in the number of connected devices for cellular M2M communications by involving the interweave cognitive radio model. In that sense, the base station is defined to be smart so that it can overlay the less priority machines to the cognitive band. Smart eNodeB should be able to handle the cognition part of the solution as well as the typical behaviour for LTE system. Various network models to support next generation MTC have been discussed including the heterogeneous network model and cellular model. Implementation aspects for the future devices including low-power and low-cost features have been considered. Based on this proposal, we addressed practical implementation issues for the current CR networks. This

mainly includes the low cognitive radio network throughput due the quiet period scheduling. Also, the power consumption problem attached to the wideband sensing due to the ultra high sampling rate. Furthermore, we studied the recent advances in LTE systems to include both MTC and NB-IoT categories. We provided algorithmic solutions for the initial synchronization and cell search for both categories. Also, we addressed the frequency tracking issue for MTC systems and we presented an algorithm to operate at the introduced harsh environment with respect to low SNR and fading conditions.

While we considered the challenges of interweave cognitive radio in Chapter 3, the low throughput issue for the cognitive radio network arises due to the utilization of the quiet periods. Also, power consumption for the wideband sensing is noticed due to the ultra high sampling rates. First, in Chapter 4, we considered a novel spectrum monitoring algorithm that is designed for OFDM systems. The *energy ratio* algorithm can detect the activity of the primary user during the secondary user transmission by monitoring the signal strength variations over some reserved tones. We derived the ROC in order to analyze the performance of the proposed algorithm. Simulation results indicate that the detection performance is superior than the receiver statistics method. Also over inter-carrier interference effect due to CFO and SFO, the *energy ratio* algorithm offers good performance. As a result, our proposed spectrum monitoring algorithm can greatly improve the OFDM-based cognitive radio network throughput by enhancing the spectrum monitoring performance during SU transmission with a very limited reduction in the secondary network throughput.

In Chapter 5, we presented two architectures for wideband spectrum sensing in interweave cognitive radio networks. For both techniques, the ultimate goal is to extremely reduce the power consumption and complexity by employing the smallest allowed ADC precision (i.e., 1-bit ADC). The first architecture is an update for the classical FFT-based energy detector, where the 1-bit quantizer replaces the high-precision ADC. Furthermore, to preserve the total power at the receiver side, the RF is assumed to provide the estimated RSSI, of course within a tolerance. In this piece of work, we have derived the exact performance for the frequency domain energy detector in order to relax the infinite precision and large averaging assumptions. We have also discussed the impact of the introduced aggressive quantization. Results show promising detection capabilities for various RSSI tolerances.

The other solution relies on evaluating the window-based autocorrelation for the received quantized signal. In this regard, we have derived the closed form expression for the window-based autocorrelation function which clearly shows the spectrum occupancy. We presented a detection algorithm that employs the average PSD to discriminate between vacant and occupied sub-bands. Simulation results indicate that the detection accuracy is promising for sparse systems. As a result, our presented solutions can greatly enhance the complexity, power consumption, and the performance for the wideband spectrum sensing problem.

Chapter 6 considers the contribution in the direction of LTE-MTC and LTE-based NB-IoT systems. Although there are many implementation issues for the new systems due to the introduced harsh environment which includes ultra low SNR requirements under fading conditions in addition to the RF impairments. Our focus is directed to the initial synchronization, cell search, and frequency tracking for LTE-MTC systems. In this direction, we have evaluated the classical initial synchronization and cell search algorithms for the conventional LTE systems in the LTE-MTC framework. Applying time averaging over all techniques can enhance the performance under low SNR regimes with reasonable increase in the complexity. For the frequency tracking, we have presented an algorithm to track the frequency errors due to fading or residual offsets resulting from the initial synchronization process. This technique relies on the repetitive nature of the modified broadcast channel for LTE-MTC systems. The frequency estimation is applied by measuring the differential phase of the repeated symbols. Averaging over multiple repetition patterns enhances the estimation accuracy. For NB-IoT systems, new synchronization signals have been introduced and hence new techniques have to be developed in order to apply initial synchronization and cell search. The new synchronization signals, namely NPSS and NSSS, span complete subframes. NPSS does not include any information about the cell but it is mainly used for timing acquisition on both the symbol level and frame boundaries. On the other hand, NSSS carries the full information about the cell ID. In this front, we have presented two algorithms that rely on the TD correlation for NPSS and FD correlation for NSSS in order to capture the timing and the initial frequency offset, and to acquire the cell ID. Results show that the presented techniques can not only be efficient from the performance perspective, but also they can provide reasonable complexity.

7.2 Future Work

In our research, we have utilized the *energy ratio* algorithm to detect the reappearance of the PU from a reserved tone sequence in OFDM system. The system has been investigated over some RF impairment including CFO, SFO, and NBI. However, there are still other impairments such as phase noise and IQ imbalance that can be considered as a future extension. Furthermore, we assumed typical fading channels such as a frequency selective channel, however this can be extended to other general fading channels such as Nakagami channels.

Indeed, we feel that the *energy ratio* algorithm can be utilized to tackle couple of other problems in cognitive radio networks such as detecting the power boosting of a PU in spectrum sharing network. Actually, one problem for SU in spectrum sharing networks is that PU always changes its nominal power according to power control mechanism. Accordingly there should be a method to track this power change from the SU perspective in order to adjust its interference threshold.

For the FFT-based 1-bit quantizer architecture, we have assumed the coordination between PUs so that the power is almost uniformly distributed over the wideband. However, this assumption may not be possible in some scenarios. Hence, a relaxation to this assumption is considered as another direction of research. Moreover, analytical derivations for the power distribution constant might be part of this future work.

For the 1-bit quantizer system based on autocorrelation, the detection is a function of the system sparsity which varies with time. A more sophisticated detection algorithm is required to post process the estimated PSD. In this case, the relation between the allocated bands, possibly through a random variable, will be a key factor in the design of this sub-optimal detector. This has not been tackled yet.

In the direction of LTE-MTC and NB-IoT systems, we have investigated a single cell detection. Thus, multi-cell search is a direct extension to this work. Indeed, there are numerous challenges that would require the research effort. For example, coherent detection can be applied only when channel estimates are available. Estimating the channel at this low SNR with high Doppler spreading is a real challenge especially with the introduction of the frequency hopping. Furthermore, the current techniques for soft combining, control

channel detection, and channel quality measurements have to be revised based on the MTC requirements. Last but not least, the time tracking and frequency tracking loops for NB-IoT become a challenge due to the insufficient number of pilots for the extremely low bandwidth.

Appendix A

Proof of the Correlation Function For One-Bit Quantizer System

In this appendix, we provide an analysis for the proposed autocorrelation-based wideband sensing. Throughout the analysis, we assume that the signal to be detected does not have any known structure that could be exploited. Therefore, a PU signal is modelled via a zero-mean circularly symmetric complex Gaussian distribution as presented in Section 5.2. The target of this analysis is to find closed form expressions for the statistical autocorrelation function in case of the one-bit quantized system. We start by evaluating the covariance matrix between various signal components for two samples of the non-quantized received signal. Then, the effect of quantization is explored and reflected on the covariance matrix.

A.1 Covariance Matrix Evaluation

To develop the autocorrelation of the quantized signal, we start by evaluating the covariance between various signal components for the non-quantized signal. Let us define $z_1 = r(n) = X_1 + \mathbf{j}Y_1$ and $z_2 = r(n+k) = X_2 + \mathbf{j}Y_2$. It is known that the real and imaginary parts of the complex envelop signal $r(n)$ are independent as they form a circularly symmetric complex Gaussian distribution. Therefore, we do not need to prove that $\mathbb{E}[X_1Y_1] = \mathbb{E}[X_2Y_2] = 0$. Further, the signal components carry the same power level, therefore $\mathbb{E}[X_1X_1] = \mathbb{E}[Y_1Y_1] = \sum_{m=1}^{M} \sigma_m^2/2 + N\sigma_W^2/2$. The covariance matrix for the four real random variables X_1, Y_1, X_2, and Y_2 can be obtained if we find only $\mathbb{E}[X_1X_1]$, $\mathbb{E}[X_1X_2]$, and $\mathbb{E}[X_1Y_2]$ since it has been shown in [149] that $\mathbb{E}[X_mX_l] = \mathbb{E}[Y_mY_l]$ and $\mathbb{E}[X_mY_l] = -\mathbb{E}[X_lY_m]$ for any $l \neq m$.

$$
\begin{aligned}
\mathbb{E}[X_1X_2] &= \mathbb{E}\Bigg[\Big(\sum_{m=1}^{M} A^m_{\lfloor(n-\varepsilon_m)/N\rfloor}\cos\big(2\pi(n-\varepsilon_m)f_m/F_s\big) - B^m_{\lfloor(n-\varepsilon_m)/N\rfloor}\sin\big(2\pi(n-\varepsilon_m)f_m/F_s\big)\Big) \\
&\quad \Big(\sum_{l=1}^{M} A^l_{\lfloor(n-\varepsilon_l+k)/N\rfloor}\cos\big(2\pi(n-\varepsilon_l+k)f_l/F_s\big) - B^l_{\lfloor(n-\varepsilon_l+k)/N\rfloor}\sin\big(2\pi(n-\varepsilon_l+k)f_l/F_s\big)\Big)\Bigg] \\
&\quad +\mathbb{E}\Big[w_I(n)w_I(n+k)\Big] \\
&= \frac{1}{2}\sum_{m=1}^{M}\mathbb{E}\Big[A^m_{\lfloor(n-\varepsilon_m)/N\rfloor}A^m_{\lfloor(n-\varepsilon_m+k)/N\rfloor}\Big(\cos\big(2\pi k f_m/F_s\big)+\cos\big(4\pi(n-\varepsilon_m+0.5k)f_m/F_s\big)\Big)\Big] \\
&\quad +\frac{1}{2}\sum_{m=1}^{M}\mathbb{E}\Big[B^m_{\lfloor(n-\varepsilon_m)/N\rfloor}B^m_{\lfloor(n-\varepsilon_m+k)/N\rfloor}\Big(\cos\big(2\pi k f_m/F_s\big)-\cos\big(4\pi(n-\varepsilon_m+0.5k)f_m/F_s\big)\Big)\Big] \\
&\quad +\frac{N\sigma_W^2}{2}\delta(k) \\
&= \sum_{m=1}^{M}\Big[\mathbb{E}\big[A^m_{-1}A^m_{-1}\big]P\big[n+k<\varepsilon_m<N\big]+\mathbb{E}\big[A^m_0A^m_0\big]P\big[0<\varepsilon_m<n\big] \\
&\quad +\mathbb{E}\big[A^m_{-1}A^m_0\big]P\big[n<\varepsilon_m<n+k\big]\Big]\cos\big(2\pi k f_m/F_s\big)+\frac{N\sigma_W^2}{2}\delta(k) \\
&= \sum_{m=1}^{M}\Big[\frac{\sigma_m^2}{2}\Big(1-\frac{n+k}{N}\Big)+\frac{\sigma_m^2}{2}\frac{n}{N}\Big]\cos\big(2\pi k f_m/F_s\big)+\frac{N\sigma_W^2}{2}\delta(k) \\
&= \frac{M\sigma_W^2}{2}\Big[\frac{1}{M}\Big(1-\frac{k}{N}\Big)\sum_{m=1}^{M}\gamma_m\cos\Big(2\pi k f_m/F_s\Big)\Big]+\frac{N\sigma_W^2}{2}\delta(k) = \frac{\sigma_W^2}{2}\Big[M\eta_k+N\delta(k)\Big] \qquad \text{(A.1)}
\end{aligned}
$$

As a first step and by utilizing the definition for $r(n)$ given by (5.3), the cross-correlation between the real parts can be given by (A.1) where we have used the facts that:

- A_m, B_m, and ε_m are independent.
- A_m and A_l are independent as long as $m \neq l$.
- $A_m \sim \mathcal{N}(0, \sigma_m^2/2)$ and also $B_m \sim \mathcal{N}(0, \sigma_m^2/2)$.
- ε_m is uniformly distributed within the range $[0,\ N-1]$.
- Noise components are independent such that $w_I(n) \sim \mathcal{N}(0, N\sigma_W^2/2)$ and $w_Q(n) \sim \mathcal{N}(0, N\sigma_W^2/2)$.
- The noise is independent on A_m, B_m, and ε_m.
- $\gamma_m = \sigma_m^2/\sigma_W^2$ is the signal-to-noise-ratio per sub-band.

Similarly, the cross-correlation between X_1 and Y_2 can be obtained by,

$$
\mathbb{E}[X_1Y_2] = \frac{\sigma_W^2}{2}\Bigg[\Big(1-\frac{k}{N}\Big)\sum_{m=1}^{M}\gamma_m\sin\Big(2\pi k f_m/F_s\Big)\Bigg] = \frac{M\sigma_W^2}{2}\zeta_k, \quad 0\le k<N \qquad \text{(A.2)}
$$

where we have defined,

$$\eta_k = \frac{1}{M}\left(1-\frac{k}{N}\right)\sum_{m=1}^{M}\gamma_m \cos\left(2\pi f_m k/F_s\right) \tag{A.3}$$

$$\zeta_k = \frac{1}{M}\left(1-\frac{k}{N}\right)\sum_{m=1}^{M}\gamma_m \sin\left(2\pi f_m k/F_s\right). \tag{A.4}$$

In fact, the parameters η_k and ζ_k reflect the information of the spectrum occupancy. To study the statistical properties of the autocorrelation function, the cross-correlation between every two random variables has to be obtained. The objective is to utilize those cross-correlations to derive the autocorrelation function when quantization takes place. Let us define $\mathbf{w} = [X_1\ Y_1\ X_2\ Y_2]^T$ to be a real vector. Cross-correlation between every two random variables can be obtained by just deriving the covariance matrix of $\mathbf{w}$. By using the facts that $\mathbb{E}[Y_1Y_2] = \mathbb{E}[X_1X_2]$ and $\mathbb{E}[X_2Y_1] = -\mathbb{E}[X_1Y_2]$ as derived in [149], we can write the covariance matrix of $\mathbf{w}$ as given by (A.5). It is clear that the matrix is a function of the spectrum occupancy as well as other system parameters such as N, M, σ_m^2, and σ_W^2.

A.2 Quantization Effect

Let X_{1q} and X_{2q} be the quantized versions of the two samples X_1 and X_2, respectively. Further, let Y_{1q} and Y_{2q} be the quantized versions of the two samples Y_1 and Y_2, respectively. Recall that we only study the effect of the aggressive quantization in which each variable is quantized to a single bit. The quantized version for any of these random variables can only take a value of either +1 or -1 such that $X_{1q} = sgn(X_1)$, $X_{2q} = sgn(X_2)$, $Y_{1q} = sgn(Y_1)$, $Y_{2q} = sgn(Y_2)$, and sgn denotes the well-known signum sign function. The autocorrelation of the quantized version of the received signal $r(n)$ is given by (A.6) where $r_q(n) = X_{1q} + \mathbf{j}Y_{1q}$ and $r_q(n+k) = X_{2q} + \mathbf{j}Y_{2q}$.

$$\mathbb{E}[\mathbf{w}\mathbf{w}^T] = \frac{\sigma_W^2}{2}\begin{bmatrix} N+\sum_{m=1}^{M}\gamma_m & 0 & M\eta_k+N\delta(k) & M\zeta_k \\ 0 & N+\sum_{m=1}^{M}\gamma_m & -M\zeta_k & M\eta_k+N\delta(k) \\ M\eta_k+N\delta(k) & -M\zeta_k & N+\sum_{m=1}^{M}\gamma_m & 0 \\ M\zeta_k & M\eta_k+N\delta(k) & 0 & N+\sum_{m=1}^{M}\gamma_m \end{bmatrix} \tag{A.5}$$

$$\mathcal{R}(k) \;=\; \mathbb{E}[r_q^*(n) r_q(n+k)] = \mathbb{E}[X_{1q}X_{2q}] + \mathbb{E}[Y_{1q}Y_{2q}] + \mathbf{j}\mathbb{E}[X_{1q}Y_{2q}] - \mathbf{j}\mathbb{E}[X_{2q}Y_{1q}] \quad \text{(A.6)}$$

In reality, each pair of the underlying random variables are jointly Gaussian as they are simply samples of a stationary Gaussian process. Correspondingly, the correlation coefficient can be defined for any pair. For example, the correlation coefficient between X_1 and X_2 is given by (A.7), where $\bar{\gamma} = \frac{1}{M}\sum_{m=1}^{M}\gamma_m$ is the average primary signal power. Here, we have utilized the covariance matrix results defined by (A.5) to write closed form expressions for the cross-correlation between X_1 and X_2 and also to define the variances for both X_1 and X_2. Furthermore, we have defined $\beta = M/N$ to represent the fraction of the occupied sub-bands or simply the spectrum utilization.

$$\rho_{X_1X_2} \;=\; \frac{\mathbb{E}[X_1X_2]}{\sqrt{\mathbb{E}[X_1X_1]\mathbb{E}[X_2X_2]}} = \frac{M\eta_k + N\delta(k)}{N + \sum_{m=1}^{M}\gamma_m} = \frac{\delta(k) + \beta\eta_k}{1 + \beta\bar{\gamma}} \quad \text{(A.7)}$$

To find the probability mass function for the correlation of the quantized version of the signal $r(n)$, one needs to evaluate four probabilities for the four quadrants. Since both random variables have zero mean and common variance, then the probabilities can be directly evaluated [150]. The joint probability mass function of X_{1q} and X_{2q} can be summarized by Table A.1. The correlation between the quantized two samples can be then obtained by (A.8).

$$\begin{aligned}\mathbb{E}[X_{1q}X_{2q}] \;&=\; 2P[X_1 \geq 0,\, X_2 \geq 0] - 2P[X_1 \geq 0,\, X_2 \leq 0] \\ &=\; \frac{2}{\pi}\sin^{-1}\left(\frac{\delta(k) + \beta\eta_k}{1 + \beta\bar{\gamma}}\right)\end{aligned} \quad \text{(A.8)}$$

Table A.1: PMF for the quantized samples for X_1 and X_2

X_{1q}	X_{2q}	$P[X_{1q} = x_{1q}, X_{2q} = x_{2q}]$
+1	+1	$P[X_1 \geq 0, X_2 \geq 0] = \frac{1}{4} + \frac{1}{2\pi}\sin^{-1}(\rho_{X_1X_2})$
-1	+1	$P[X_1 \leq 0, X_2 \geq 0] = \frac{1}{4} - \frac{1}{2\pi}\sin^{-1}(\rho_{X_1X_2})$
+1	-1	$P[X_1 \geq 0, X_2 \leq 0] = \frac{1}{4} - \frac{1}{2\pi}\sin^{-1}(\rho_{X_1X_2})$
-1	-1	$P[X_1 \leq 0, X_2 \leq 0] = \frac{1}{4} + \frac{1}{2\pi}\sin^{-1}(\rho_{X_1X_2})$

The same procedure can be applied for the remaining random variables. One can simply show that $\mathbb{E}[X_{1q}X_{2q}] = \mathbb{E}[Y_{1q}Y_{2q}]$ and $\mathbb{E}[X_{1q}Y_{2q}] = -\mathbb{E}[X_{2q}Y_{1q}]$. Further, closed form expressions for these quantities can be written as given by (A.9) and (A.10). Finally, the autocorrelation of the quantized signal can be derived as given by (A.11).

$$\mathbb{E}[X_{1q}X_{2q}] = \mathbb{E}[Y_{1q}Y_{2q}] = \frac{2}{\pi}\sin^{-1}\left(\frac{\delta(k) + \beta\eta_k}{1 + \beta\bar{\gamma}}\right) \tag{A.9}$$

$$\mathbb{E}[X_{1q}Y_{2q}] = -\mathbb{E}[X_{2q}Y_{1q}] = \frac{2}{\pi}\sin^{-1}\left(\frac{\beta\zeta_k}{1 + \beta\bar{\gamma}}\right) \tag{A.10}$$

$$\begin{aligned}\mathcal{R}(k) &= \mathbb{E}[r_q^*(n)r_q(n+k)] = \mathbb{E}[X_{1q}X_{2q}] + \mathbb{E}[Y_{1q}Y_{2q}] + \mathbf{j}\mathbb{E}[X_{1q}Y_{2q}] - \mathbf{j}\mathbb{E}[X_{2q}Y_{1q}] \\ &= \frac{4}{\pi}\left[\sin^{-1}\left(\frac{\delta(k) + \beta\eta_k}{1 + \beta\bar{\gamma}}\right) + \mathbf{j}\sin^{-1}\left(\frac{\beta\zeta_k}{1 + \beta\bar{\gamma}}\right)\right]\end{aligned} \tag{A.11}$$

References

[1] J. Wan, D. Li, C. Zou, and K. Zhou, "M2M Communications for Smart City: An Event-Based Architecture," in *IEEE International Conference on Computer and Information Technology (CIT)*, Oct 2012, pp. 895–900.

[2] S. Y. Lien, K. C. Chen, and Y. Lin, "Toward ubiquitous massive accesses in 3GPP machine-to-machine communications," *IEEE Communications Magazine*, vol. 49, no. 4, pp. 66–74, April 2011.

[3] T. Yucek and H. Arslan, "A survey of spectrum sensing algorithms for cognitive radio applications," *IEEE Communications Surveys Tutorials*, vol. 11, no. 1, pp. 116–130, 2009.

[4] I. F. Akyildiz, W. y. Lee, M. C. Vuran, and S. Mohanty, "A survey on spectrum management in cognitive radio networks," *IEEE Communications Magazine*, vol. 46, no. 4, pp. 40–48, April 2008.

[5] Y. Zeng, Y.-C. Liang, A. T. Hoang, and R. Zhang, "A review on spectrum sensing for cognitive radio: Challenges and solutions," *EURASIP J. Adv. Signal Process*, vol. 2010, pp. 1–15, Jan. 2010.

[6] J. Wang, M. Ghosh, and K. Challapali, "Emerging cognitive radio applications: A survey," *IEEE Communications Magazine*, vol. 49, no. 3, pp. 74–81, March 2011.

[7] A. Ali, W. Hamouda, and M. Uysal, "Next generation M2M cellular networks: challenges and practical considerations," *IEEE Communications Magazine*, vol. 53, no. 9, pp. 18–24, September 2015.

[8] A. Ali and W. Hamouda, "Advances on spectrum sensing for cognitive radio networks: Theory and applications," *IEEE Communications Surveys and Tutorials*, in second iteration of revisions.

[9] ——, "A multi-mode IFFT/FFT processor for IEEE 802.11ac: Design and implementation," *International Journal of Wireless Communications and Mobile Computing*, pp. 1–13, Nov 2015.

[10] ——, "A novel spectrum monitoring algorithm for OFDM-based cognitive radio networks," in *IEEE Global Communications Conference*, Dec 2015, pp. 1–6.

[11] ——, "Spectrum monitoring using energy ratio algorithm for OFDM-based cognitive radio networks," *IEEE Transactions on Wireless Communications*, vol. 14, no. 4, pp. 2257–2268, April 2015.

[12] ——, "METHODS AND SYSTEMS FOR COGNITIVE RADIO SPECTRUM MONITORING," *United States Patent*, filed on June 3rd, 2014.

[13] ——, "Low power wideband sensing for one-bit quantized cognitive radio systems," *IEEE Wireless Communications Letters*, vol. 5, no. 1, pp. 16–19, Feb 2016.

[14] ——, "A novel one-bit quantization design for correlation-based low-power wideband sensing," in *IEEE International Conference on Communications*, May 2016, pp. 1–6.

[15] ——, "Power efficient wideband spectrum sensing for cognitive radio systems," *IEEE Transactions on Vehicular Technology*, in second iteration of revisions.

[16] ——, "Cell search evaluation: A step towards the next generation LTE-MTC systems," in *IEEE Wireless Communications and Networking Conference*, April 2016, pp. 1–6, BEST PAPER AWARD.

[17] ——, "Employing broadcast channel for frequency tracking in lte-mtc systems," *IEEE Wireless Communications Letters*, vol. (to appear), no. 99, pp. 1–4, 2016.

[18] ——, "On the cell search and initial synchronization for NB-IoT LTE systems," *IEEE Wireless Communications Letters*, submitted.

[19] FCC, "Spectrum policy task force report," Federal Communications Commission, Tech. Rep. 02-155, Nov 2002.

[20] S. Haykin, "Cognitive radio: brain-empowered wireless communications," *IEEE Journal on Selected Areas in Communications*, vol. 23, no. 2, pp. 201–220, 2005.

[21] A. Ghosh and W. Hamouda, "Cross-Layer Antenna Selection and Channel Allocation for MIMO Cognitive Radios," *IEEE Transactions on Wireless Communications*, vol. 10, no. 11, pp. 3666–3674, November 2011.

[22] FCC, "Facilitating opportunities for flexible, efficient, and reliable spectrum use employing cognitive radio technologies," Federal Communications Commission, Tech. Rep. 03-108, Feb 2005.

[23] T. W. Ban, W. Choi, B. C. Jung, and D. K. Sung, "Multi-user diversity in a spectrum sharing system," *IEEE Trans. Wireless Communications*, vol. 8, no. 1, pp. 102–106, Jan. 2009.

[24] S. Srinivasa and S. Jafar, "The throughput potential of cognitive radio: A theoretical perspective," in *Fortieth Asilomar Conference (ACSSC) on Signals, Systems and Computers*, Nov-2006, pp. 221–225.

[25] P. M. N. Devroye and V. Tarokh, "Achievable rates in cognitive radio channels," *IEEE Transactions on Information Theory*, vol. 52, no. 5, pp. 1813–1827, May 2006.

[26] A. Jovicic and P. Viswanath, "Cognitive radio: An information-theoretic perspective," *IEEE Transactions on Information Theory*, vol. 55, no. 9, pp. 3945–3958, Sept. 2009.

[27] I. F. Akyildiz, W.-Y. Lee, M. C. Vuran, and S. Mohanty, "Next generation/dynamic spectrum access/cognitive radio wireless networks: A survey," *Elsevier Computer Networks*, vol. 50, no. 13, pp. 2127 – 2159, 2006.

[28] M. Masonta, M. Mzyece, and N. Ntlatlapa, "Spectrum decision in cognitive radio networks: A survey," *IEEE Communications Surveys Tutorials*, vol. 15, no. 3, pp. 1088–1107, 2013.

[29] E. Larsson and M. Skoglund, "Cognitive radio in a frequency-planned environment: some basic limits," *IEEE Transactions on Wireless Communications*, vol. 7, no. 12, pp. 4800–4806, 2008.

[30] H. Sun, A. Nallanathan, C.-X. Wang, and Y. Chen, "Wideband spectrum sensing for cognitive radio networks: a survey," *IEEE Wireless Communications*, vol. 20, no. 2, pp. 74–81, 2013.

[31] L. De Vito, "A review of wideband spectrum sensing methods for Cognitive Radios," in *IEEE International Instrumentation and Measurement Technology Conference*, May 2012, pp. 2257–2262.

[32] W. S. Jeon, D. G. Jeong, J. A. Han, G. Ko, and M. S. Song, "An efficient quiet period management scheme for cognitive radio systems," *IEEE Transactions on Wireless Communications*, vol. 7, no. 2, pp. 505–509, Feb. 2008.

[33] H. Chen, L. Liu, J. Matyjas, and M. Medley, "Optimal resource allocation for sensing based spectrum sharing cognitive radio networks," in *IEEE Global Communications Conference*, 2014, pp. 899–904.

[34] W. Hu, D. Willkomm, M. Abusubaih, J. Gross, G. Vlantis, M. Gerla, and A. Wolisz, "COGNITIVE RADIOS FOR DYNAMIC SPECTRUM ACCESS - Dynamic Frequency Hopping Communities for Efficient IEEE 802.22 Operation," *IEEE Communications Magazine*, vol. 45, no. 5, pp. 80–87, May 2007.

[35] D. Willkomm, M. Bohge, D. Hollos, J. Gross, and A. Wolisz, "Double Hopping: A new approach for Dynamic Frequency Hopping in Cognitive Radio networks," in *IEEE International Symposium on Personal, Indoor and Mobile Radio Communications*, Sept 2008, pp. 1–6.

[36] T. Ihalainen, A. Viholainen, T. Stitz, and M. Renfors, "Spectrum monitoring scheme for filter bank based cognitive radios," in *Future Network and Mobile Summit*, 2010, pp. 1–9.

[37] Y. Pei, Y.-C. Liang, K. Teh, and K. H. Li, "How much time is needed for wideband spectrum sensing?" *IEEE Transactions on Wireless Communications*, vol. 8, no. 11, pp. 5466–5471, 2009.

[38] E. Axell, G. Leus, E. Larsson, and H. Poor, "Spectrum Sensing for Cognitive Radio : State-of-the-Art and Recent Advances," *IEEE Signal Processing Magazine*, vol. 29, no. 3, pp. 101–116, 2012.

[39] S. M. Kay, *Fundamentals of Statistical Signal Processing: Detection Theory.* Prentice Hall, 1998.

[40] S. Kapoor, S. Rao, and G. Singh, "Opportunistic Spectrum Sensing by Employing Matched Filter in Cognitive Radio Network," in *International Conference on Communication Systems and Network Technologies*, 2011, pp. 580–583.

[41] D. Bhargavi and C. Murthy, "Performance comparison of energy, matched-filter and cyclostationarity-based spectrum sensing," in *IEEE International Workshop on Signal Processing Advances in Wireless Communications*, June 2010, pp. 1–5.

[42] A. Nasser, A. Mansour, K. Yao, H. Charara, and M. Chaitou, "Efficient spectrum sensing approaches based on waveform detection," in *International Conference on e-Technologies and Networks for Development*, April 2014, pp. 13–17.

[43] E. Axell and E. Larsson, "Optimal and Sub-Optimal Spectrum Sensing of OFDM Signals in Known and Unknown Noise Variance," *IEEE Journal on Selected Areas in Communications*, vol. 29, no. 2, pp. 290–304, February 2011.

[44] S. Chaudhari, V. Koivunen, and H. Poor, "Autocorrelation-Based Decentralized Sequential Detection of OFDM Signals in Cognitive Radios," *IEEE Transactions on Signal Processing*, vol. 57, no. 7, pp. 2690–2700, July 2009.

[45] J. Lunden, V. Koivunen, A. Huttunen, and H. Poor, "Collaborative Cyclostationary Spectrum Sensing for Cognitive Radio Systems," *IEEE Transactions on Signal Processing*, vol. 57, no. 11, pp. 4182–4195, Nov 2009.

[46] S. K. Sharma, S. Chatzinotas, and B. Ottersten, "Eigenvalue-based sensing and snr estimation for cognitive radio in presence of noise correlation," *IEEE Transactions on Vehicular Technology*, vol. 62, no. 8, pp. 3671–3684, Oct 2013.

[47] Y. Zeng and Y. C. Liang, "Eigenvalue-based spectrum sensing algorithms for cognitive radio," *IEEE Transactions on Communications*, vol. 57, no. 6, pp. 1784–1793, June 2009.

[48] D. Donoho, "Compressed sensing," *IEEE Transactions on Information Theory*, vol. 52, no. 4, pp. 1289–1306, April 2006.

[49] P. Feng and Y. Bresler, "Spectrum-blind minimum-rate sampling and reconstruction of multiband signals," in *IEEE International Conference on Acoustics, Speech, and Signal Processing*, vol. 3, May 1996, pp. 1688–1691.

[50] R. Venkataramani and Y. Bresler, "Perfect reconstruction formulas and bounds on aliasing error in sub-nyquist nonuniform sampling of multiband signals," *IEEE Transactions on Information Theory*, vol. 46, no. 6, pp. 2173–2183, 2000.

[51] Z. Quan, S. Cui, A. Sayed, and H. Poor, "Optimal Multiband Joint Detection for Spectrum Sensing in Cognitive Radio Networks," *IEEE Transactions on Signal Processing*, vol. 57, no. 3, pp. 1128–1140, March 2009.

[52] Z. Tian and G. Giannakis, "A wavelet approach to wideband spectrum sensing for cognitive radios," in *IEEE International Conference on Cognitive Radio Oriented Wireless Networks and Communications*, 2006, pp. 1–5.

[53] S. El-Khamy, M. El-Mahallawy, and E. Youssef, "Improve wideband spectrum sensing techniques using wavelet-based edge detection for cognitive radio," in *IEEE International Conference on Computing, Networking and Communications*, Jan 2013, pp. 28–31.

[54] B. Farhang-Boroujeny, "Filter bank spectrum sensing for cognitive radios," *IEEE Transactions on Signal Processing*, vol. 56, no. 5, pp. 1801–1811, May 2008.

[55] E. Candes and T. Tao, "Decoding by linear programming," *IEEE Transactions on Information Theory*, vol. 51, no. 12, pp. 4203–4215, Dec 2005.

[56] Z. Tian and G. Giannakis, "Compressed sensing for wideband cognitive radios," in *IEEE International Conference on Acoustics, Speech and Signal Processing*, vol. 4, 2007, pp. IV1357–IV1360.

[57] E. Candes, J. Romberg, and T. Tao, "Robust uncertainty principles: exact signal reconstruction from highly incomplete frequency information," *IEEE Transactions on Information Theory*, vol. 52, no. 2, pp. 489–509, Feb 2006.

[58] C. Luo and J. Mcclellan, "Discrete random sampling theory," in *IEEE International Conference on Acoustics, Speech and Signal Processing*, May 2013, pp. 5430–5434.

[59] E. Candes, M. Rudelson, T. Tao, and R. Vershynin, "Error correction via linear programming," in *IEEE Symposium on Foundations of Computer Science*, Oct 2005, pp. 668–681.

[60] S. S. Chen, D. L. Donoho, and M. A. Saunders, "Atomic decomposition by basis pursuit," *SIAM Journal on Scientific Computing*, vol. 20, no. 1, pp. 33–61, 1998.

[61] J. Tropp, J. Laska, M. Duarte, J. Romberg, and R. Baraniuk, "Beyond nyquist: Efficient sampling of sparse bandlimited signals," *IEEE Transactions on Information Theory*, vol. 56, no. 1, pp. 520–544, 2010.

[62] W. Sun, Z. Huang, F. Wang, and X. Wang, "Compressive wideband spectrum sensing based on single channel," *Electronics Letters*, vol. 51, no. 9, pp. 693–695, 2015.

[63] R. Yazicigil, T. Haque, M. Whalen, J. Yuan, J. Wright, and P. Kinget, "Wideband rapid interferer detector exploiting compressed sampling with a quadrature analog-to-information converter," *IEEE Journal of Solid-State Circuits*, vol. 50, no. 12, pp. 3047–3064, Dec 2015.

[64] H. Mahmoud, T. Yucek, and H. Arslan, "OFDM for cognitive radio: merits and challenges," *IEEE Wireless Communications*, vol. 16, no. 2, pp. 6–15, April 2009.

[65] T. Pollet, M. Van Bladel, and M. Moeneclaey, "BER sensitivity of OFDM systems to carrier frequency offset and wiener phase noise," *IEEE Transactions on Communications*, vol. 43, no. 234, pp. 191–193, 1995.

[66] C. Muschallik, "Influence of RF oscillators on an OFDM signal," *IEEE Transactions on Consumer Electronics*, vol. 41, no. 3, pp. 592–603, 1995.

[67] P.-Y. Tsai, H.-Y. Kang, and T.-D. Chiueh, "Joint weighted least-squares estimation of carrier-frequency offset and timing offset for OFDM systems over multipath fading channels," *IEEE Transactions on Vehicular Technology*, vol. 54, no. 1, pp. 211–223, 2005.

[68] T. Pollet, P. Spruyt, and M. Moeneclaey, "The BER performance of OFDM systems using non-synchronized sampling," in *IEEE Global Telecommunications Conference, GLOBECOM*, 1994, pp. 253–257.

[69] F. Capozzi, G. Piro, L. A. Grieco, G. Boggia, and P. Camarda, "Downlink packet scheduling in LTE cellular networks: Key design issues and a survey," *IEEE Communications Surveys Tutorials*, vol. 15, no. 2, pp. 678–700, Second 2013.

[70] M. Wang, J. Zhang, B. Ren, W. Yang, J. Zou, M. Hua, and X. You, "The Evolution of LTE Physical Layer Control Channels," *IEEE Communications Surveys Tutorials*, vol. 18, no. 2, pp. 1336–1354, Secondquarter 2016.

[71] J. Hu, M. Wang, K. Zou, K. Yang, M. Hua, and J. Zhang, "Enhanced LTE physical downlink control channel design for machine-type communications," in *International Conference on New Technologies, Mobility and Security*, July 2015, pp. 1–5.

[72] S. S. A. Abbas, S. J. Thiruvengadam, and N. A. R. Kumar, "Realization of receiver architectures using VLSI DSP techniques for broadcast channel in LTE," in *International Conference on Embedded Systems*, July 2014, pp. 12–17.

[73] P. Osti, P. Lassila, S. Aalto, A. Larmo, and T. Tirronen, "Analysis of PDCCH Performance for M2M Traffic in LTE," *IEEE Transactions on Vehicular Technology*, vol. 63, no. 9, pp. 4357–4371, Nov 2014.

[74] S. S. A. Abbas, P. A. J. Sheeba, and S. J. Thiruvengadam, "Design of downlink pdsch architecture for LTE using FPGA," in *International Conference on Recent Trends in Information Technology*, June 2011, pp. 947–952.

[75] J. Lorca, "Increasing coverage and maximum CFO in DFT-s-OFDM for Machine-Type Communications," in *International Conference on Communications*, 2015, pp. 982–987.

[76] D. Flore. (2015, Feb.) Evolution of LTE in Release 13. [Online]. Available: http://www.3gpp.org/news-events/3gpp-news/1628-rel13

[77] R. Ratasuk, A. Prasad, Z. Li, A. Ghosh, and M. Uusitalo, "Recent advancements in M2M communications in 4G networks and evolution towards 5G," in *International Conference on Intelligence in Next Generation Networks*, 2015, pp. 52–57.

[78] Ericsson, "RAN1 agreements for Rel-13 eMTC sorted and edited by topic," Tech. Rep. R1-157733, Nov 2015, 3GPP TSG RAN WG1 Meeting-83. [Online]. Available: http://www.3gpp.org/DynaReport/TDocExMtg--R1-83--31259.htm

[79] "LTE-M-Optimizing LTE for the Internet of Things," White Paper, Nokia Networks, Aug. 2015.

[80] Y. Tsai, G. Zhang, D. Grieco, and F. Ozluturk, "Cell search in 3GPP long term evolution systems," *IEEE Vehicular Technology Magazine*, vol. 2, no. 2, pp. 23–29, 2007.

[81] I. Kim, Y. Han, and H. K. Chung, "An efficient synchronization signal structure for OFDM-based cellular systems," *IEEE Transactions on Wireless Communications*, vol. 9, no. 1, pp. 99–105, 2010.

[82] P. Annamalai, S. Das, J. Bapat, and D. Das, "Coverage enhancement of PBCH using reduced search Viterbi for MTC in LTE-Advanced networks," in *International Symposium on Modeling and Optimization in Mobile, Ad Hoc, and Wireless Networks*, May 2015, pp. 110–114.

[83] J. Gozalvez, "New 3GPP Standard for IoT [Mobile Radio]," *IEEE Vehicular Technology Magazine*, vol. 11, no. 1, pp. 14–20, March 2016.

[84] Ericsson, "Introduction of NB-IoT," 3GPP TSG RAN WG1 Meeting-85, Tech. Rep. R1-165971, May 2016.

[85] Huawei and HiSilicon, "Introduction of Rel-13 feature of NB-IoT in 36.212," 3GPP TSG RAN WG1 Meeting-85, Tech. Rep. R1-166045, May 2016.

[86] Motorola Mobility, "Introduction of NB-IoT," 3GPP TSG RAN WG1 Meeting-85, Tech. Rep. R1-165111, May 2016.

[87] J. Bradley, J. Barbier, and D. Handler, "Embracing the internet of everything to capture your share of $14.4 trillion," White Paper, Cisco, July 2013, viewed on July 20, 2016 http://www.cisco.com/web/about/ac79/docs/innov/IoE_Economy.pdf.

[88] A. Damnjanovic, J. Montojo, Y. Wei, T. Ji, T. Luo, M. Vajapeyam, T. Yoo, O. Song, and D. Malladi, "A survey on 3GPP heterogeneous networks," *IEEE Wireless Communications*, vol. 18, no. 3, pp. 10–21, June 2011.

[89] C. A. Haro and M. Dohler, *Machine-to-Machine (M2M) Communications: Architecture, Performance and Applications (Google eBook)*. Elsevier, Dec 2014.

[90] 3GPP, "Standarization of Machine-type Communications," 3rd Generation Partnership Project, Tech. Rep. V0.2.4, June 2014.

[91] J. Swetina, G. Lu, P. Jacobs, F. Ennesser, and J. Song, "Toward a standardized common M2M service layer platform: Introduction to oneM2M," *IEEE Wireless Communications*, vol. 21, no. 3, pp. 20–26, June 2014.

[92] A. Pyattaev, K. Johnsson, S. Andreev, and Y. Koucheryavy, "3GPP LTE traffic offloading onto WiFi Direct," in *IEEE Wireless Communications and Networking Conference Workshops*, April 2013, pp. 135–140.

[93] B. Wang and K. Liu, "Advances in cognitive radio networks: A survey," *IEEE Journal of Selected Topics in Signal Processing*, vol. 5, no. 1, pp. 5–23, Feb 2011.

[94] S. Y. Lien, S. M. Cheng, S. Y. Shih, and K. C. Chen, "Radio Resource Management for QoS Guarantees in Cyber-Physical Systems," *IEEE Transactions on Parallel and Distributed Systems*, vol. 23, no. 9, pp. 1752–1761, Sept 2012.

[95] I. F. Akyildiz, B. F. Lo, and R. Balakrishnan, "Cooperative Spectrum Sensing in Cognitive Radio Networks: A Survey," *Phys. Commun.*, vol. 4, no. 1, pp. 40–62, Mar. 2011.

[96] K. Letaief and W. Zhang, "Cooperative Communications for Cognitive Radio Networks," *Proceedings of the IEEE*, vol. 97, no. 5, pp. 878–893, May 2009.

[97] T. Yucek and H. Arslan, "A survey of spectrum sensing algorithms for cognitive radio applications," *IEEE Communications Surveys and Tutorials*, vol. 11, no. 1, pp. 116–130, First 2009.

[98] S. H. Hwang and M. J. Rim, "Adaptive operation scheme for quiet period in IEEE 802.22 system," in *International Conference on ICT Convergence (ICTC)*, Sept. 2011, pp. 482–484.

[99] D. Cabric, S. M. Mishra, and R. W. Brodersen, "Implementation issues in spectrum sensing for cognitive radios," in *Conference Record of the Thirty-Eighth Asilomar Conference on Signals, Systems and Computers*, vol. 1, Nov. 2004, pp. 772–776.

[100] S. W. Boyd, J. M. Frye, M. B. Pursley, and T. C. Royster, "Spectrum monitoring during reception in dynamic spectrum access cognitive radio networks," *IEEE Transactions on Communications*, vol. 60, no. 2, pp. 547–558, Feb. 2012.

[101] T. Ihalainen, A. Viholainen, T. Stitz, and M. Renfors, "Spectrum monitoring scheme for filter bank based cognitive radios," in *Future Network and Mobile Summit*, June 2010, pp. 1–9.

[102] D. Galda and H. Rohling, "Narrow band interference reduction in ofdm based power line communication systems," in *Proc. of IEEE International Symp. on Power Line Commun. and its Appl. (ISPLC)*, Apr. 2001, pp. 345–351.

[103] S. Brandes, I. Cosovic, and M. Schnell, "Reduction of out-of-band radiation in ofdm systems by insertion of cancellation carriers," *IEEE Communications Letters*, vol. 10, no. 6, pp. 420–422, June 2006.

[104] M. Ma, X. Huang, B. Jiao, and Y. Guo, "Optimal orthogonal precoding for power leakage suppression in DFT-based systems," *IEEE Transactions on Communications*, vol. 59, no. 3, pp. 844–853, 2011.

[105] D. Zhang, P. Fan, and Z. Cao, "Receiver window design for narrowband interference suppression in ieee 802.11a system," in *Joint Conference of the 10th Asia-Pacific Conference on Communications and 5th International Symposium on Multi-Dimensional Mobile Communications Proceedings*, vol. 2, Sept. 2004, pp. 839–842.

[106] T.-D. Chiueh and P.-Y. Tsai, *OFDM Baseband Receiver Design for Wireless Communications*. Wiley, 2007.

[107] J. Rinne, "An equalization method using preliminary decisions for orthogonal frequency division multiplexing systems in channels with frequency selective fading," in *IEEE Vehicular Technology Conference, Mobile Technology for the Human Race*, vol. 3, 1996, pp. 1579–1583.

[108] M. Xu, H. Li, and X. Gan, "Energy Efficient Sequential Sensing for Wideband Multi-Channel Cognitive Network," in *International Conference on Communications*, June 2011, pp. 1–5.

[109] H. Chen, C. Tse, and F. Zhao, "Optimal quantisation bit budget for a spectrum sensing scheme in bandwidth-constrained cognitive sensor networks," *Wireless Sensor Systems, IET*, vol. 1, no. 3, pp. 144–150, September 2011.

[110] H. Sun, A. Nallanathan, C.-X. Wang, and Y. Chen, "Wideband spectrum sensing for cognitive radio networks: a survey," *IEEE Wireless Communications*, vol. 20, no. 2, pp. 74–81, April 2013.

[111] D. Liu, C. Li, J. Liu, and K. Long, "A Novel Signal Separation Algorithm for Wideband Spectrum Sensing in Cognitive Networks," in *IEEE Global Telecommunications Conference*, Dec 2010, pp. 1–6.

[112] T.-H. Yu, S. Rodriguez-Parera, D. Markovic, and D. Cabric, "Cognitive Radio Wideband Spectrum Sensing Using Multitap Windowing and Power Detection with Thresh-

old Adaptation," in *IEEE International Conference on Communications*, May 2010, pp. 1–6.

[113] R. Sarvendranath and N. B. Mehta, "Antenna Selection with Power Adaptation in Interference-Constrained Cognitive Radios," *IEEE Transactions Communications*, vol. 62, no. 3, pp. 786–796, March 2014.

[114] Y.-C. Liang, Y. Zeng, E. Peh, and A. T. Hoang, "Sensing-Throughput Tradeoff for Cognitive Radio Networks," *IEEE Transactions on Wireless Communications*, vol. 7, no. 4, pp. 1326–1337, April 2008.

[115] C.-L. Wang and H.-W. Chen, "A New Signal Structure for Active Sensing in Cognitive Radio Systems," *IEEE Transactions Communications*, vol. 62, no. 3, pp. 822–835, March 2014.

[116] N. Bambal and S. Dixit, "CMOS Limiting Amplifier and RSSI (Received Signal Strength Indicator)," in *International Conference on Emerging Trends in Engineering and Technology*, Nov 2011, pp. 238–243.

[117] S. Farooq and A. Ghafoor, "Analysis of Multiband Sensing-Time Joint Detection Framework for Cognitive Radio Systems," in *IEEE Vehicular Technology Conference*, 2012, pp. 1–5.

[118] Z. Quan, S. Cui, A. Sayed, and H. Poor, "Wideband Spectrum Sensing in Cognitive Radio Networks," in *IEEE International Conference on Communications*, 2008, pp. 901–906.

[119] Z. Liu, Y. Liu, and H. Yang, "Energy efficient A/D conversion for sequential wideband multichannel spectrum sensing in cognitive radio network," in *International Conference on Advanced Communication Technology*, Jan 2013, pp. 580–585.

[120] F. Digham, M.-S. Alouini, and M. K. Simon, "On the energy detection of unknown signals over fading channels," in *IEEE International Conference on Communications*, vol. 5, 2003, pp. 3575–3579.

[121] E. Axell, G. Leus, E. Larsson, and H. Poor, "Spectrum Sensing for Cognitive radio : State-of-the-Art and Recent Advances," *IEEE Signal Processing Magazine*, vol. 29, no. 3, pp. 101–116, May 2012.

[122] L. Zhou and M. Nakamura, "Channel estimation of multiple transmit antennas for OFDM systems with cyclic delay preamble," in *IEEE Vehicular Technology Conference*, vol. 1, 2005, pp. 583–587.

[123] J. Singh, O. Dabeer, and U. Madhow, "On the limits of communication with low-precision analog-to-digital conversion at the receiver," *IEEE Transactions on Communications*, vol. 57, no. 12, pp. 3629–3639, December 2009.

[124] J. Mo and R. Heath, "Capacity Analysis of One-Bit Quantized MIMO Systems With Transmitter Channel State Information," *IEEE Transactions on Signal Processing*, vol. 63, no. 20, pp. 5498–5512, 2015.

[125] FCC, "Spectrum policy task force report," Federal Communications Commission, Tech. Rep. 02-155, Nov 2002.

[126] C.-C. Sung, M.-F. Chou, C.-C. Wu, C.-S. Chen, K.-A. Wen, and C.-Y. Chang, "Low power CMOS wideband receiver design," in *International Conference on Microelectronics*, 2004, pp. 287–290.

[127] Texas Instruments, "RF-Sampling and GSPS ADCs, Breakthrough ADCs Revolutionize Radio Architectures," in *Design Resources and References*, Dec. 2015. [Online]. Available: http://www.ti.com/lit/pdf/snwt001

[128] S. Zahrai and M. Onabajo, "A low-power hybrid ADC architecture for high-speed medium-resolution applications," in *International Midwest Symposium on Circuits and Systems*, 2015, pp. 1–4.

[129] M. Ahmadi and W. Namgoong, "Comparator power minimization analysis for sar adc using multiple comparators," *Circuits and Systems I: Regular Papers, IEEE Transactions on*, vol. 62, no. 10, pp. 2369–2379, 2015.

[130] Y. Zhu, C.-H. Chan, S.-P. U, and R. Martins, "An 11b 900 Ms/s time-interleaved sub-ranging pipelined-SAR ADC," in *European Solid State Circuits Conference*, 2014, pp. 211–214.

[131] W. Xu and K. Manolakis, "Robust Synchronization for 3GPP LTE system," in *IEEE Global Telecommunications Conf.*, 2010, pp. 1–5.

[132] K. Manolakis, D. Gutierrez Estevez, V. Jungnickel, W. Xu, and C. Drewes, "A Closed Concept for Synchronization and Cell Search in 3GPP LTE Systems," in *IEEE Wireless Communications and Networking Conference*, 2009, pp. 1–6.

[133] J.-J. van de Beek, M. Sandell, and P. Borjesson, "ML estimation of time and frequency offset in OFDM systems," *IEEE Transactions on Signal Processing*, vol. 45, no. 7, pp. 1800–1805, 1997.

[134] S. Ma, X. Pan, G.-H. Yang, and T.-S. Ng, "Blind Symbol Synchronization Based on Cyclic Prefix for OFDM Systems," *IEEE Transactions on Vehicular Technology*, vol. 58, no. 4, pp. 1746–1751, 2009.

[135] H. Setiawan and H. Ochi, "A low complexity physical-layer identity detection for 3GPP Long Term Evolution," in *International Conference on Advanced Communication Technology*, vol. 1, 2010, pp. 8–13.

[136] K. Guo, W. Xu, and G. Zhou, "Differential Carrier Frequency Offset and Sampling Frequency Offset Estimation for 3GPP LTE," in *IEEE Vehicular Technology Conference*, May 2011, pp. 1–5.

[137] Y. Tsuchida, S. Nagata, and M. Sawahashi, "Cell Search Time Performance Using Multipath Signals in LTE Downlink," in *IEEE Vehicular Technology Conference*, 2011, pp. 1–5.

[138] Y. Yang, W. Che, N. Yan, X. Tan, and H. Min, "Efficient implementation of primary synchronisation signal detection in 3GPP LTE downlink," *Electronics Letters*, vol. 46, no. 5, pp. 376–377, 2010.

[139] J.-I. Kim, J.-S. Han, H.-J. Roh, and H.-J. Choi, "SSS detection method for initial cell search in 3GPP LTE FDD/TDD dual mode receiver," in *International Symposium on Communications and Information Technology*, 2009, pp. 199–203.

[140] H. Cao, C. Ma, and P. Lin, "An area-efficient implementation of Primary Synchronization Signal detection in LTE," in *IEEE International Conference on Communication Technology*, 2010, pp. 722–725.

[141] S.-L. Su, Y.-C. Lin, and Y.-J. Fan, "Joint sector identity and integer part of carrier frequency offset detection by phase-difference in long term evolution cell search process," *IET Communications*, vol. 7, no. 10, pp. 950–959, 2013.

[142] P.-Y. Tsai and H.-W. Chang, "A new cell search scheme in 3GPP long term evolution downlink, OFDMA systems," in *Inter. Conf. on Wireless Communications Signal Processing*, 2009, pp. 1–5.

[143] C.-C. Liao, P.-Y. Tsai, and T.-D. Chiueh, "Low-Complexity Cell Search Algorithm for Interleaved Concatenation ML-Sequences in 3GPP-LTE Systems," *IEEE Wireless Communications Letters*, vol. 1, no. 4, pp. 280–283, 2012.

[144] Y. Shen, T. Luo, and M. Win, "Neighboring Cell Search for LTE Systems," *IEEE Transactions on Wireless Communications*, vol. 11, no. 3, pp. 908–919, 2012.

[145] Z. Zhang, J. Liu, and K. Long, "Low-Complexity Cell Search With Fast Pss Identification in LTE," *IEEE Transactions on Vehicular Technology*, vol. 61, no. 4, pp. 1719–1729, 2012.

[146] F. Classen and H. Meyr, "Frequency synchronization algorithms for OFDM systems suitable for communication over frequency selective fading channels," in *IEEE Vehicular Technology Conference*, Jun 1994, pp. 1655–1659 vol.3.

[147] P. H. Moose, "A technique for orthogonal frequency division multiplexing frequency offset correction," *IEEE Transactions on Communications*, vol. 42, no. 10, pp. 2908–2914, Oct 1994.

[148] H. Ni, G. Ren, and Y. Chang, "Complexity effective cell search scheme for OFDM cellular system," in *IEEE International Conference on Communication Systems*, 2010, pp. 700–704.

[149] N. R. Goodman, "Statistical Analysis Based on a Certain Multivariate Complex Gaussian Distribution (An Introduction)," *Ann. Math. Statist.*, vol. 34, no. 1, pp. 152–177, March 1963.

[150] S. Wolff, J. Gastwirth, and H. Rubin, "The effect of autoregressive dependence on a nonparametric test (corresp.)," *IEEE Transactions on Information Theory*, vol. 13, no. 2, pp. 311–313, Apr 1967.